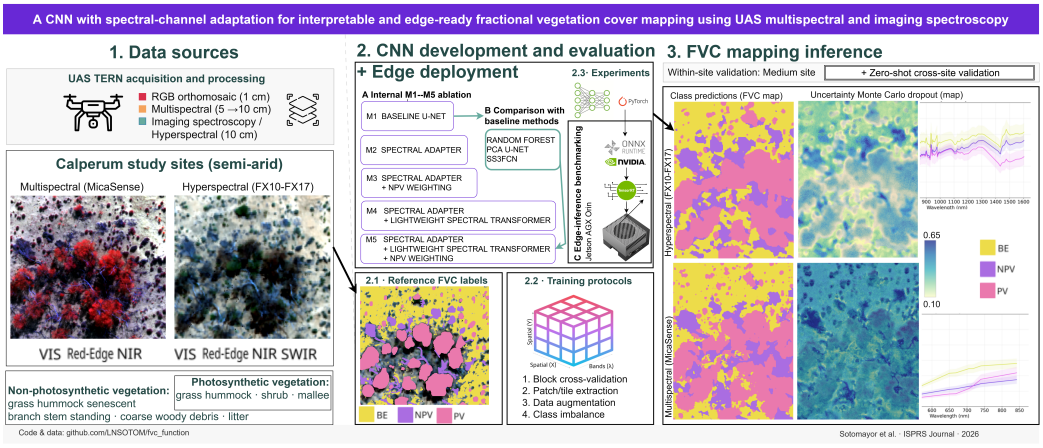
This manuscript is a preprint submitted to EarthArXiv and has not been peer reviewed. This manuscript is a preprint submitted to EarthArXiv. It has undergone peer review and substantial revisions in response to reviewers' comments. The revised manuscript has been resubmitted and is currently undergoing further peer review.

Graphical Abstract

A CNN with spectral-channel adaptation for interpretable and edge-ready fractional vegetation cover mapping using UAS multispectral and imaging spectroscopy

Laura N. Sotomayor, Arko Lucieer, Ryan Haynes, Darren Turner, Johan Barthelemy, Teja Kattenborn



A CNN with spectral-channel adaptation for interpretable and edge-ready fractional vegetation cover mapping using UAS multispectral and imaging spectroscopy

Laura N. Sotomayor[a], Arko Lucieer[a], Ryan Haynes[a], Darren Turner[a], Johan Barthelemy[b,c], Teja Kattenborn[d]

[a]*School of Geography, Planning, and Spatial Sciences, Hobart, Tasmania, Australia*
[b]*Securing Antarctica's Environmental Future (SAEF), University of Wollongong, Wollongong, , NSW, Australia*
[c]*NVIDIA NVAITC, Australia*
[d]*Sensor-based Geoinformatics (geosense), University of Freiburg, Freiburg, Breisgau, Germany*

Abstract

Non-photosynthetic vegetation (NPV) remains difficult to map in semi-arid fractional vegetation cover (FVC) because it overlaps with photosynthetic vegetation (PV), bare ground (BE), shadows, and mixed vegetation–soil surfaces.

We developed an NPV-aware convolutional neural network workflow with spectral-channel adaptation for UAS multispectral and imaging spectroscopy data. The benchmark combined controlled M1–M5 ablations with comparisons against Random Forest, plain and PCA-reduced U-Nets, and SS3FCN under shared held-out spatial folds. We also evaluated matched spatial resolution, post-inference spectral characterisation, uncertainty, zero-shot transfer, and TensorRT deployment.

NPV weighting produced the largest target-class gains. M5 achieved the highest NPV F1 (0.496; +0.148 relative to M1), whereas M3 achieved the highest mean F1 (0.745) and mIoU (0.629). In the combined 296-band FX10–FX17 benchmark, M5 achieved mean F1 of 0.705 and mIoU of 0.573; the strongest baseline values were 0.688 and 0.565, respectively. PCA underperformed the plain U-Net using the combined 296-band input despite retaining more than 99% of spectral variance. Resampling MICA to 10 cm reduced NPV F1 from 0.725 to 0.539, although it retained higher mIoU than FX10–

FX17 (0.667 versus 0.573).

Post-inference analyses confirmed persistent NPV instability and spectral ambiguity. The highest zero-shot external-site NPV F1 was 0.120. On Jetson AGX Orin, mixed-precision FX10–FX17 inference achieved a 1.70-fold speed-up with 99.96% argmax agreement, although pure FP16 was unstable. The workflow provides an interpretable, edge-compatible baseline while highlighting the need for broader cross-site validation.

Keywords: UAS hyperspectral, multispectral imagery, transfer, deep learning, vegetation function mapping, edge deployment

---

1. Introduction

Fractional vegetation cover (FVC) is a key descriptor of ecosystem condition in dryland and semi-arid environments, where sparse herbaceous and woody vegetation, dry plant material, and exposed substrates vary strongly across space and time. In component-based fractional cover products, the land surface is commonly partitioned into photosynthetic vegetation (PV; green vegetation with high chlorophyll content), non-photosynthetic vegetation (NPV; woody material, litter, and dry or senescent plant material), and bare ground (BE; soil, gravel, and rock). These fractions provide an ecologically meaningful representation of active vegetation, dry biomass, and exposed ground, supporting assessments of vegetation condition, degradation risk, productivity, surface stability, grazing capacity, carbon-related ecosystem processes, and ecosystem resilience (Fisk et al., 2019a; Morgan et al., 2020; Melville et al., 2019a; Harrison et al., 2021; Li et al., 2023). In drought-affected drylands, changes in PV, NPV, and BE are particularly important because they can indicate shifts in vegetation dynamics, dry biomass accumulation, soil exposure, and ecosystem function (Brodribb et al., 2020, 2021; Dou et al., 2025).

Optical remote sensing provides a practical basis for estimating these FVC components because PV, NPV, and BE differ in their reflectance across visible (VIS), red-edge, near-infrared (NIR), and shortwave-infrared (SWIR) wavelengths. VIS wavelengths are sensitive to pigment absorption, the red-edge region captures the transition from chlorophyll absorption to enhanced NIR reflectance, NIR wavelengths are strongly influenced by leaf and canopy structure, and SWIR wavelengths provide complementary sensitivity to water status and dry-matter components (Lewis et al., 2001; Homolová et al., 2013).

However, the measured reflectance signal is not uniquely controlled by a single vegetation property, because absorption, scattering, canopy structure, substrate background, illumination, and viewing geometry interact (Kattenborn et al., 2019c,b; Homolová et al., 2013; Wang et al., 2019b; Kattenborn et al., 2024). Vegetation indices (VIs) have therefore been widely used as empirical proxies for greenness, productivity, pigment status, water status, and related ecosystem properties (Tucker, 1979; Merton, 1998; Xue and Su, 2017; Montero et al., 2023; Haynes et al., 2026). In drylands, however, VI interpretation remains context-dependent because dry vegetation, exposed substrate, shadows, canopy structure, and mixed vegetation-soil backgrounds can produce overlapping spectral responses (Lewis et al., 2001; Fisk et al., 2019a; Melville et al., 2019a; Li et al., 2023; Kattenborn et al., 2024). Explicit PV-NPV-BE mapping is therefore important for distinguishing green vegetation, non-photosynthetic dry biomass, and exposed ground, improving the physical interpretability of FVC estimates beyond greenness-based proxies.

Building on these spectral principles, satellite Earth observation data, including multispectral missions such as Landsat and Sentinel-2 and spaceborne imaging spectroscopy missions such as the Italian PRecursore IperSpettrale della Missione Applicativa (PRISMA) and the German Environmental Mapping and Analysis Program (EnMAP), enable repeated and spatially extensive monitoring of vegetation cover across dryland landscapes (Scarth, 2012; Guanter et al., 2015; Storch et al., 2023; Chabrillat et al., 2024). Multispectral observations have supported the estimation of PV, NPV, and BE fractions, including Landsat-based FVC products and comparisons with field hyperspectral measurements in Australian drylands (Scarth, 2012; Fisk et al., 2019b). More recently, spaceborne imaging spectroscopy has expanded opportunities for vegetation characterisation through contiguous spectral measurements, supporting dry-vegetation assessment, subpixel fractional-abundance estimation, and vegetation classification in arid and semi-arid environments (Verrelst et al., 2023; Chabrillat et al., 2024; Reddig et al., 2025). Nevertheless, the moderate spatial resolution of satellite observations can limit the detection of small vegetation patches, exposed soil, litter, shadows, and fine-scale mixtures of PV, NPV, and BE in heterogeneous rangelands. High-resolution UAS imagery therefore provides complementary spatial information for resolving local surface composition and supporting the development and validation of satellite-derived FVC products (Fisk et al., 2019a; Melville et al., 2019a; Morgan et al., 2020; Li et al., 2023).

Imagery from unoccupied aerial systems (UAS) complements satellite-

based monitoring by providing centimetre-scale spatial resolution and detailed information on local vegetation structure, canopy gaps, shadows, and exposed ground patterns (Lucieer et al., 2014; Melville et al., 2019b; Turner et al., 2024; Sotomayor et al., 2025a, 2026; Mosig et al., 2026). Integrating UAS-derived RGB imagery with multispectral data has been shown to improve FVC mapping by capturing fine-scale spatial and spectral variation in PV, NPV, shadows, and exposed BE within semi-arid ecosystems (Bian et al., 2016; Chen et al., 2016; Choi et al., 2016; Melville et al., 2019b; Sotomayor et al., 2025a). UAS multispectral sensors typically acquire data in the VIS, red-edge, and NIR regions, providing sensitivity to greenness, canopy structure, and broad vegetation-soil contrasts (Melville et al., 2019a; Bollard et al., 2022; Sotomayor et al., 2025a). However, although multispectral imagery has demonstrated strength in discriminating and mapping broad biophysical vegetation variables such as leaf area index, and canopy cover, and in monitoring vegetation condition such as greenness, resolving compositional variation among PV, NPV, and BE remains difficult. This limitation arises because broad spectral bands may not capture diagnostic variation associated with pigment degradation, vegetation drying, dry plant material, shadow effects, and heterogeneous soil backgrounds, leading to potential confusion among FVC components (Lewis et al., 2001).

UAS imaging spectroscopy, hereafter referred to as hyperspectral imagery, addresses this spectral limitation by measuring narrow and contiguous bands across the VNIR–SWIR region (Asner and Martin, 2009; Ustin and Gamon, 2010; Zhao et al., 2021). Compared with broadband multispectral imagery, hyperspectral data preserve wavelength-dependent information and provide greater sensitivity to subtle functional differences associated with pigment-related responses, red-edge behaviour, moisture condition, dry vegetation material, canopy structure, and background effects in sparse vegetation communities (Malenovský et al., 2017; Yang et al., 2021; Turner et al., 2023; Wang et al., 2019a; Cotrozzi, 2022; Jutras-Perreault et al., 2023; Cimoli et al., 2024; Haynes et al., 2024). Because the available SWIR range in this study extends only to approximately 1600 nm and does not capture longer SWIR absorption features, moisture-sensitive contrast, dry-material signals, and soil-background interactions are interpreted as trait-sensitive spectral indicators or functional-condition proxies rather than direct biochemical or physiological measurements.

The high dimensionality of UAS hyperspectral imagery creates both an opportunity and a modelling challenge. Dimensionality-reduction and feature-

selection approaches, including spectral indices, principal component analysis, spectral summary statistics, and selected narrow bands, are commonly used to simplify hyperspectral inputs and reduce computational burden (Sothe et al., 2020; Cimoli et al., 2020; Kattenborn et al., 2021; Sandino et al., 2025). These approaches can retain dominant spectral variance or target diagnostic wavelength regions linked to biochemical, structural, and moisture-related vegetation properties, and have been effective for arid vegetation discrimination, vegetation-health assessment, water-content estimation, pigment-proxy mapping, and stress detection (Lewis et al., 2001; Malenovský et al., 2015, 2017; Turner et al., 2023; Montes-Herrera et al., 2024; Sandino et al., 2025; Cimoli et al., 2026; Haynes et al., 2026). However, reducing hyperspectral data to indices, principal components, summary statistics, or a limited set of selected bands may discard wavelength-specific and spectral-shape information needed to separate PV, NPV, BE, and transitional vegetation states. This is particularly problematic where pigment decline, vegetation drying, dry plant material, shadow, and soil-background effects produce overlapping spectral responses (Sothe et al., 2020; Kattenborn et al., 2021). Conversely, retaining full spectral resolution alone does not resolve spatially mixed pixels, diffuse class boundaries, limited training data, or spectral shifts between sites.

Traditional pixel-based machine learning methods, including Random Forest and support vector machines, and object-based image analysis have also been applied to vegetation and FVC mapping (Mishra and Crews, 2014; Sothe et al., 2020). These approaches can perform well when suitable spectral and spatial features, sampling designs, segmentation scales, class-balancing strategies, and model parameters are selected. Under variable illumination, however, pixel-based classifiers may confuse shadow with shaded PV, NPV, dark substrate, or water unless shadow-sensitive features, representative training samples, or spatial context are provided. Object-based methods can add texture, shape, and neighbourhood information, but their results depend on feature selection and segmentation scale. The synthesis by Kattenborn et al. (2021) found that CNNs often outperformed shallow machine learning methods across vegetation remote-sensing tasks, particularly where high-resolution spatial patterns were informative, while learning relevant features within an end-to-end framework. CNNs are not insensitive to shadow or illumination changes, but their learned spatial context can complement spectral information when separating shadow from vegetation and substrate classes.

Our previous UAS FVC study treated shadow as an explicit class and used spatial block cross-validation to evaluate site-specific and generic U-Net models across three semi-arid vegetation sites (Sotomayor et al., 2025a). Site-specific models achieved stronger performance than the generic model, while dense vegetation structure, spectral ambiguity, and limited reference data reduced accuracy. These findings motivated the present focus on spatially controlled evaluation, sensor-specific spectral representation, class imbalance, and cross-site transfer rather than assuming that a single model will generalise across vegetation structures and illumination conditions.

Deep learning segmentation algorithms provide a pathway for integrating spectral and spatial information from high-resolution UAS imagery. Convolutional neural networks (CNNs), in particular, have been widely applied in vegetation mapping because they can learn local spatial features such as edges, textures, patch boundaries, and neighbourhood context (Kattenborn et al., 2019a, 2020, 2021; Schiefer et al., 2023; Sotomayor et al., 2025a; Möhring et al., 2025). These features are important for FVC mapping because PV, NPV, BE, and shadows often vary over short distances in response to vegetation structure, senescence, substrate exposure, and local microtopographic conditions. However, in many two-dimensional (2D) CNN applications to hyperspectral imagery, spectral bands are treated as input channels. This allows spectral information to be learned implicitly, but does not explicitly encode wavelength order, band adjacency, or physically meaningful spectral intervals. As a result, the contribution of red-edge regions, SWIR-sensitive wavelengths, or diagnostically important spectral intervals to class predictions may be difficult to control or interpret. Although CNNs have been adapted to learn informative relationships from canopy spectra for plant-trait retrieval (Cherif et al., 2023), spatially explicit segmentation of hyperspectral imagery can benefit from spectral-channel adaptation integrated with CNN-based spatial feature extraction.

The need to jointly represent spectral-channel information and spatial context has motivated the adaptation of modern vision architectures for remote sensing segmentation. Transformer-based encoders, including Vision Transformers (ViTs), CNN–Transformer hybrids, and SegFormer-style models (Xie et al., 2021), can capture longer-range spatial dependencies and contextual relationships beyond the local receptive fields of conventional CNNs (Jiang et al., 2023; Joshi and Witharana, 2025; Möhring et al., 2025). In high-resolution vegetation mapping, SegFormer-style architectures have been used for tree-cover delineation and vegetation-condition segmentation from RGB

UAS imagery (Veitch-Michaelis et al., 2024; Möhring et al., 2025). Nevertheless, adapting these models to multispectral or hyperspectral imagery remains non-trivial because standard pretrained SegFormer models are typically configured for three-channel RGB inputs. Although transfer learning from pretrained RGB models can reduce annotation requirements and improve model generalisation, extending RGB-pretrained architectures to additional spectral bands requires modification of the initial patch-embedding layer, which can limit the direct reuse of pretrained RGB weights (Xie et al., 2021; Kattenborn et al., 2021; Růžička and Markham, 2024; Chowdhury et al., 2027). Recent hyperspectral ViT adaptations, including HyperSegFormer, address this limitation by modifying Transformer-based segmentation models to process high-dimensional hyperspectral data cubes more directly (Růžička and Markham, 2024). However, Transformer-based models often require larger annotated datasets and greater computational resources when trained directly, which can limit their operational use in ecological applications where labelled data are sparse (Li et al., 2024; Chowdhury et al., 2027).

These data and computational constraints are particularly relevant for UAS vegetation mapping. Prior reviews of CNN-based vegetation studies report a median of approximately 2795 reference observations across UAS- or airborne-based studies in the reviewed literature (Kattenborn et al., 2019a, 2021). Reported reference data volumes vary among sensing platforms, reflecting differences in spatial extent, opportunities for reference data reuse, and the class separability enabled by finer spatial or structural detail in higher-resolution observations. In this data-constrained context, U-Net encoder–decoder CNNs remain a practical option for UAS-based FVC segmentation because they provide efficient pixel-wise prediction, integrate multiscale spatial context, and can be trained with comparatively modest annotation effort (Huang et al., 2018; Brodrick et al., 2019; Kattenborn et al., 2019a, 2021).

For UAS hyperspectral FVC mapping, the central challenge is therefore not simply to adopt increasingly complex vision architectures, but to preserve diagnostically relevant spectral information while maintaining the spatial precision, annotation efficiency, and transferability required for component-level segmentation. This is important because transferable UAS-derived FVC products can provide fine-scale reference information for evaluating regional satellite-derived vegetation cover estimates, where coarser pixels often integrate multiple ground-cover components. New site inference remains difficult because vegetation condition, senescence, soil background, illumina-

tion, shadow, and substrate exposure can shift spectral distributions between training, validation, and deployment areas. Hyperspectral workflows also involve trade-offs among spectral richness, spatial resolution, signal-to-noise ratio, storage requirements, calibration complexity, and computational cost (Kattenborn et al., 2021; Chowdhury et al., 2027). Spectral adapter modules provide one mechanism for addressing these constraints by translating high-dimensional hyperspectral inputs into learned spectral-channel representations before spatial decoding, allowing CNN-based models to exploit spectral information while retaining local boundary-delineation ability (Braham et al., 2025). In this study, spectral-channel adaptation refers to learned reweighting and mixing of input channels representing spectral bands. The adapter operates under a fixed input-band configuration but does not explicitly encode wavelength coordinates, band adjacency, or local spectral continuity.

Building on existing UAS-derived FVC labels (Sotomayor et al., 2025b) and previous CNN-based segmentation work in sparse rangelands (Sotomayor et al., 2025a), this study extends FVC mapping to imaging spectroscopy, with particular emphasis on the spectral ambiguity of non-photosynthetic vegetation (NPV). While related work has explored the reuse of UAS-derived labels for 2D–3D transfer and growth-form mapping (Sotomayor et al., 2026), the present study focuses on spectral-channel adaptation, multispectral and hyperspectral segmentation, and cross-site generalisation.

Operational feasibility is also important for UAS-based environmental monitoring, as high-dimensional hyperspectral imagery and tiled inference can impose substantial computational demands. While high-performance computing (HPC) supports model development and large-scale processing, portable edge GPUs offer opportunities to perform inference closer to data acquisition, potentially reducing processing delays and data transfer requirements. Integrating edge-based inference with UAS data acquisition could support near-real-time vegetation mapping and timely field decisions, particularly in remote environments. Previous research on onboard and edge AI for UAS remote sensing (Koubaa et al., 2023), NVIDIA Jetson platforms (Mittal, 2019; López-Fandiño et al., 2024), and computationally efficient hyperspectral models (Haut et al., 2019; Růžička and Markham, 2024) motivates the evaluation of edge-inference feasibility as a step towards future onboard deployment.

Accordingly, this study makes three primary contributions:

1. We adapt and benchmark a previously developed CNN-based FVC segmentation framework (Sotomayor et al., 2025a) for multi-sensor UAS optical imagery, with emphasis on the spectrally ambiguous NPV component. A controlled M1–M5 ablation using a common U-Net backbone evaluates spectral-channel adaptation, lightweight cross-channel attention, and NPV-weighted optimisation. A separate combined 296-band FX10–FX17 benchmark compares M5 with five baseline configurations: per-pixel Random Forest, plain U-Net M1, PCA-3 and PCA-10 versions of the same plain U-Net, and the published SS3FCN spectral–spatial CNN.

2. We assess post-inference spectral characterisation and model interpretability by relating predicted BE, NPV, and PV classes to reflectance responses, pairwise spectral separability, uncertainty- and confusion-stratified spectra, post-inference spectral-index maps, Monte Carlo dropout-based uncertainty, and spectral-importance analyses based on learned input-gate profiles, gradient sensitivities, and spectral permutation, with particular attention to the spectral ambiguity of NPV.

3. We evaluate edge-inference feasibility on NVIDIA Jetson AGX Orin by exporting selected multispectral and imaging spectroscopy models to ONNX, optimising them with TensorRT, and assessing numerical consistency, engine footprint, latency, throughput, and precision-dependent performance. These benchmarks establish a foundation for future onboard UAS inference and deployment.

2. Materials

2.1. Study area and datasets

We tested the CNN with spectral-channel adaptation at one site (SASMDD0001), known as an AusPlot site that is part of the Australian Terrestrial Ecosystem Research Network (TERN), and performed inference at another TERN AusPlot (SASMDD0013) (White et al., 2012), each representing similar vegetation types as defined by the National Vegetation Information System (NVIS) (DCCEEW, 2017). The sites sample the predominant structural formations of this semi-arid area, encompassing a range of vegetation types, soil characteristics, and structural complexities (White et al., 2012; TERN, 2026) (detailed in Table 1). The study sites covered a total area of

19 hectares (ha) and are located at Calperum Station near Renmark, South Australia (see Figs. 1 and 2, where further details of UAS imagery processing are described in Section 3.1). This area experiences low annual rainfall (average 265 mm) and an average temperature of 17 °C.

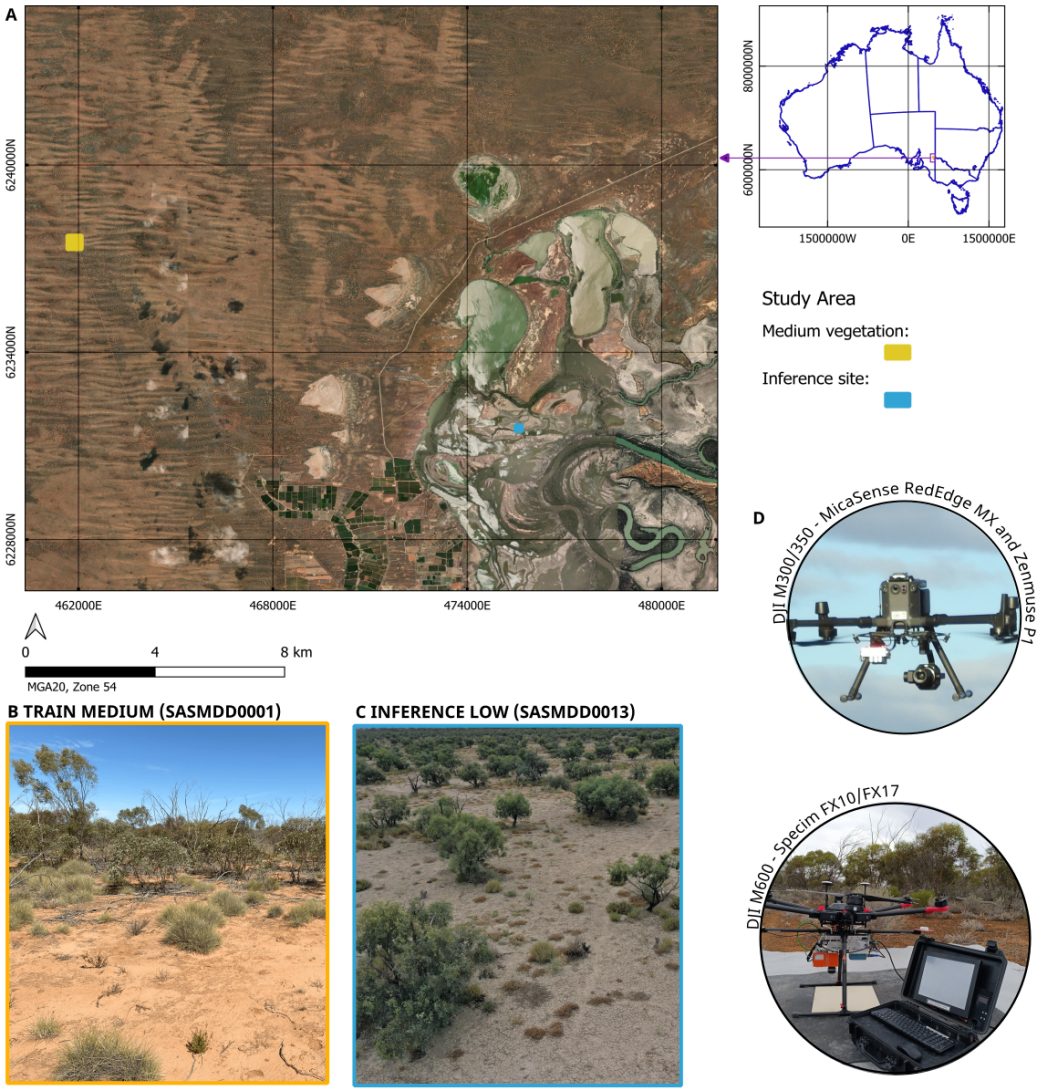


Figure 1: **A** Location of the two study sites (rectangle coloured boxes in map top-left) at Calperum Station, South Australia, each representing a different vegetation community (**B** for medium site trained and **C** for low site used as inference). **D** the UAS platforms used for data acquisition during the survey.

The medium density site (SASMDD0001) sits on a stable longitudinal dunefield and dune crest, and supports a regenerating multi-stemmed mallee canopy dominated by *Eucalyptus socialis* subsp. *socialis*, *E. cyanophylla* and *E. dumosa* (mostly 0.5-5 m), influenced by past fire events, over a sparse understorey of *Triodia scariosa* hummock grasses (0.01–3.70 m, median 0.30 m) (see Fig. 2B, C). Here, standing and emergent dead branches persisting after fire add to the coarse woody debris and litter, creating structural diversity through mallee stems, *Triodia* hummocks, and NPV branches. On the other hand, the low vegetation site (SASMDD0013) is a low open woodland of *Eucalyptus largiflorens* (0.6–5.0 m, median 2.5 m) on a floodplain, with a sparse ground cover of *Maireana pyramidata* chenopod shrubs (0.2–0.6 m) and scattered annual grasses and forbs (see Fig. 2G, H). The soil surface is cryptogam crusted with poor drainage over a reddish-brown calcareous sandy loam, consistent with a Calcarosol.

Table 1: Site descriptions including area, land system, dominant vegetation, height, structure and growth forms (White et al., 2012; TERN, 2021; TERN et al., 2022; TERN, 2026)

AusPlot IDs	**Site area**	**Land system and soil type**	**Dominant vegetation**	**Height of strata**	**Growth forms and structural components**
SASMDD0001 (medium)	369 m x 400 m (≈ 15 ha)	Stable inland dune-swale system; reddish loamy sand	Low open woodland of multi-stemmed mallee *Eucalyptus* spp. over sparse understorey of *Triodia scariosa* hummock grasses and shrubs	Upper (Mallee trees) and Ground (mainly *Triodia*): 0.5–5 m	Hummock grass, multi-stemmed mallee trees, shrubs, coarse woody debris, and litter. Standing/emergent NPV branches/stem that still stand after regeneration after fire and emergent dead branches
SASMDD0013 (low)	152 m × 186 m (≈ 2.8 ha)	Floodplain plain; soil surface recorded as cryptogam surface with poor drainage; reddish-brown calcareous sandy loam	*Maireana pyramidata* (Black bluebush) low open shrubland with scattered annual grasses and forbs	Tree/shrub layer: 0.6–5.0 m for *Eucalyptus largiflorens* (median 2.5 m); chenopod shrub layer: 0.2–0.6 m for *Maireana pyramidata* (median 0.4 m)	Low open *Eucalyptus largiflorens* woodland with sparse chenopod shrubs, annual grasses, and forbs

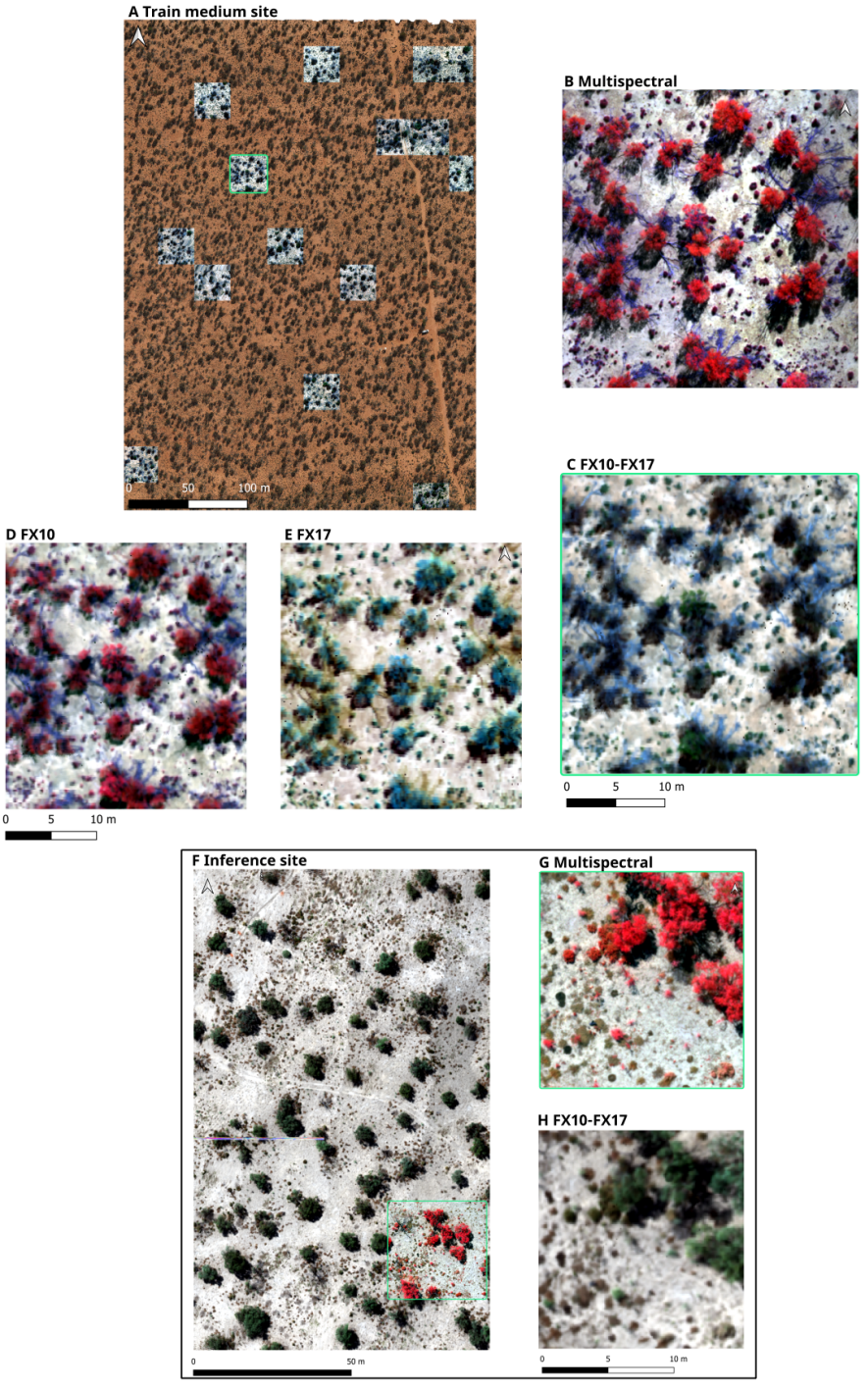


Figure 2: Multi-sensor remote sensing imagery across training and inference sites with contrasting vegetation structure. **A** RGB orthomosaic of the medium vegetation training site, overlaid with 15 labelled hyperspectral tiles (3070 × 3070 pixels); the green box marks the subset shown in **B**–**E**. **B**–**E** Enlargements of this subset: **B** multispectral imagery (NIR-842 nm, Red-668 nm, Blue-475 nm), **C** fused FX10–FX17 imagery (639.585 nm, 551.015 nm, 468.725 nm), **D** FX10 imagery (800.445 nm, 609.955 nm, 529.695 nm), and **E** FX17 imagery (1597.010 nm, 1299.800 nm, 999.630 nm). **F** FX10–FX17 orthomosaic of the low-vegetation inference site, characterised by sparse vegetation and extensive exposed ground; the green box marks the subset shown in **G**–**H**. **G**–**H** Enlargements of this subset from multispectral and fused FX10–FX17 imagery, respectively, using the band combinations in **B** and **C**.

3. Methods

The proposed workflow integrates band-aware CNN-based FVC segmentation, post-inference spectral characterisation, and edge-deployment benchmarking. After the study area and datasets are described in Section 2, Section 3.1 details the generation of calibrated reflectance imagery and FVC reference labels from the multi-sensor UAS optical datasets. The experimental framework compares a baseline CNN with spectral-encoding CNN variants (Section 4). Model outputs are evaluated and interpreted using class probabilities, Monte Carlo dropout-based uncertainty, class-wise reflectance responses, pairwise spectral separability, post-inference spectral-index maps, and model-derived spectral importance scores. Finally, the best-performing models are exported to ONNX, converted to TensorRT, and benchmarked on Jetson hardware to assess the feasibility of scalable band-aware FVC segmentation for edge deployment. The full pipeline, *hyperFVC*, is publicly available at `https://github.com/LNSOTOM/fvc_function`.

3.1. UAS acquisition and processing

3.1.1. UAS platforms and sensors

Datasets were acquired using DJI Matrice RTK UAS platforms equipped with optical imaging sensors. The May 2022 campaign, including the medium density site, was conducted with a DJI Matrice 300 RTK platform carrying a DJI Zenmuse P1 RGB camera and a MicaSense (MICA) RedEdge-MX/Dual multispectral sensor. The low density inference site was acquired in March 2024 using the updated DJI Matrice 350 RTK platform. Multispectral imagery comprised ten broad bands: Blue-444, Blue-475, Green-531, Green-560, Red-650, Red-668, Red Edge-705, Red Edge-717, Red Edge-740, and NIR-842 nm. Flight parameters were optimised for each optical sensor, with RGB and multispectral imagery collected at 80 m above ground level at a flying speed of 8 m/s, resulting in ground sampling distances of approximately 1 cm/pixel and 5 cm/pixel, respectively. Further details on data collection and preprocessing are provided in the TERN drone data collection and imagery processing protocols (TERN, 2022; Montes-Herrera et al., 2025).

The imaging spectroscopy sensors were mounted on a DJI Matrice 600 UAS (DJI, Shenzhen, China). The payload was designed as a modular system, allowing different imaging spectroscopy sensors to be interchanged. In this study, two Specim sensors (Specim, Oulu, Finland) were flown consecutively for each site: the FX10, which measures in the visible to near-infrared

region of the electromagnetic spectrum (400–1000 nm), and the FX17, which measures in the near-infrared to shortwave-infrared region (900–1700 nm). The FX10 and FX17 acquired 224 and 112 spectral bands, respectively, before preprocessing and removal of unusable or overlapping bands. The average Full Width at Half Maximum (FWHM) of the FX10 is 5.5 nm and 8 nm for the FX17. The pose orientation system (POS) for determination of sensor location and orientation was the Advanced Navigation Certus Evo, which was hard-mounted to the sensors with the lever arm offsets measured with millimeter precision. At each site, the FX10 and FX17 sensors were flown on separate consecutive flights, with less than 15 min between acquisitions to exchange sensors. Because the two flights were consecutive rather than simultaneous, solar geometry changed slightly between acquisitions, and shadow positions and lengths may therefore differ marginally between the FX10 and FX17 imagery at pixel scale. Both sensors were flown at 90 m above ground level at a flying speed of 4 m/s resulting in a spatial resolution of approximately 6 cm/pixel for the FX10 and 9.6 cm for the FX17 (before re-sampling both to 10 cm). For more information on the UAS and sensor configuration, see Haynes et al. (2025).

3.1.2. UAS RGB and multispectral processing

The RGB and multispectral imagery were georeferenced using the DJI D-RTK2 base station and the onboard Global Navigation Satellite System Real-Time Kinematic (GNSS RTK) receiver, providing an expected absolute positioning accuracy of approximately 5 cm without the use of ground control points. Imagery was processed in Agisoft Metashape Professional v. 2.0 following the TERN drone RGB and multispectral image processing protocols (TERN, 2021, 2022; TERN et al., 2022). The processing workflow generated spatially co-registered RGB and multispectral orthomosaics for downstream analysis. Multispectral imagery was radiometrically calibrated using a camera calibration panel and co-registered with the RGB product during processing. The calibrated multispectral images were orthorectified using the RGB-derived surface model to produce multispectral orthomosaics spatially aligned with the RGB orthomosaic. Further details of this workflow are provided in (TERN, 2022; Montes-Herrera et al., 2025). Together, these steps produced georeferenced, co-registered RGB and multispectral reflectance products suitable for subsequent model development and analysis.

Multispectral reflectance scaled-integer storage for CNN modelling. The multispectral orthomosaics were stored as scaled integers to reduce file size while preserving reflectance precision. Valid float32 reflectance values were multiplied by a scale factor of 10,000 and converted to int16, preserving four decimal places of precision and maintaining consistency with the hyperspectral integer-scaled data products. Invalid pixels, including NaN and existing nodata values, were excluded from scaling and assigned a nodata value of -1. Valid reflectance values can be recovered by dividing the stored values by 10,000.

3.1.3. UAS Imaging spectroscopy processing

The hyperspectral imagery was radiometrically calibrated, geometrically corrected, and converted to surface reflectance. For radiometric correction and georectification, both sets of imagery (FX10 and FX17) were processed line by line in Caligeo Pro, using factory calibration files provided by Specim and high accuracy post-processed data from the POS. After this processing, the individual passes were trimmed to remove the jagged edges (retaining the central 80 - 90 percent of the imagery). These hyperspectral orthomosaic image strips were then co-registered to the RGB mosaic from 2022 using optical flow method eFOLKI (Iteration: 8., radius: [16. 8. 4]., rank: 4., levels: 6) to ensure pixel-level alignment. Finally, the spatially aligned image strips were converted to reflectance using Atmospheric Radiative Transfer Modelling (ARTM) software DROACOR (RESE, 2025). Noise-dominated and water absorption bands were interpolated prior to analysis. Specifically, the bands associated with the absorption feature at 1400 nm were interpolated (between wavelengths 1320.9 and 1419.62 nm). To reduce high frequency noise while preserving the diagnostic absorption features, the reflectance for each pass were minimally smoothed using a Savitsky-Golay (SAVGOL) filter (window length 3, poly order 1). Then, all passes were mosaicked in ENVI using the seamless mosaic tool. Further details on imaging spectroscopy data preprocessing can be found (Haynes et al., 2025, 2026).

FX10–FX17 spectral trimming and stacking for CNN modelling. For CNN modelling, the FX10 and FX17 hyperspectral orthomosaics were spectrally trimmed and concatenated to produce a single VNIR–SWIR reflectance stack. The original FX10 and FX17 products contained 224 and 112 bands, covering 397.765–1003.915 nm and 933.330–1719.595 nm, respectively (Table 2). Trimming was performed to remove noise-dominated sensor-edge channels

and minimise redundant spectral overlap between the two sensors. The ENVI metadata were also inspected for bands flagged as interpolated, where reflectance values are estimated from neighbouring spectral channels during sensor calibration rather than measured as fully independent observations. This information was considered when defining the retained wavelength ranges. Within the retained wavelength range, the stack also included 15 interpolated bands in the atmospheric water-absorption interval of 1320.9–1419.62 nm. Interpolation maintained spectral continuity but did not recover reliable measured reflectance, and interpolated values may introduce artificial spectral structure. Spectral continuity was not required by the CNN architecture, so exclusion or masking remained a valid alternative.

For the FX10 sensor, bands 10–215 were retained, yielding 206 bands from 421.345 to 978.565 nm. Bands 1–9, corresponding to 397.765–418.725 nm, were removed because they occur at the lower edge of the FX10 spectrum, where calibration uncertainty and reduced signal-to-noise ratio may affect reflectance stability. Bands 216–224, corresponding to 981.375–1003.915 nm, were also removed to avoid redundancy with the beginning of the FX17 spectral range.

For the FX17 sensor, bands 7–96 were retained, yielding 90 bands from 978.850 to 1604.130 nm. Bands 1–6 were omitted because they overlapped with the retained FX10 range, with FX17 band 7 beginning at 978.850 nm, close to the final retained FX10 band at 978.565 nm. Bands 97–112 were excluded from the upper SWIR edge, where reflectance estimates are more susceptible to noise and calibration uncertainty. The final combined FX10–FX17 stack therefore contained 296 bands, with FX10 bands 10–215 followed by FX17 bands 7–96, covering an overall wavelength range of 421.345–1604.130 nm.

Before stacking, the FX17 orthomosaic was aligned to the FX10 grid where needed using bilinear resampling, with the FX10 orthomosaic left unresampled. No spectral resampling to a common wavelength grid was applied; the retained sensor-specific bands were concatenated along the band dimension at their native wavelength sampling.

Table 2: Spectral configuration of the FX10, FX17, and combined FX10–FX17 hyperspectral datasets.

Dataset	Band range	Number of bands	Wavelength range (nm)
FX10 full range	1–224	224	397.765–1003.915
FX17 full range	1–112	112	933.330–1719.595
FX10–FX17 used stack	FX10: 10–215; FX17: 7–96	296	421.345–1604.130
FX10 component	10–215	206	421.345–978.565
FX17 component	7–96	90	978.850–1604.130

3.2. 2D reference data extraction for U-Net segmentation models

U-Net-based semantic segmentation requires co-registered predictor rasters and categorical reference masks prepared as paired image–mask tiles. Two-dimensional (2D) predictor–reference datasets were therefore generated for multispectral and hyperspectral model configurations using a common fractional vegetation cover (FVC) class schema: bare ground (BE = 0), non-photosynthetic vegetation (NPV = 1), and photosynthetic vegetation (PV = 2) (see Table 3 and Fig. 3). This schema followed the 2D reference-label framework developed for site-specific FVC mapping by Sotomayor et al. (2025a,c).

3.2.1. Annotation and mask alignment

Reference labelling. We adopted the orthomosaic tiling and reference data generation workflow described by Sotomayor et al. (2025a). For manual interpretation, 15 multispectral source tiles were randomly selected and converted to 8-bit false-colour composites using the blue, red, and NIR bands. Reference polygons for BE, NPV, and PV were digitised in LabelMe, an open-source annotation platform (Wada and others, 2021), with Efficient-SAM used as an AI-assisted interactive segmentation model to support polygon delineation (Xiong et al., 2023, 2024). The resulting labels were inspected and refined in QGIS 3.28.0-Firenze to correct inaccurate automated delineations and improve class-boundary consistency. The refined polygons were then merged into a unified vector label dataset and rasterised according to the site-specific class characteristics of the three FVC classes BE, NPV, and PV, summarised in Table 3 and illustrated with examples in Fig. 3.

Sensor-specific mask alignment. The refined annotation masks were first prepared at 1 cm resolution and then downsampled to the 5 cm multispectral

grid using majority-vote resampling. Each multispectral predictor tile was used as the reference grid to ensure matching extent, transform, and raster dimensions. For the hyperspectral configurations, the 5 cm multispectral-aligned masks were further downsampled to the 10 cm FX10, FX17, and combined FX10–FX17 grids, again using majority-vote resampling with the corresponding predictor tile as the reference. This produced aligned masks for each sensor configuration while preserving the common BE, NPV, and PV class schema. Invalid or unlabelled pixels were assigned to the ignore class and excluded from the loss during training.

Table 3: FVC class definitions and structural subclasses used for reference-label generation at the medium-density training site. Structural subclasses were used to guide annotation but were aggregated into the three modelled FVC classes: BE, NPV, and PV.

ID	**Class**	**Structural subclass**	**Annotation definition**
0	BE	Bare ground	Exposed bare ground or substrate without visible vegetation cover.
1	NPV	Standing branch/stem	Attached, upright, or emergent dead woody material, including branches or stems persisting after fire and lacking live foliage; often associated with offset shadows.
		Coarse woody debris	Larger detached dead woody material, including fallen branches or stems lying on the ground.
		Litter	Fine dead plant material on the ground, including leaves, bark fragments, and small twigs.
		Senescent hummock grass	Dry or ageing hummock grass with limited or no visible photosynthetic foliage.
2	PV	Mallee	Live multi-stemmed eucalypt growth, typically resprouting from lignotubers or epicormic buds after fire.
		Shrub	Live perennial woody plants with multiple stems; height classes may be recorded separately as < 2 m or ≥ 2 m.
		Hummock grass	Live spiny perennial grass forming rounded hummocks that may expand into open rings with age.

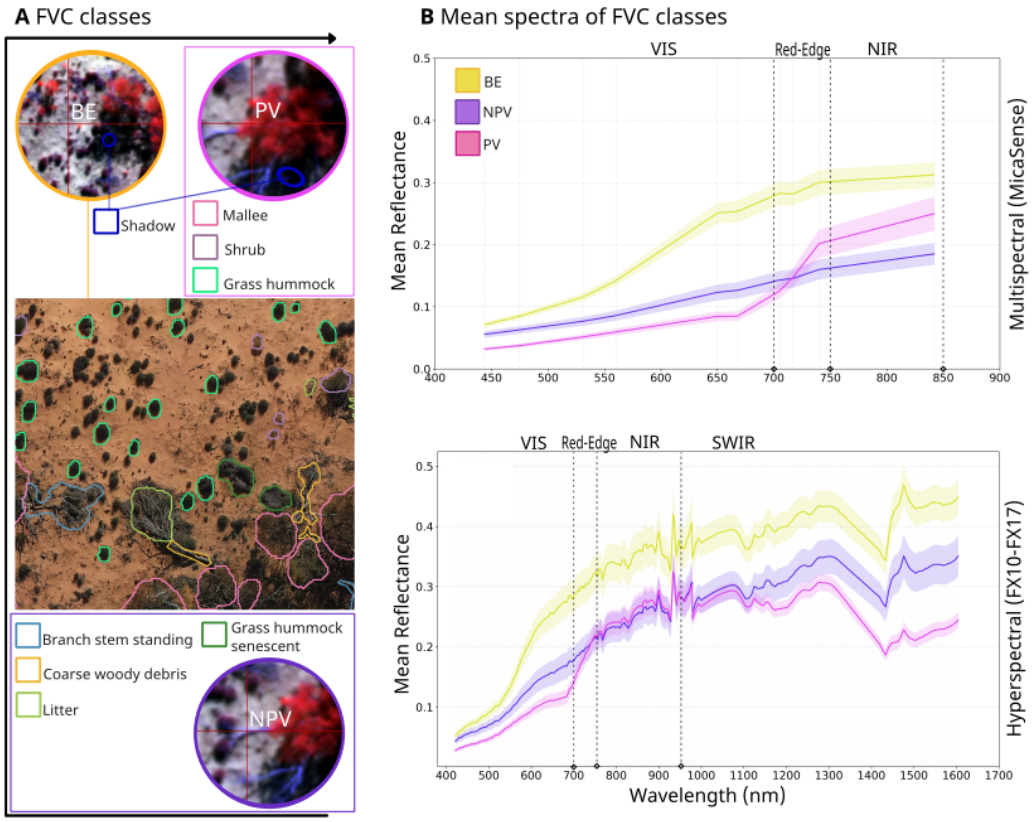


Figure 3: FVC classes and their spectral separability in multispectral and hyperspectral imagery. **A** Enlarged RGB image subset of the study area showing representative structural components used to interpret the three FVC classes: BE, PV, and NPV. PV includes live mallee, shrub, and grass hummock components, whereas NPV includes standing dead stems, coarse woody debris, litter, and senescent hummock grasses. Shadowed pixels are highlighted as an image-level confounding condition that can reduce local reflectance and complicate visual separation among BE, PV, and NPV, but they were not treated as a separate FVC class. These components provide ecological context for the image labels but were aggregated into BE, PV, and NPV for model training and inference. **B** Mean spectral reflectance responses for BE, PV, and NPV, shown as coloured lines with shaded 95% confidence intervals calculated from all reference data tiles at the study site. The top panel shows MicaSense multispectral responses across the VIS, Red-Edge, and NIR regions, while the bottom panel shows FX10–FX17 hyperspectral responses across the VIS, Red-Edge, NIR, and SWIR regions. Vertical dashed lines indicate approximate spectral-region boundaries.

3.2.2. Sensor-specific predictor preparation

Predictor rasters were prepared separately for multispectral and hyperspectral configurations because the sensors differed in spatial resolution, tile size, and spectral dimensionality.

Multispectral predictors. The multispectral orthomosaic was used as the predictor source on a 5 cm raster grid. Source tiles were generated at 614×614 pixels, corresponding to approximately 30.70×30.70 m. eflectance values followed the project scaled-integer convention, where valid float reflectance values were multiplied by 10,000 and stored as signed 16-bit integers, while invalid or NoData pixels retained the project NoData value.

To test the contribution of spatial resolution to the performance difference between the multispectral and hyperspectral models, an additional matched-resolution MICA predictor set was prepared by resampling the MICA imagery from 5 cm to 10 cm. This control retained the MICA spectral bands and radiometric product but matched the spatial grid, 152×152-pixel patch size, reference masks, and spatial data splits used for the FX10–FX17 hyperspectral configuration.

Hyperspectral predictors. The FX10 and FX17 reflectance mosaics were used as predictor sources on a 10 cm raster grid. Three hyperspectral configurations were prepared: FX10-only, FX17-only, and combined FX10–FX17. Spectral inputs used FX10 bands 10–215 and FX17 bands 7–96; for the combined configuration, the selected bands from both sensors were concatenated along the spectral dimension before patch extraction. Hyperspectral source tiles were generated at 304×304 pixels, corresponding to approximately 30.40×30.40 m.

3.2.3. Scale-specific crop and patch extraction

Patch extraction was performed separately for the multispectral and hyperspectral predictor configurations to preserve each sensor's native spatial resolution while producing U-Net-compatible input sizes (Table 4).

Multispectral configuration. Each 614×614 multispectral predictor–mask tile was centre-cropped to 608×608 pixels (divisible by 32 for U-Net compatibility) without spatial resampling, and subdivided into 304×304 patches with 50% overlap, generating nine paired samples per source tile.

Hyperspectral configurations. The 304×304 hyperspectral source tiles were not resized or resampled; input samples were extracted as overlapping spatial windows of 304×304, 224×224, or 152×152 pixels, yielding one, four, or nine samples per tile, respectively (Table 4). Larger hyperspectral patches increased the spatial context represented by each sample but reduced the number of samples available for training and evaluation.

For all configurations, predictor rasters and reference masks were matched by tile ID and processed using identical crop or window offsets to preserve pixel-wise correspondence between inputs and labels. Patches derived from the same original source tile were kept within the same training, validation, or test subset to avoid spatial leakage between data splits.

Table 4: Predictor–reference patch extraction summary. Patch totals are reported per predictor configuration.

Sensor/profile	Spatial scale	Source tile	Patch size	Patches/tile	Total patches	Train/val/test
Multispectral	5 cm	$614 \times 614 \rightarrow 608 \times 608$	304×304	9	135	72 / 27 / 36
FX10, FX17, FX10–FX17	10 cm	304×304	152×152	9	135	72 / 27 / 36
FX10, FX17, FX10–FX17	10 cm	304×304	224×224	4	60	32 / 12 / 16
FX10, FX17, FX10–FX17	10 cm	304×304	304×304	1	15	8 / 3 / 4

4. Experiments

4.1. Model benchmark design

FVC mapping was formulated as a dense semantic segmentation task in which each valid pixel was assigned to one of three classes: BE, NPV, or PV. Invalid or unlabelled pixels were assigned an ignore label of (-1) and were excluded from loss computation and metric evaluation.

The model benchmark comprised two complementary components. First, an internal M1–M5 ablation evaluated the effects of spectral-channel adaptation, lightweight cross-channel attention, and NPV-weighted optimisation. All five internal variants used the same U-Net-style spatial encoder–decoder backbone and differed only in the spectral front-end, cross-channel-attention setting, and class-weighting configuration. Second, a baseline-method comparison evaluated the proposed M5 pipeline against a traditional per-pixel Random Forest, the plain U-Net M1 using the combined 296-band FX10–FX17 input, PCA-3 and PCA-10 versions of the same plain U-Net, and the published SS3FCN spectral–spatial CNN. These configurations used identical spatial folds and held-out test partitions, allowing the proposed pipeline to

be compared with traditional machine learning, variance-based dimensionality reduction, a direct U-Net reference, and a representative spectral–spatial CNN.

The internal ablation comprised a baseline U-Net CNN, a spectral-adapter CNN, an NPV-weighted spectral-adapter CNN, a spectral-adapter CNN with lightweight cross-channel attention, and an NPV-weighted spectral-adapter CNN with lightweight cross-channel attention. Table 5 summarises this ablation sequence.

Table 5: Model variants used to evaluate spatial convolutional learning, spectral-channel embedding, lightweight cross-channel attention, and class-weighted loss optimisation. Class weights are reported in the order BE, NPV, and PV.

Variant	Description	Spectral mode	Cross-channel attention	Weighted loss	Isolated comparison
M1	Baseline U-Net CNN	`no_spectral`	0	–	reference spatial encoder–decoder
M2	Spectral-adapter CNN	`enhanced`	0	–	effect of spectral-channel embedding
M3	Weighted spectral-adapter CNN	`enhanced`	0	$[1, 2, 1]$	effect of NPV up-weighting without cross-channel attention
M4	Spectral-adapter CNN with lightweight cross-channel attention	`enhanced`	1	–	effect of lightweight cross-channel interaction modelling
M5	Weighted spectral-adapter CNN with lightweight cross-channel attention	`enhanced`	1	$[1, 2, 1]$	combined spectral-channel embedding, cross-channel attention, and imbalance-aware optimisation

4.1.1. Baseline U-Net CNN

The baseline model provided the spatial encoder–decoder reference against which all spectral-channel adapter variants were compared (Ronneberger et al., 2015). In this configuration, reflectance bands were passed directly to the shared U-Net backbone described in Section 4.2.4, without the spectral adapter or lightweight cross-channel attention. This model quantified

the performance achievable when spectral bands were learned implicitly by standard convolutional feature extraction.

4.1.2. Spectral-adapter CNN

The spectral-adapter CNN was implemented as a study-specific combination of established architectural components, rather than as a direct reimplementation of a single published adapter model. The design combined squeeze-and-excitation-style channel recalibration (Hu et al., 2019), hyperspectral spatial–spectral attention concepts (Wang et al., 2019a), pixel-wise (1×1) convolutional projection (Lin et al., 2014), and the shared U-Net segmentation backbone (Ronneberger et al., 2015).

The adapter was inserted before the U-Net encoder to perform band-aware recalibration and spectral-channel embedding. It first estimated band-wise weights from the input reflectance patch and used these weights to modulate the relative contribution of each spectral channel. This provided an adaptive spectral reweighting step before spatial decoding, allowing the model to emphasise channels useful for separating BE, NPV, and PV.

After band recalibration, the adapter projected the input bands into a fixed 32-channel learned spectral embedding using stacked (1×1) convolutional operations with batch normalisation, Gaussian Error Linear Unit (GELU) activation, and dropout (Lin et al., 2014; Hendrycks and Gimpel, 2023). The notation "32 ch" refers to learned spectral feature channels, not to 32 original reflectance bands. For multispectral inputs, this acted as a band-aware remapping module. For hyperspectral inputs, it also provided trainable dimensionality reduction from the larger input band set to the same fixed embedding dimension.

The module did not explicitly use wavelength-centre or bandwidth metadata; therefore, learned weights were spectral-channel specific under a fixed input band order rather than wavelength-parameterised. This variant tested whether explicit spectral-channel encoding improved BE, NPV, and PV segmentation relative to the baseline U-Net CNN.

4.1.3. Spectral-adapter CNN with lightweight cross-channel attention

The attention-enabled variants added a lightweight cross-channel attention block after the spectral adapter and before the U-Net encoder. This block was designed as a computationally efficient channel-attention module rather than as a full vision transformer over spatial image tokens. The design

was inspired by transformer self-attention (Vaswani et al., 2023) and hyperspectral transformer studies that use attention to model spectral signatures and joint spectral–spatial representations (He et al., 2021; Hong et al., 2022; Růžička and Markham, 2024; Makarov et al., 2025).

The module operated on the 32-channel learned spectral embedding produced by the adapter. Instead of applying self-attention across all spatial pixels, it summarised the adapted feature tensor using global spatial descriptors and used these descriptors to estimate cross-channel interactions. The resulting attention-weighted representation was passed through a (1×1) projection, residual connection, normalisation, and lightweight feed-forward convolutional block.

This transformer-inspired design modelled cross-channel interactions while avoiding the memory cost of full spatial self-attention. It is therefore interpreted as lightweight global channel attention over the learned spectral embedding, rather than as a conventional ViT-style token transformer. The corresponding ablation tested whether explicit cross-channel interaction modelling improved FVC segmentation beyond the spectral-adapter CNN alone.

4.1.4. Class-weighted spectral-adapter variants

Class-weighted optimisation was evaluated as a loss-function ablation for the spectral-adapter CNN variants with and without lightweight cross-channel attention. These variants used the class-weighting term of focal loss (Lin et al., 2017), with ($\alpha = [1, 2, 1]$) for BE, NPV, and PV, respectively. Thus, NPV pixels contributed more strongly to the loss than BE or PV pixels during training.

The weighting was applied only to M3 and M5. M3 isolated the effect of NPV up-weighting for the spectral-adapter CNN, whereas M5 tested the same weighting in combination with lightweight cross-channel attention. Because the input data, class definitions, backbone structure, and evaluation protocol were otherwise held constant, performance differences between weighted and unweighted variants were interpreted as the effect of imbalance-aware optimisation.

To assess sensitivity to the NPV class weight, an additional experiment was conducted using the spectral-adapter and cross-channel-attention architecture shared by M4 and M5. Only the NPV coefficient in the focal-loss class-weight vector was varied, with weights reported in the order BE, NPV, and PV. The $[1, 1, 1]$ configuration corresponded to the unweighted M4 formulation, whereas $[1, 2, 1]$ corresponded to M5. All configurations used the

same 296-band FX10–FX17 inputs, 152-pixel patches, spatial folds, augmentation data, optimiser settings, and model architecture. Each configuration was trained from scratch across three spatial folds for 120 epochs using seed 42. We compared the class weights $[1, 1, 1]$, $[1, 2, 1]$, and $[1, 3, 1]$ using the validation set. The $[1, 2, 1]$ configuration achieved the highest validation NPV F1, macro F1, and mIoU and was therefore selected. The test set was not used to choose the class weight.

Together, the five configurations form a controlled ablation sequence that evaluates spectral-channel embedding, lightweight cross-channel attention, and NPV-weighted optimisation relative to the same U-Net spatial backbone. Detailed implementation information is provided in the GitHub repository, called *hyperFVC*, and available at `https://github.com/LNSOTOM/fvc_function`.

4.1.5. Comparison with baseline methods

The combined 296-band FX10–FX17 benchmark compared the proposed M5 pipeline with five baseline configurations using identical training, validation, and held-out test tile partitions across the three spatial cross-validation folds. A traditional per-pixel Random Forest classifier (Breiman, 2001) provided a conventional machine-learning baseline without spatial context. For each fold, a Random Forest with 300 trees (`max_features = sqrt`, minimum leaf size 2, and no class weighting) was trained on up to 50,000 labelled pixels per class, sampled without replacement from that fold's training tiles using a deterministic fold-specific random seed. The combined 296-band reflectance spectra were used as input features, and performance was evaluated on all valid labelled pixels in the corresponding held-out test tiles.

The plain U-Net using the combined 296-band input corresponded to the M1 configuration in the ablation sequence (Section 4.1) and provided a direct combined-sensor baseline without PCA, spectral-channel adaptation, cross-channel attention, or class weighting. PCA-based baselines were included to characterise redundancy across the hyperspectral bands and to test whether unsupervised, variance-preserving spectral compression was sufficient for FVC classification (Uddin et al., 2021). A separate PCA basis was fitted within each fold using only its training data, comprising 143,928 sampled spectra from 72 training patches, and was subsequently applied to the corresponding validation and test data. The combined 296-band input was projected onto the first three (PCA-3) or first ten (PCA-10) principal components, which were then classified using the plain U-Net M1 configuration.

This fold-specific fitting procedure prevented information from the validation or held-out test tiles from influencing the PCA transformation.

SS3FCN was implemented as a published spectral–spatial CNN baseline (Zou et al., 2020). Its shared spectral-reduction stem and spectral–spatial branches were adapted to accept the combined 296-band FX10–FX17 input and produce dense three-class BE–NPV–PV predictions. M5 represented the proposed NPV-weighted spectral-channel adaptation pipeline with lightweight cross-channel attention.

The plain U-Net, PCA–U-Net, and SS3FCN baselines used the same augmentation protocol as the main models and unweighted focal loss. M5 instead used NPV-weighted focal loss with class weights $[1, 2, 1]$, while the Random Forest was unweighted and used no augmentation because it operated on individual pixel spectra. All trainable models were initialised and trained from scratch for each of the three spatial folds and followed the shared checkpoint-selection and evaluation protocol (Section 4.2.5). Consequently, this benchmark compares complete training pipelines rather than isolating architecture from class weighting.

4.2. Experimental settings

4.2.1. Datasets, sites, and sensors

The experiments were conducted using the predictor–reference datasets described in Section 3.2. These datasets comprised multispectral and hyperspectral UAS image patches paired with BE, NPV, and PV reference masks. The native multispectral configuration used the MICA 5 cm predictor grid, whereas the hyperspectral configurations used the 10 cm FX10-only, FX17-only, and combined FX10–FX17 predictor grids. For the matched-resolution experiment, the native MICA imagery was additionally resampled from 5 cm to 10 cm and aligned to the combined FX10–FX17 grid. All experiments used masks aligned to their corresponding predictor rasters to ensure pixel-wise correspondence between input reflectance data and reference labels.

Within-site evaluation used source-tile-level partitions to prevent overlapping patches from crossing training, validation, and test splits; the complete partitioning and independent cross-site protocols are described in Sections 4.2.5 and 4.2.8, respectively.

4.2.2. Matched spatial-resolution comparison

The spatial-resolution analysis included three independently trained M5 configurations: native MICA at 5 cm, MICA resampled to 10 cm, and the

combined 296-band FX10–FX17 input at 10 cm. The primary matched-resolution comparison was between the two 10 cm inputs. Resampled MICA was clipped to the combined FX10–FX17 source-tile extents, and both configurations used the same majority-vote masks, spatial folds, augmentation, and training and evaluation protocol described in Section 4.2.5.

Native 5 cm MICA was included as a separate reference. Because the native and resampled MICA models were trained independently, their performance difference represents a resolution-associated effect across matched training pipelines rather than evaluation of one model at two resolutions. Comparing resampled MICA with combined FX10–FX17 at 10 cm evaluates multispectral and hyperspectral inputs after matching spatial resolution, although wavelength coverage, radiometry, noise, and other sensor-specific differences remain.

4.2.3. Water-absorption channel exclusion sensitivity

A supplementary FX10–FX17 sensitivity experiment tested the effect of excluding the 15 interpolated channels within the 1320.9–1419.62 nm atmospheric water-absorption interval (Section 3.1). This reduced the hyperspectral input from 296 to 281 bands while keeping the same spatial folds, patch-generation workflow, M5 model configuration, and evaluation metrics.

4.2.4. Shared U-Net architecture and optimisation settings

All CNN variants used the U-Net-style encoder–decoder backbone summarised in Table 6; input dimensionality, enabled spectral modules, and class weighting varied by experiment. The backbone used five encoder stages (64–1024 channels) with a 2048-channel bottleneck, 3×3 convolutional blocks with batch normalisation, ReLU activation, and dropout, 2×2 max-pooling and transposed-convolution sampling with skip connections, and a 1×1 classifier producing logits for the three FVC classes.

Models were trained with focal loss and Adam. Invalid or unlabelled pixels were excluded using ignore index -1. The focal-loss alpha term was 1 for unweighted experiments and $[1, 2, 1]$, in BE, NPV, and PV order, for the default weighted setting. Remaining architecture and optimisation settings are reported in Table 6.

Table 6: Shared U-Net architecture, optimisation, and training hyperparameters used across model variants. Input-channel dimensionality was sensor-dependent, while output classes, backbone structure, optimiser settings, and focal-loss form were kept consistent. The focal-loss alpha term differed only for the class-weighted variants.

Hyperparameter	Value
Input and output configuration	
Number of input channels	Sensor-dependent: 5 for selected multispectral inputs, 10 for full MICA multispectral inputs, 90 for FX17, 206 for FX10, and 296 for combined FX10–FX17 hyperspectral inputs
Number of output classes	3: BE, NPV, and PV
Output activation	Model returned logits; softmax was applied for probability-map interpretation and hard-class prediction
U-Net backbone architecture	
Encoder filter depths	64, 128, 256, 512 and 1024 channels
Bottleneck channels	2048 channels
Convolution kernel size	3×3
Final classifier kernel size	1×1 convolution
Pooling size	2×2 max pooling
Upsampling operation	2×2 transposed convolution
Dropout probability	0.3
Hidden activation function	ReLU in the CNN U-Net blocks
Spectral adapter activation	GELU when the spectral adapter was enabled
Optimisation and training settings	
Number of epochs	120
Batch size	4 patches per mini-batch
Gradient accumulation	2 mini-batches per optimiser step
Effective batch size	8 patches per optimiser step
Optimiser	Adam with initial learning rate 1×10^{-4}, OneCycleLR scheduling, weight decay 1×10^{-4}, and beta parameters $(0.9, 0.999)$
Mixed precision	CUDA automatic mixed precision
Gradient clipping	Maximum gradient norm = 1.0
Loss function and masking	
Loss function	Focal loss with focusing parameter $\gamma = 2$; invalid or unlabelled pixels were excluded using ignore index -1
Focal-loss alpha	1 for unweighted runs; class-weight vector for weighted runs, e.g., $[1, 2, 1]$ for BE, NPV, and PV

4.2.5. Training and inference protocols

Unless otherwise stated, CNN experiments followed the shared optimisation, checkpoint-selection, and evaluation settings in Table 6. Within each input configuration, compared variants used the same predictor–reference tiles and spatial splits; differences were limited to the components defined in

Section 4.1 and the sensor-specific augmentation protocols below.

Block-based data partitioning. Data were partitioned using a three-fold spatial block cross-validation strategy (Kattenborn et al., 2022; Sotomayor et al., 2025a). Annotated source tiles were grouped into spatial blocks, and one block was withheld as the independent test set in each fold. The remaining tiles were allocated to training and validation subsets using fixed tile-level counts. Source-site models were trained independently within each fold, with a new model and optimiser initialised for each fold, the validation subset used for checkpoint selection, and the spatially held-out block reserved for evaluation. In the default configuration, 8 base tiles were used for training, 3 for validation, and 4 for testing, corresponding to 53.3%, 20.0%, and 26.7% of the 15 annotated base tiles, respectively. All patches derived from the same source tile were kept within the same split to prevent spatial leakage between training, validation, and test data. For the 9-patch-per-tile exports, this produced 72 training patches, 27 validation patches, and 36 test patches; lower patch-density exports preserved the same tile-level partitioning.

Patch generation. Training samples were generated by extracting paired image-mask patches from the reflectance products and corresponding BE, NPV, and PV reference masks. Patch size and stride followed the sensor-specific settings described in Section 3.2. Patches with insufficient valid pixels or dominated by NoData regions were excluded. The same patch-generation procedure was used for all model variants to preserve comparability across ablations.

Data augmentation. Data augmentation was applied to augmentation-enabled training profiles to improve generalisation and reduce overfitting under limited labelled data. A conservative core protocol was used for the hyperspectral FX10, FX17, and combined FX10–FX17 experiments, and also formed the base of the reported MICA multispectral configuration. This core protocol included horizontal flipping, vertical flipping, random rotations in 90° increments, and mild coherent brightness-contrast jitter. Geometric transformations were applied identically to predictor patches and PV/NPV/BE masks to preserve pixel-wise correspondence, whereas radiometric transformations were applied only to predictor reflectance patches. Invalid and unlabelled pixels were propagated through the augmentation pipeline and retained as ignore regions.

For the reported MICA configuration, the core augmentations were retained and additional shadow-robust radiometric perturbations were enabled for multispectral imagery. These additional transformations included global gain jitter, per-band gain jitter, gamma adjustment, mild Gaussian noise, and synthetic shadow patches. They were not applied to the FX10, FX17, or combined FX10–FX17 hyperspectral experiments because stronger radiometric perturbations can distort narrow-band spectral signatures important for hyperspectral classification. The augmentation protocols are summarised in Table 7.

Table 7: Data augmentation protocols used during model training. The core protocol was used for FX10, FX17, and combined FX10–FX17 hyperspectral experiments and formed the base of the reported MICA multispectral configuration. The MICA protocol added shadow-robust radiometric transformations for multispectral imagery only.

Protocol	Augmentation type	Operation	Probability
Core	Geometric	Horizontal flip	0.5
Core	Geometric	Vertical flip	0.5
Core	Geometric	Random rotation in 90° increments	0.5
Core	Radiometric	Mild coherent brightness–contrast jitter	0.5
MICA add-on	Radiometric	Global gain jitter	0.5
MICA add-on	Radiometric	Per-band gain jitter	0.5
MICA add-on	Radiometric	Gamma adjustment	0.35
MICA add-on	Radiometric	Mild Gaussian noise	0.2
MICA add-on	Shadow simulation	Synthetic shadow patches	0.35

Geometric transformations were applied identically to predictor patches and PV/NPV/BE masks. Radiometric and shadow-simulation transformations were applied only to predictor reflectance patches; reference masks were unchanged.

Inference. Selected checkpoints were applied to held-out within-site test patches using deterministic inference. Softmax outputs supported probability-map interpretation, while hard class predictions were used for metrics and qualitative comparison. Monte Carlo dropout and cross-site inference were conducted separately as described in Sections 4.2.7 and 4.2.8.

4.2.6. Evaluation metrics

Model performance was assessed using semantic segmentation metrics calculated from valid labelled pixels only. Invalid or unlabelled pixels with the ignore label -1 were excluded from all metric calculations. For each FVC class $c \in \{\mathrm{BE}, \mathrm{NPV}, \mathrm{PV}\}$, precision, recall, F1-score, and Intersection

over Union (IoU) were calculated from the class-specific true positives (TP_c), false positives (FP_c), and false negatives (FN_c):

$$F1_c = \frac{2TP_c}{2TP_c + FP_c + FN_c}, \tag{1}$$

$$IoU_c = \frac{TP_c}{TP_c + FP_c + FN_c}. \tag{2}$$

The NPV F1-score was used as the primary target-class metric. Aggregate segmentation performance was summarised using macro averaged mean F1-score and mean IoU (mIoU) across BE, NPV, and PV:

$$\text{Mean F1} = \frac{F1_{\text{BE}} + F1_{\text{NPV}} + F1_{\text{PV}}}{3}, \tag{3}$$

$$\text{mIoU} = \frac{IoU_{\text{BE}} + IoU_{\text{NPV}} + IoU_{\text{PV}}}{3}. \tag{4}$$

Aggregate model-variant summaries were calculated by first computing metrics for each sensor-profile and patch-scale configuration, then averaging the corresponding configuration-level metrics by model variant. Detailed aggregation procedures are provided in Appendix A.

Within-site validation. Within-site validation quantified BE, NPV, and PV performance across model variants, sensor profiles, and patch scales using the independent test block defined in Section 4.2.5.

4.2.7. Monte Carlo dropout uncertainty mapping

Monte Carlo dropout was used as a post-inference diagnostic to map pixel-wise epistemic uncertainty from the trained segmentation models (Gal and Ghahramani, 2016; Scheiter et al., 2022; Sotomayor et al., 2025a). Epistemic uncertainty reflects incomplete model knowledge of the underlying data distribution and is relevant in semi-arid scenes where BE, NPV, PV, shadow, and mixed vegetation–soil backgrounds can be difficult to separate. Unlike aleatoric uncertainty, which is associated with intrinsic data noise, label ambiguity, or sensor variability, epistemic uncertainty can potentially be reduced through additional training data, improved model structure, or more representative spectral–spatial features.

Dropout layers with probability $p = 0.3$ were included in the segmentation network during training. For Monte Carlo dropout inference, model

weights were fixed while dropout layers remained active, and each valid input patch was evaluated over $T = 50$ stochastic forward passes. Let $\mathcal{C} = \{\mathrm{BE}, \mathrm{NPV}, \mathrm{PV}\}$ denote the set of FVC classes, and let (i, j) denote the row and column location of a pixel within an image patch. For class $c \in \mathcal{C}$, the pre-softmax logit from stochastic pass t was denoted as $z_c^{(t)}(i, j)$.

Pixel-wise logit-space epistemic uncertainty was calculated as the mean class-wise standard deviation of the logits across stochastic passes:

$$U_{\mathrm{raw}}(i, j) = \frac{1}{|\mathcal{C}|} \sum_{c \in \mathcal{C}} \mathrm{SD}_{t=1}^{T} \left[z_c^{(t)}(i, j) \right], \tag{5}$$

where $|\mathcal{C}| = 3$ and $U_{\mathrm{raw}}(i, j)$ denotes the raw uncertainty assigned to pixel (i, j). This quantity represents logit-space prediction variability and was interpreted as a relative measure of model uncertainty, rather than as a calibrated probability of error.

Uncertainty was calculated only for valid input pixels. Invalid, nodata, and ignored pixels were excluded using the valid data mask and written as missing values. Patch-level uncertainty outputs were stitched back into the orthomosaic coordinate grid using the same inference extent as the deterministic class predictions, producing georeferenced uncertainty rasters aligned with the FVC prediction maps. Class-wise uncertainty summaries were calculated by averaging the unscaled U_{raw} values over valid pixels assigned to each predicted FVC class. The uncertainty rasters were used only as post-inference diagnostic layers and were not included in the deterministic accuracy metrics.

For comparative visualisation of the selected FX10–FX17 and MICA outputs, uncertainty maps were displayed using the same colour ramp and shared display limits of 0.10–0.65. Values outside these limits were clipped for display only. This display scaling affected only map rendering and did not modify the underlying uncertainty values used for quantitative class-wise summaries.

4.2.8. Cross-site transfer experiments

Quantitative zero-shot cross-site evaluation. Cross-site transfer was evaluated using five tiles from the external site SASMDD0013 (tiles 2, 4, 7, 8, and 15). The reference masks were generated using the same semi-automated BE–NPV–PV annotation workflow applied at the source site, followed by manual inspection and correction of all three classes. They are therefore

described as manually reviewed and corrected external-site reference masks rather than as fully manual pixel-by-pixel annotations. Frozen source-site checkpoints selected using source-site validation loss were applied without target-site fine-tuning, hyperparameter adjustment, checkpoint selection, or other parameter updates using the external labels. The three fold-matched per-pixel Random Forest models (Section 4.1.5) were applied zero-shot to the same five tiles in the same way. Metrics included class-wise precision, recall, F1-score, and IoU, together with macro F1, mIoU, overall accuracy, class support, and confusion matrices. The five supplied tiles were not established as a random or stratified sample of the entire external site.

4.3. Post-inference spectral characterisation

Post-inference spectral characterisation was used to describe the spectral behaviour of pixels predicted as BE, NPV, and PV. The analysis combined reflectance-based class signatures, pairwise separability curves, spectral-index maps, and model-derived spectral-importance scores. Reflectance analyses were derived directly from the retained MICA and FX10–FX17 reflectance stacks, spectral indices were calculated from the retained FX10–FX17 reflectance bands, and importance scores were extracted from the trained spectral-encoding components.

4.3.1. Reflectance-based spectral response and class separability

Class-wise spectral responses were summarised from the retained reflectance stacks. Pixels predicted as BE, NPV, and PV were used as spatial masks, and reflectance values were extracted for each class across the available wavelength range. For each class and wavelength, mean reflectance responses were computed to describe the spectral profiles associated with the predicted FVC categories.

Pairwise separability between BE, NPV, and PV was calculated using standardised differences in class-wise mean reflectance responses. For each pair of classes and wavelength, the absolute class-mean difference was standardised to allow comparison across wavelengths and sensor profiles. The resulting curves were used to identify wavelength regions where predicted classes showed larger or smaller reflectance differences.

4.3.2. Uncertainty- and confusion-stratified spectral analysis

To trace the spectral composition of regions where NPV classification was difficult, mean reflectance spectra were extracted for uncertainty- and

confusion-stratified pixel sets using the combined 296-band FX10–FX17 M5 configuration. For the uncertainty analysis, valid pixels of each predicted class in the stitched inference tile were split into low- and high-uncertainty strata using the class-wise 25th and 75th percentiles of the Monte Carlo dropout uncertainty raster (Section 4.2.7), and mean reflectance spectra with one standard deviation envelopes were calculated for each stratum. For the confusion analysis, predicted classes on the four spatially held-out block-1 test tiles were cross-tabulated against the aligned reference masks, and mean reflectance spectra and mean uncertainty were calculated for each prediction–reference pair. Because stitched uncertainty rasters were generated only for the qualitative inference tile, which belonged to the block-1 training partition, the uncertainty stratification is reported for that tile, whereas the confusion-stratified spectra use only the spatially held-out test tiles.

4.3.3. Post-inference spectral-index mapping

To complement the reflectance-based spectral response analysis, five spectral indices were derived from the nearest available FX10–FX17 reflectance bands (Table 8). This post-inference mapping step was used to extend interpretation beyond the predicted distribution of BE, NPV, and PV components by examining spatial variation in spectral proxies associated with vegetation physiological and biochemical traits, moisture or dry-material conditions, and exposed-substrate contribution within and across FVC classes. The selected indices represented greenness and photosynthetic activity, red-edge response, pigment transition, moisture or dry-material variation, and exposed-substrate contribution.

For representative inference tiles, each index was computed directly from the retained FX10–FX17 reflectance stack and mapped spatially. The predicted FVC class map was included only as a spatial reference for comparison with the spectral-index layers. The spectral-index maps were not derived from model logits, probabilities, or predicted class labels, and they were not used as model inputs. For visualisation, each index map was displayed using per-panel 2–98% percentile-normalised scaling to emphasise within-index spatial gradients; this display normalisation did not affect the index calculations or predicted class maps.

Table 8: Spectral indices used for post-inference spectral characterisation of the BE–NPV–PV continuum in the FX10–FX17 imagery. R_λ denotes reflectance at the nearest available band to wavelength λ nm.

Index	Formula	Main spectral proxy	Diagnostic use
kNDVI	$\tanh(\mathrm{NDVI}^2)$, where $\mathrm{NDVI} = \frac{R_{842}-R_{668}}{R_{842}+R_{668}}$	Greenness and photosynthetic activity	Spatial distribution of stronger or weaker vegetation greenness response.
NDRE	$\frac{R_{842}-R_{717}}{R_{842}+R_{717}}$	Red-edge response	Spatial distribution of chlorophyll-sensitive red-edge variation.
PSRI	$\frac{R_{668}-R_{560}}{R_{842}}$	Pigment transition	Spatial distribution of relative pigment-transition and senescence-sensitive response.
MSI	$\frac{R_{1597}}{R_{861}}$	SWIR–NIR moisture-sensitive contrast	Spatial distribution of dry-material or moisture-related variation.
BSI	$\frac{(R_{1597}+R_{668})-(R_{861}+R_{480})}{(R_{1597}+R_{668})+(R_{861}+R_{480})}$	Exposed substrate	Spatial distribution of bare-ground or substrate-background contribution.

4.3.4. Model-derived spectral importance analysis

Model-derived spectral importance analysis was used to summarise the wavelength regions assigned the highest relative importance by the trained spectral-encoding components. Two complementary scores were computed. First, the spectral adapter's input gate assigns each input band b a learned weight $g_b \in (0, 1)$ that rescales the band before the 32-channel spectral embedding; reported gate scores are the per-band weights averaged over input patches. Second, the class-wise importance scores were computed as gradient-based logit sensitivities with respect to the original input bands, rather than the learned embedding channels. For class c, the class score $\bar{z}_c$ was defined as the mean class-c logit over the set $\mathcal{P}_c$ of pixels predicted as class c, and

the importance of band b was calculated as the mean absolute gradient of this score with respect to the band image:

$$S_c(b) = \frac{1}{HW} \sum_{i,j} \left| \frac{\partial \bar{z}_c}{\partial x_b(i,j)} \right|, \qquad \bar{z}_c = \frac{1}{|\mathcal{P}_c|} \sum_{(i,j)\in\mathcal{P}_c} z_c(i,j), \tag{6}$$

where $x_b(i,j)$ denotes the reflectance of band b at pixel (i,j). Because the gradient propagates through the complete network, including the spectral adapter, the 32-channel projection, and the attention and decoder stages, $S_c(b)$ quantifies the end-to-end sensitivity of each class logit to each original input band. Scores were normalised by their maximum absolute value within each class and sensor profile so that rankings represented relative spectral importance for a given model output rather than direct or absolute biophysical sensitivity.

To verify that the highlighted wavelength regions were not an artefact of the learned weights, a model-agnostic permutation-importance analysis was performed. For each named spectral region S, the pixel values of all bands in the region were jointly permuted across valid pixels, destroying the association between the region and the labels while preserving the region's band statistics and inter-band correlation, and the resulting drop in class-wise F1-score was recorded:

$$PI_c(S) = F1_c(\text{original}) - \frac{1}{R} \sum_{r=1}^{R} F1_c(\text{permuted}_r(S)), \tag{7}$$

with $R = 3$ repeats and a fixed random seed. The analysis was applied to the combined 296-band FX10–FX17 configuration using five named regions (VIS, 421–699 nm; red-edge, 702–748 nm; NIR, 751–1000 nm; SWIR, 1007–1604 nm; and the interpolated water-absorption interval, 1321–1420 nm) and, separately, to contiguous 25 nm windows.

The resulting importance rankings were interpreted alongside the reflectance-response and spectral-index analyses. Class-wise importance scores were treated as diagnostic model-output summaries rather than direct measurements of vegetation traits or substrate properties.

4.4. Deployment workflow and edge benchmarking

The selected hyperspectral FX10–FX17 s152 and multispectral MICA s304 FVC segmentation models were exported from PyTorch to ONNX before

TensorRT engine construction. The ONNX exports used dynamic batch and spatial dimensions, allowing inference over input tensors of size $N \times C \times H \times W$, where C denotes the number of spectral bands. Both exported models produced $N \times 3 \times H \times W$ logits corresponding to BE, NPV, and PV.

Although model training used automatic mixed precision (AMP), the ONNX exports retained FP32 weights. FP16 Reduced-precision execution was therefore introduced during TensorRT engine construction rather than inherited directly from the training configuration. Initial FP32 and pure FP16 TensorRT engines were built on Jetson AGX Orin hardware and benchmarked to characterise median latency, P99 latency, throughput, and serialized engine size. Inference latency was reported in milliseconds per tile, throughput was reported as tiles processed per second, and serialized engine size was reported in MiB.

Latency speed-up was calculated relative to the corresponding TensorRT FP32 baseline:

$$\text{Latency speed-up} = \frac{\text{FP32 median latency}}{\text{engine median latency}}.$$

Deployment consistency was evaluated by comparing ONNX Runtime and TensorRT outputs against the PyTorch reference on representative input patches. Parity assessment included logit differences, finite-logit checks, pixel-wise argmax agreement, and mIoU computed relative to the PyTorch argmax predictions across BE, NPV, and PV. TensorRT engines that produced non-finite logits were excluded from deployment interpretation.

Where pure FP16 execution was numerically unstable, Polygraphy precision debugging was used to construct mixed FP16/FP32 engines that preserved finite logits and high argmax agreement with the PyTorch reference. Unless stated otherwise, FP16-labelled TensorRT results refer to these validated mixed FP16/FP32 engines rather than pure FP16 engines. The final deployment comparison was therefore based only on finite-logit, parity-validated engines. The benchmark represents inference-stage edge deployment feasibility rather than a complete onboard UAS processing workflow.

5. Results

5.1. FVC classification performance across ablation experiments

5.1.1. Performance of baseline and spectral-channel adapter models

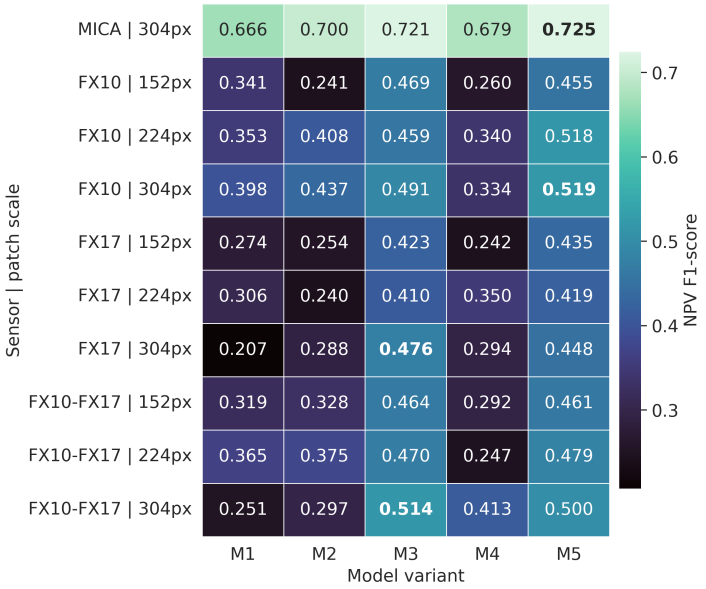
Within-site ablation results differed across model variants (Table 9). M5 achieved the highest aggregate NPV F1-score, while M3 achieved the highest mean F1-score and mIoU. Compared with the baseline M1, the unweighted spectral adapter M2 showed only a small increase in NPV F1, mean F1, and mIoU, while the addition of cross-channel attention without class weighting in M4 produced similar aggregate values to M1. In contrast, the NPV-weighted variants M3 and M5 produced substantially larger improvements.

Table 9: Aggregate within-site performance of the five model variants. Each value is the mean of the corresponding fold-mean metric over all sensor-profile and patch-scale configurations (MICA at 5 cm and FX10, FX17, and FX10–FX17 at 10 cm); the aggregation procedure is detailed in Appendix A. Values in parentheses indicate differences relative to M1. Per-configuration values, including the separation of the 5 cm multispectral and 10 cm hyperspectral profiles, are shown in Fig. 4, and sensor-level comparisons at matched resolution are reported in Table 11.

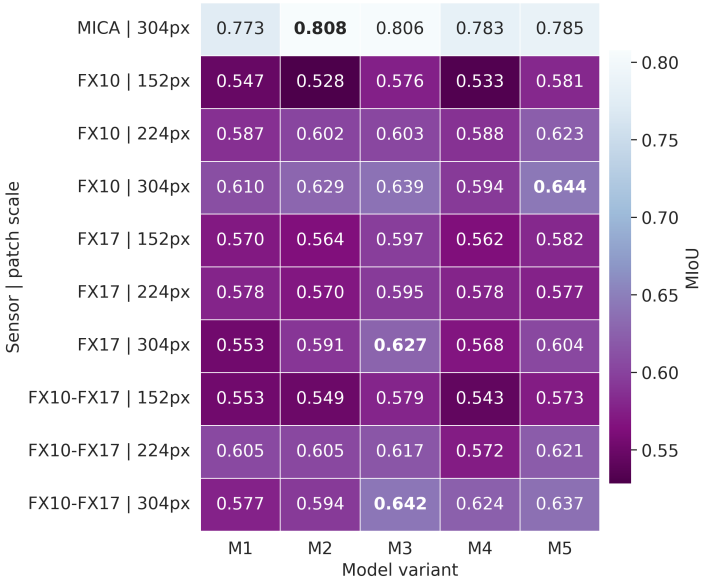
Variant	NPV F1	Mean F1	mIoU
M1	0.348 (–)	0.701	0.597 (–)
M2	0.357 (+0.009)	0.706	0.604 (+0.007)
M3	0.490 (+0.142)	**0.745**	**0.629** (+0.032)
M4	0.345 (−0.003)	0.700	0.596 (−0.001)
M5	**0.496** (+0.148)	0.744	0.625 (+0.028)

The NPV class-weight sensitivity analysis, including validation-based weight selection and held-out test results, is reported in Appendix A.1.

Across individual sensor-profile and patch-scale combinations, the highest NPV F1-score was achieved by either M3 or M5 (Fig. 4). M5 was most frequently the highest-ranked variant for NPV F1-score, whereas M3 had slightly higher aggregate mean F1-score and mIoU. Additional diagnostics, including NPV IoU, mean F1-score, the NPV F1–mIoU trade-off, and class-wise BE–NPV–PV F1-score and IoU, are provided in Appendix A.



(a) NPV F1-score.



(b) mIoU.

Figure 4: Within-site segmentation performance across model variants, sensor profiles, and patch scales. Rows denote sensor-profile and patch-scale combinations, and columns denote model variants M1–M5. Bold values indicate the highest value within each sensor row.

5.1.2. Performance comparison with baseline methods

For the combined 296-band FX10–FX17 input, the per-pixel Random Forest achieved a mean F1 of 0.688 and an mIoU of 0.556 (Table 10). The plain U-Net M1 achieved a lower mean F1 of 0.669 and a similar mIoU of 0.553.

For the PCA baselines, the first three principal components explained 99.341% of the training-spectra variance when averaged across the three fold-specific PCA bases, while the first ten explained 99.967%. Nevertheless, PCA-3 achieved a mean F1 of 0.602 and an mIoU of 0.503, and PCA-10 achieved 0.641 and 0.532, respectively. PCA-10 therefore outperformed PCA-3, but neither compressed-input configuration matched the plain U-Net using all 296 bands.

SS3FCN achieved a mean F1 of 0.685 and an mIoU of 0.565, making it, together with the Random Forest, one of the strongest baseline methods. The proposed M5 pipeline achieved the highest mean F1 (0.705) and mIoU (0.573) among all evaluated configurations. Its clearest advantage was for NPV, with an F1-score of 0.461 compared with 0.414 for the Random Forest, 0.319 for the plain U-Net M1, 0.143 for PCA-3, 0.245 for PCA-10, and 0.368 for SS3FCN.

Table 10: Held-out test performance for the proposed M5 pipeline and baseline methods using the same three spatial folds. Values are means of the three fold-level test metrics. PCA bases were fitted only on each fold's training tiles. M5 used NPV-weighted focal loss, whereas the CNN-based baseline configurations used unweighted focal loss and Random Forest used no class weighting.

Model	BE F1	NPV F1	PV F1	Mean F1	BE IoU	NPV IoU	PV IoU	mIoU
Random Forest (per-pixel)	0.837	0.414	0.811	0.688	0.721	0.262	0.686	0.556
Plain U-Net, combined 296-band input (M1)	0.864	0.319	**0.824**	0.669	0.763	0.191	**0.705**	0.553
PCA-3 + plain U-Net	0.856	0.143	0.809	0.602	0.749	0.077	0.681	0.503
PCA-10 + plain U-Net	0.860	0.245	0.818	0.641	0.757	0.142	0.695	0.532
SS3FCN (Zou et al., 2020)	**0.865**	0.368	0.822	0.685	**0.765**	0.229	0.702	0.565
M5, NPV-weighted	0.846	**0.461**	0.807	**0.705**	0.737	**0.300**	0.681	**0.573**

A supplementary spectral input sensitivity experiment (Section 4.2.3) evaluated the exclusion of the 15 interpolated water-absorption channels. The 281-band input achieved an NPV F1-score of 0.409, compared with 0.461 for the corresponding 296-band M5 configuration.

5.1.3. Matched spatial-resolution performance

Resampling MICA from its native 5 cm resolution to 10 cm reduced NPV F1 from 0.725 to 0.539, mean F1 from 0.886 to 0.772, and mIoU from 0.812

to 0.667 (Table 11). At the matched 10 cm resolution, MICA still exceeded the combined 296-band FX10–FX17 input by 0.078 in NPV F1, 0.067 in mean F1, and 0.094 in mIoU. These results indicate that spatial resolution contributed substantially to the native MICA advantage but did not fully account for the performance difference between the sensor inputs.

Table 11: Source-site performance of M5 at native and matched spatial resolutions. The matched comparison used MICA resampled to 10 cm and the combined 296-band FX10–FX17 input at 10 cm; native 5 cm MICA is included as a reference. Values are means of the three fold-level test metrics.

Input configuration	Resolution	BE F1	NPV F1	PV F1	Mean F1	BE IoU	NPV IoU	PV IoU	mIoU
MICA, native (reference)	5 cm	**0.963**	**0.725**	**0.969**	**0.886**	**0.928**	**0.568**	**0.941**	**0.812**
MICA, resampled	10 cm	0.904	0.539	0.874	0.772	0.828	0.384	0.788	0.667
FX10–FX17, combined 296-band input	10 cm	0.846	0.461	0.807	0.705	0.737	0.300	0.681	0.573

5.1.4. Qualitative within-site predictions and uncertainty

Qualitative analysis first examined model-variant and patch-scale effects on tile 65, a mixed-cover tile containing BE–NPV–PV transitions and heterogeneous vegetation–background structure. Predictions from M1, M3, and M5 were compared across patch scales of 152, 224, and 304 px (Fig. 5).

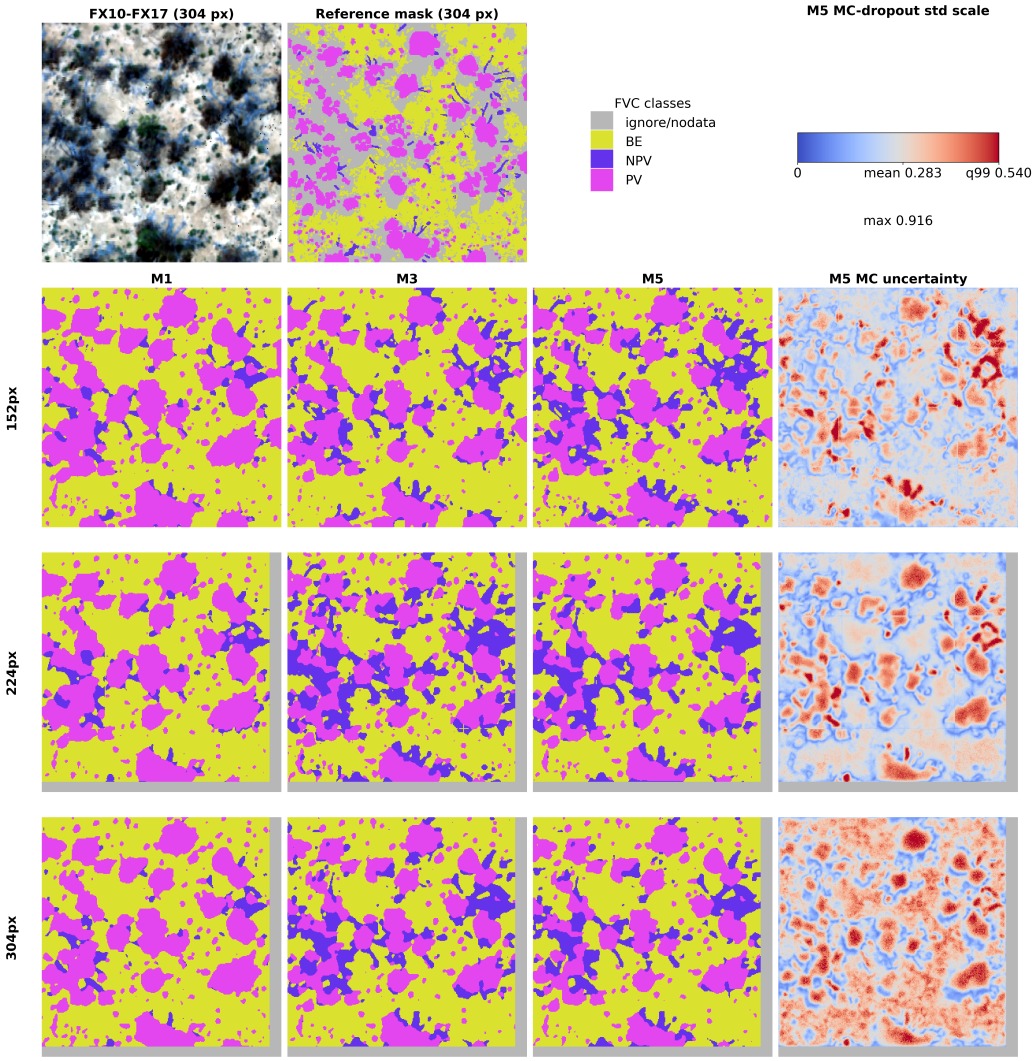


Figure 5: Within-site inference and epistemic uncertainty for tile 65 using the FX10–FX17 sensor profile. The top row shows the RGB composite, reference mask, class legend, and M5 Monte Carlo dropout uncertainty scale; subsequent rows show M1, M3, and M5 predictions at 152, 224, and 304 px. The final column shows M5 uncertainty at each patch scale. Grey pixels denote ignore/nodata areas, and the uncertainty colour scale is clipped at the 99th percentile for visualisation.

M3 and M5 produced more continuous NPV regions than M1. The 152 px outputs retained smaller spatial features, whereas the 224 px and 304 px outputs appeared more spatially regularised. M5 uncertainty was concen-

trated around class transitions, mixed pixels, small vegetation fragments, and nodata-adjacent areas.

The analysis then compared the selected M5 sensor configurations: native 5 cm MICA at 304 px and combined 296-band FX10–FX17 at 152 px. Their outputs were displayed over the same approximate ground footprint while retaining their native spatial resolutions (Fig. 6).

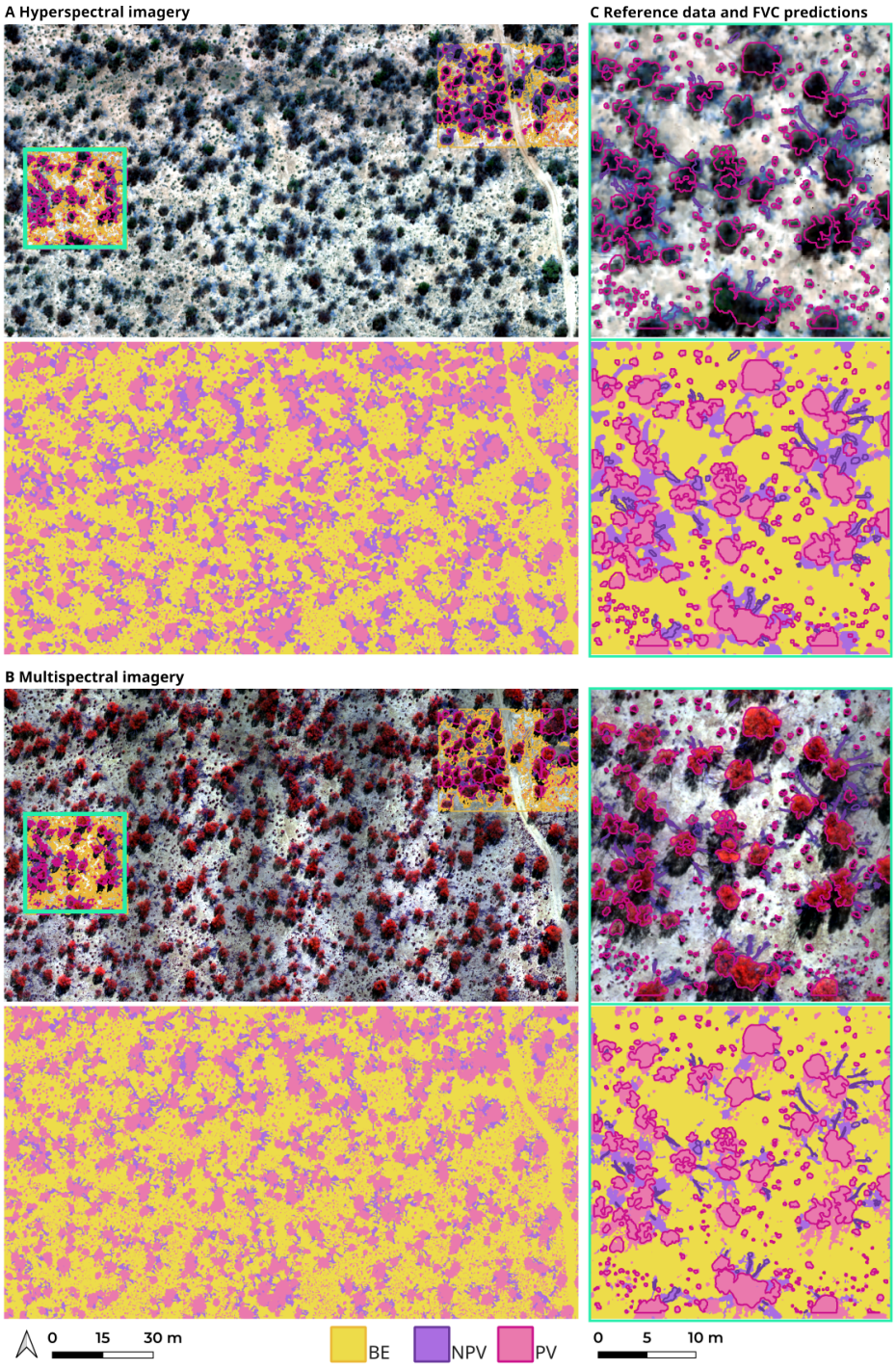


Figure 6: Ground-footprint-matched visual comparison of FX10–FX17 hyperspectral and MICA multispectral FVC inference. **A** Combined FX10–FX17 imagery and predictions at 10 cm; **B** MICA imagery and predictions at 5 cm. Both configurations are displayed over a 15.2 m $\times$ 15.2 m ground extent, with reference annotations overlaid on the imagery. **C** Enlarged subsets show local correspondence between reference and predicted FVC patterns.

Both sensor configurations mapped the dominant BE, NPV, and PV patterns, with local differences around mallee crowns, stem branches, and mixtures of bare earth and litter. Monte Carlo dropout uncertainty further characterised the spatial stability of these predictions (Fig. 7).

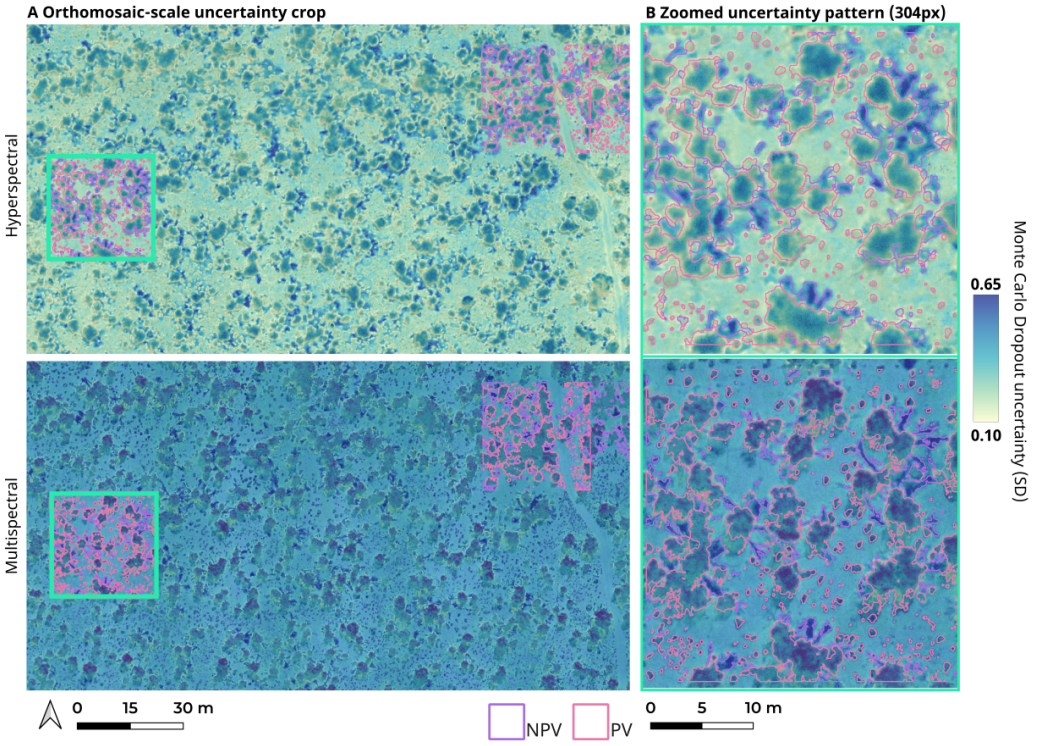


Figure 7: Monte Carlo dropout epistemic uncertainty for FX10–FX17 at 10 cm (top) and MICA at 5 cm (bottom). **A** Orthomosaic-scale uncertainty crops; **B** enlarged views of the green inset. NPV and PV boundaries are overlaid in purple and pink, respectively. All panels use the same colour ramp and display limits of 0.10–0.65; values outside this range are clipped for display only.

FX10–FX17 produced a more spatially coherent uncertainty surface, with elevated values concentrated around vegetation transitions, exposed bare ground or litter, and heterogeneous shrub structure. MICA retained finer object-level detail but showed greater local fragmentation. Across the full unscaled uncertainty rasters, NPV had the highest Monte Carlo dropout standard deviation for both sensors, followed by PV and BE. The BE, NPV, and PV values were 0.0739, 0.1388, and 0.0932 for FX10–FX17 and 0.0610, 0.1091, and 0.0759 for MICA, respectively.

5.1.5. Cross-site validation

Zero-shot performance varied substantially among the frozen source-site configurations (Table 12). Among the CNN models, native 5 cm MICA achieved the highest macro F1 (0.654) and mIoU (0.610), driven by strong BE and PV performance, although its NPV F1 remained low at 0.072. Resampled 10 cm MICA achieved the highest CNN-based NPV F1 (0.118), while the FX10–FX17 152 px configuration retained moderate aggregate performance despite an NPV F1 of only 0.010. The FX10–FX17 304 px configuration showed the greatest aggregate degradation. Random Forest NPV F1 ranged from 0.079 to 0.120, with lower macro F1 and mIoU than the stronger CNN configurations. Across all evaluated pipelines, the highest external-site NPV F1 was therefore only 0.120, indicating consistently weak NPV transfer.

Table 12: Zero-shot performance on five external SASMDD0013 tiles. CNN M5 values are per-tile means for each selected source-site checkpoint; Random Forest values are means of the three fold-matched models.

Model	Configuration	BE F1	NPV F1	PV F1	Macro F1	mIoU
CNN M5	MICA, 5 cm, 304 px	**0.949**	0.072	**0.942**	**0.654**	**0.610**
CNN M5	MICA, 10 cm, 304 px	0.829	0.118	0.904	0.617	0.530
CNN M5	FX10–FX17, 152 px	0.925	0.010	0.665	0.533	0.455
CNN M5	FX10–FX17, 304 px	0.001	0.070	0.443	0.171	0.107
Random Forest	MICA, 5 cm	0.125	0.079	0.869	0.357	0.292
Random Forest	MICA, 10 cm	0.454	**0.120**	0.813	0.462	0.351
Random Forest	FX10–FX17	0.459	0.115	0.738	0.438	0.333

The spatial expression of these transfer results was examined using corresponding cross-site prediction maps (Fig. 8). The comparison included both FX10–FX17 patch scales and the native-resolution MICA 304 px output.

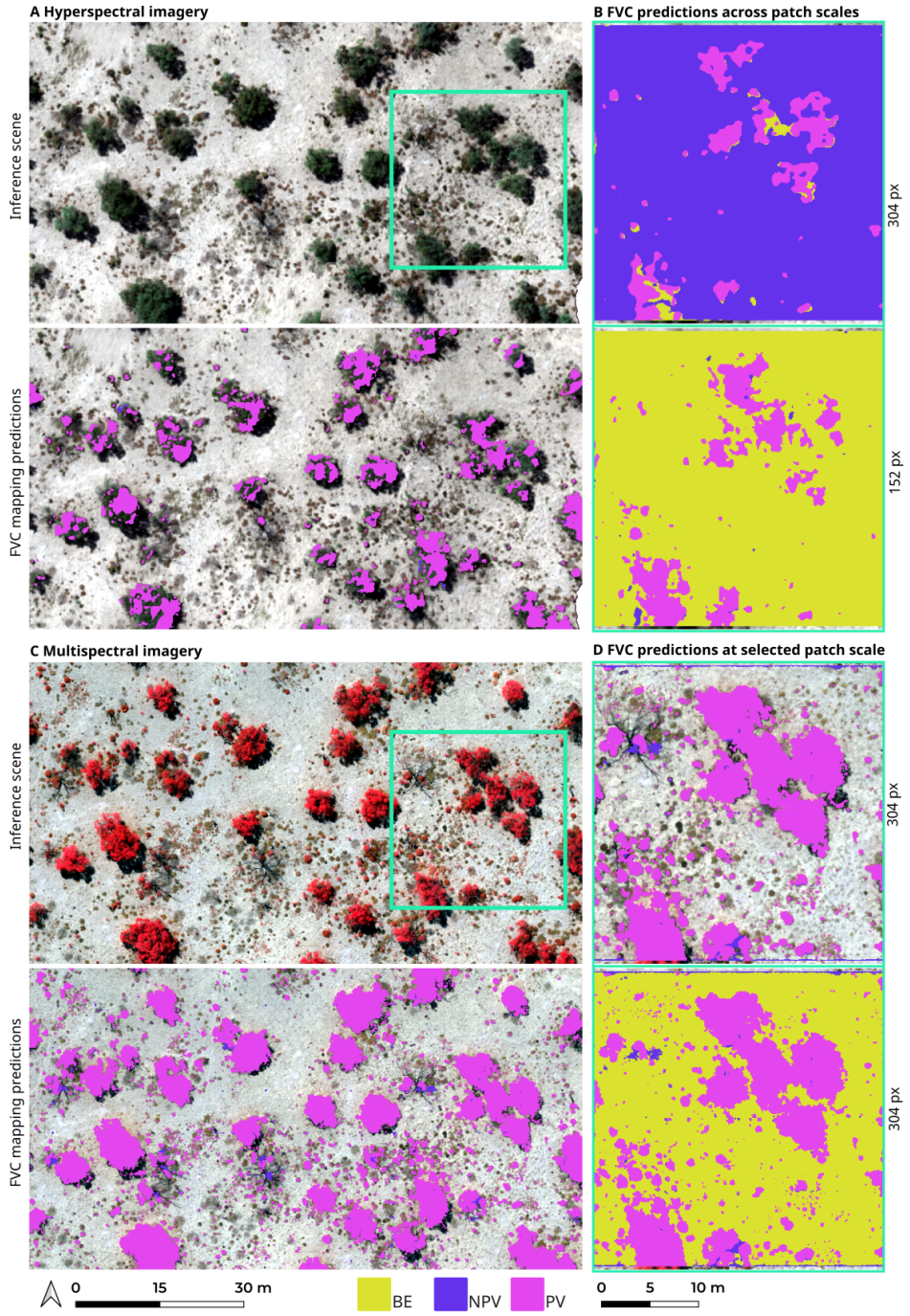


Figure 8: Cross-site FVC inference examples for M5 configurations using FX10–FX17 hyperspectral and MICA multispectral inputs. **A** External-site FX10–FX17 imagery and prediction; **B** enlarged subset comparing the 304 px and 152 px outputs. **C** Corresponding MICA imagery and prediction; **D** enlarged MICA 304 px output. Cyan boxes indicate the enlarged subsets, and prediction panels show BE, NPV, and PV.

Within the highlighted FX10–FX17 subset, the 152 px output retained more local structure and mapped most bright exposed ground as BE while preserving localised NPV and PV patches. The 304 px output instead assigned much of the same area to a broad contiguous NPV region, consistent with its poor external-site metrics and indicating NPV overgeneralisation. The MICA output showed stronger aggregate transfer, but its advantage was likewise concentrated in BE and PV rather than NPV.

5.2. Post-inference spectral characterisation results

Following the analytical sequence described in Section 4.3, the results progress from class-wise reflectance and separability to uncertainty- and confusion-stratified spectra, spectral-index maps, and model-derived spectral importance.

5.2.1. Reflectance response and class separability

The class-wise reflectance analysis showed distinct but partially overlapping spectral responses for BE, NPV, and PV across the MICA and FX10–FX17 datasets (Fig. 9). BE generally had higher reflectance than the vegetation classes, particularly across the red-edge, NIR, and SWIR regions. In the MICA data, PV had lower reflectance than NPV in the visible and red-edge bands, but higher reflectance in the NIR band. In the FX10–FX17 data, PV and NPV showed similar reflectance across parts of the red-edge and NIR transition, with greater separation in selected SWIR wavelengths.

Pairwise separability varied by wavelength. In the MICA data, BE–PV and BE–NPV differences were largest across the visible to red-edge wavelengths, whereas NPV–PV differences were smaller near the red-edge/NIR transition. In the FX10–FX17 data, BE–PV differences were high across much of the VNIR–SWIR range and increased again at longer SWIR wavelengths. BE–NPV differences were largest in the visible to red-edge region and decreased through parts of the NIR–SWIR range. NPV–PV differences were lowest across parts of the red-edge and NIR, but increased in selected SWIR wavelengths.

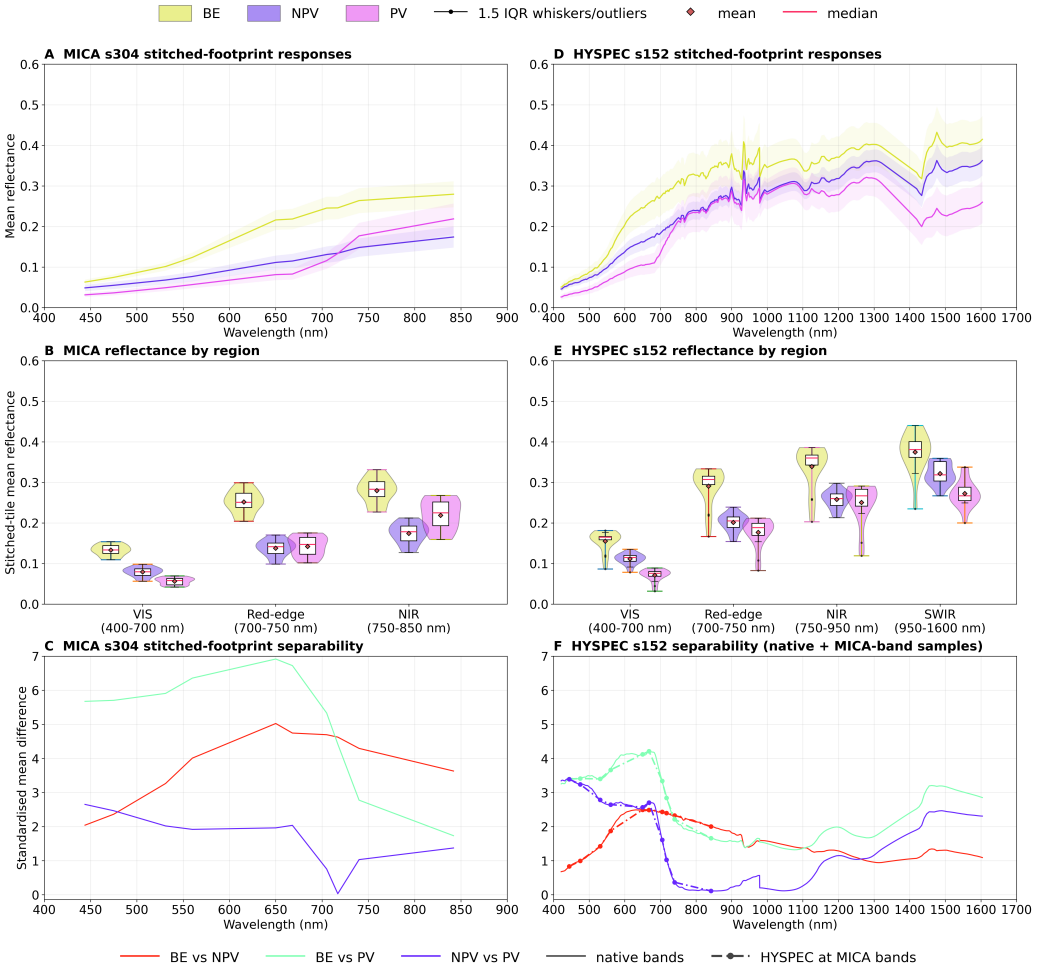


Figure 9: Class-wise spectral response, regional reflectance, and pairwise separability of predicted FVC classes derived from reflectance values. **A** and **D** show mean reflectance signatures for BE, NPV, and PV for the MICA and FX10–FX17 datasets, respectively. The shaded envelopes in **A** and **D** show the mean reflectance ± one standard deviation (SD) at each wavelength, calculated across the contributing tile-level class spectra. **B** and **E** summarise class-wise reflectance distributions by broad spectral region. **C** and **F** show standardised pairwise mean differences across wavelength. In **F**, solid lines show native FX10–FX17 bands and point markers indicate the nearest FX10–FX17 samples to the MICA band positions.

5.2.2. Spectral composition of high-uncertainty and confused NPV pixels

NPV showed the strongest uncertainty stratification among the three classes (Section 4.3.2; Fig. Appendix A.1 in Appendix A). In the stitched

inference tile, the mean epistemic uncertainty of the high-uncertainty NPV stratum was 0.54, compared with 0.33 for BE and 0.40 for PV, and the class-wise 75th-percentile uncertainty threshold for NPV (0.45) exceeded those of BE (0.28) and PV (0.34). High-uncertainty NPV pixels were consistently brighter than low-uncertainty NPV pixels across the full spectral range, for example 0.470 compared with 0.353 at 1600 nm, and were displaced toward the BE signature. In contrast, high-uncertainty PV pixels were darker than their low-uncertainty counterparts.

On the spatially held-out block-1 test tiles, pixels predicted as NPV comprised 40.4% correct NPV, 40.2% reference BE, and 19.4% reference PV. The NPV-predicted pixels labelled BE in the reference were spectrally intermediate between correct NPV and correct BE at all wavelengths, for example 0.443 at 1600 nm compared with 0.407 for correct NPV and 0.505 for correct BE. In contrast, NPV-predicted pixels labelled PV showed lower SWIR reflectance than correct NPV, 0.299 compared with 0.361 near 1450 nm. In the inference-tile analysis, the mean uncertainty of pixels predicted as NPV but labelled BE was 0.43, the same reported value as correctly classified NPV (0.43) and higher than correct BE (0.27) and correct PV (0.30).

5.2.3. Spectral-index maps in inference tiles

The post-inference spectral-index maps showed distinct spatial patterns relative to the predicted FVC classes in the representative FX10–FX17 inference tile (Fig. 10). kNDVI and NDRE showed higher relative values over shrub crowns and PV-dominated prediction regions, consistent with stronger greenness, photosynthetic activity, and red-edge responses. PSRI and MSI showed higher relative values in areas associated with dry vegetation, litter-covered ground, and mixed vegetation background surfaces, consistent with pigment-transition and moisture or dry-material variation. BSI showed higher relative values over exposed substrate and BE-dominated prediction regions. The strongest spatial contrasts occurred around shrub boundaries and mixed BE–NPV–PV areas, where the index maps highlighted fine-scale transitions between live vegetation, dry vegetation, and exposed background.

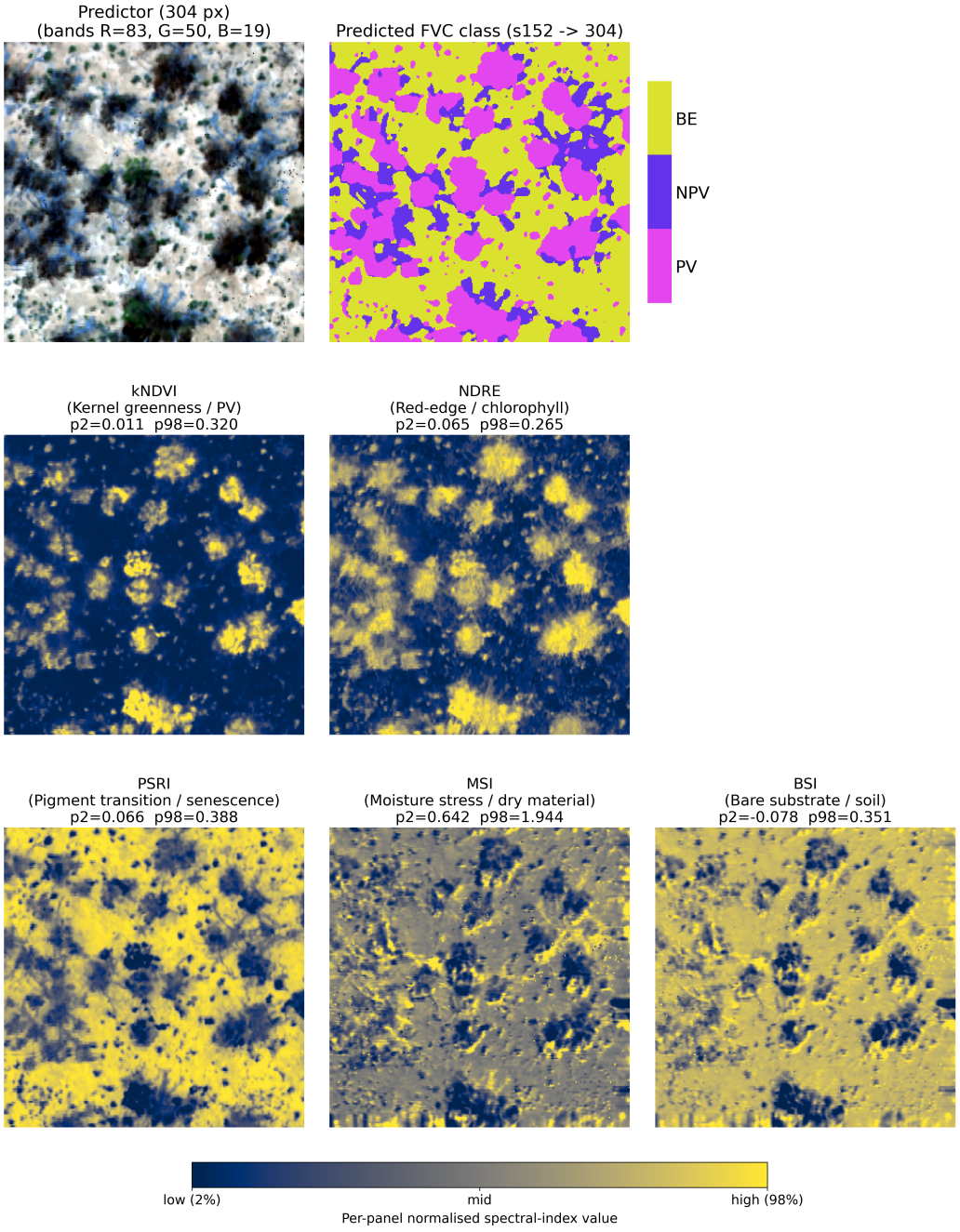


Figure 10: Representative FX10–FX17 inference tile showing the false-colour predictor, predicted FVC class map, and post-inference spectral-index maps. The predicted FVC map shows BE, NPV, and PV classes. Spectral-index maps were calculated from the retained reflectance bands and displayed using per-panel 2–98% percentile-normalised scaling. Colours indicate relative low-to-high values within each index map and are not directly comparable between indices.

5.2.4. Model-derived spectral importance

The learned input gate and gradient-based class sensitivities provided complementary importance summaries. For the combined 296-band FX10–FX17 input, the gate yielded a class-agnostic profile of learned band weights (Fig. Appendix A.2 in Appendix A), whereas the gradient-based scores produced class-specific rankings for both sensor models (Fig. 11). For MICA, the highest-ranked bands for BE, NPV, and PV were centred in the red, red-edge, and NIR regions, including wavelengths near 668, 705, 717, 740, and 842 nm. For FX10–FX17, the highest-ranked wavelengths were concentrated mainly in the NIR–SWIR range. BE importance was highest at longer SWIR wavelengths, particularly around 1476–1590 nm. PV and NPV importance was concentrated mainly around 1265–1321 nm, with NPV also showing high importance near 1476 nm. These rankings represent relative model-output sensitivities rather than direct measures of vegetation or substrate biophysical properties.

The model-agnostic permutation analysis independently assessed these patterns at regional and 25 nm-window scales. Jointly permuting the SWIR region produced the largest overall degradation (ΔF1 of 0.47 for BE, 0.42 for NPV, and 0.57 for PV), the VIS region was most important for PV (ΔF1 = 0.71) and NPV (0.49), and the NIR region was more important for NPV (0.40) than for PV (0.22) or BE (0.05), whereas the red-edge contributed little at region level (ΔF1 $\leq$ 0.03). Permuting the 15 interpolated water-absorption channels produced no degradation (ΔF1 $\leq$ 0), consistent with the 281-band exclusion experiment. At the 25 nm window level, NPV was most sensitive to windows near the NIR–SWIR transition (979–1027 and 1083–1104 nm) and at 575–597 nm, and PV to the 1455–1476 nm shoulder of the water-absorption feature. Because neighbouring hyperspectral bands are strongly correlated, permuting a single narrow window can be partially compensated by adjacent bands, so window-level scores emphasise less redundant spectral transitions, whereas region-level scores confirm the broader VIS and NIR–SWIR dependence identified by the gradient-based rankings.

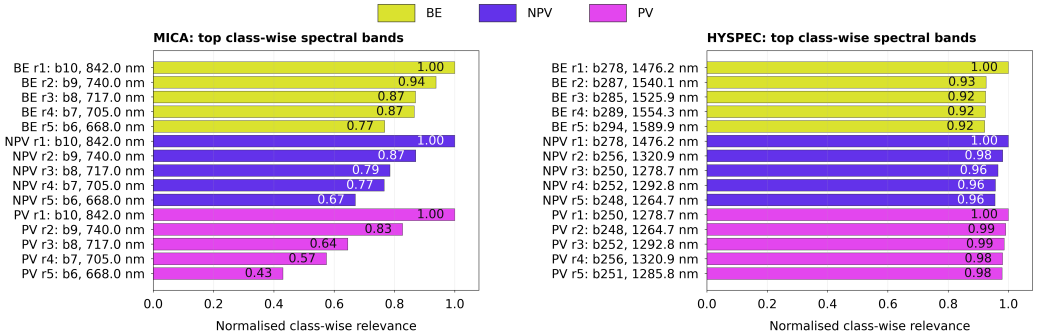


Figure 11: Top class-wise spectral-importance bands and wavelengths for BE, NPV, and PV predictions. Importance scores were normalised within each class and sensor profile. The MICA rankings show the highest-ranked multispectral bands, and the FX10–FX17 rankings show the highest-ranked hyperspectral wavelengths for each predicted class.

5.3. Edge deployment performance

ONNX Runtime reproduced the PyTorch outputs exactly within the reported precision for both sensors, with 100.00% argmax agreement and mIoU of 1.00. TensorRT FP32 also preserved the PyTorch predictions, with 100.00% agreement for FX10–FX17 s152 and near-perfect agreement for MICA s304. Pure FP16 TensorRT engines produced non-finite logits and were therefore not considered deployment-ready. The validated FP16-labelled TensorRT engines produced larger logit differences, as expected from reduced-precision execution, but maintained high argmax consistency with the PyTorch reference.

Table 13: TensorRT edge-deployment summary for the selected FVC segmentation models on Jetson AGX Orin. Engine size refers to the serialized TensorRT engine footprint. Agreement and mIoU were computed relative to the PyTorch argmax predictions. Latency speed-up was calculated relative to the corresponding TensorRT FP32 median latency. FP16-labelled rows correspond to validated mixed FP16/FP32 TensorRT engines rather than pure FP16 engines. Full logit-level and argmax-level parity diagnostics are provided in Supplementary Table Appendix B.2.

Sensor	**Engine**	**Size (MiB)**	**Latency (ms)**	**Throughput (tiles s^{-1})**	**Speed-up (×)**	**Agree (%)**	**mIoU**
FX10–FX17 s152	TRT FP32	133.77	16.31	65.51	1.00	100.00	1.00
FX10–FX17 s152	TRT FP16	93.71	9.62	116.02	1.70	99.96	1.00
MICA s304	TRT FP32	159.89	46.71	21.42	1.00	100.00	1.00
MICA s304	TRT FP16	204.70	52.05	19.22	0.90	99.99	1.00

For the FX10–FX17 s152 model, the validated FP16-labelled TensorRT engine reduced median per-tile latency from 16.31 to 9.62 ms, increased throughput from 65.51 to 116.02 tiles s^{-1}, and preserved 99.96% argmax agreement with the PyTorch reference. This represented a 1.70× latency speed-up and reduced the serialized engine footprint from 133.77 to 93.71 MiB.

In contrast, the MICA s304 FP16-labelled engine was slower than its FP32 baseline. Median latency increased from 46.71 to 52.05 ms, throughput decreased from 21.42 to 19.22 tiles s^{-1}, and the serialized engine footprint increased from 159.89 to 204.70 MiB. Although prediction parity remained high, the FP16-labelled configuration did not provide a deployment advantage for this model.

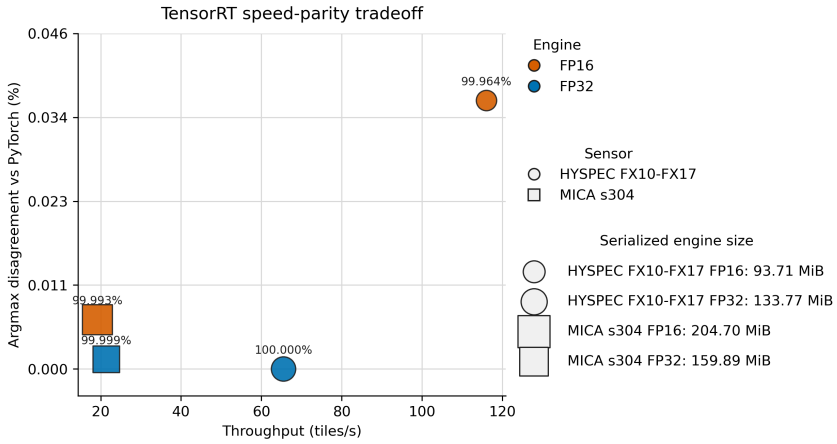


Figure 12: TensorRT speed–parity trade-off on Jetson AGX Orin. The x-axis shows throughput in tiles s^{-1}, and the y-axis shows argmax disagreement relative to the PyTorch reference, computed as 100−pixel-wise agreement. Marker colour denotes TensorRT engine precision, marker shape denotes sensor, and marker size indicates serialized engine size. Text labels show pixel-wise agreement with PyTorch. Points closer to the lower-right indicate higher throughput with stronger prediction parity.

Together, the deployment results show that TensorRT precision selection was model dependent. FP16-labelled mixed precision improved latency, throughput, and engine size for the hyperspectral FX10–FX17 s152 model while preserving high prediction parity with PyTorch. For the multispectral MICA s304 model, FP32 remained the preferred deployment configuration because it provided lower latency, higher throughput, smaller engine size, and marginally stronger agreement with the PyTorch reference. Detailed ONNX

export metadata, TensorRT engine validation status, full parity diagnostics, supplementary latency-throughput diagnostics, and representative tile-level parity maps are provided in Appendix B.

6. Discussion

6.1. NPV-aware FVC segmentation and PV–NPV discrimination

We demonstrated an NPV-aware CNN workflow with spectral-channel adaptation for mapping fractional vegetation cover from multi-sensor UAS optical imagery in semi-arid vegetation. This addresses a central challenge in dryland remote sensing: although PV, NPV, and BE are all ecologically meaningful components of vegetation cover, NPV is often the most difficult to map because it comprises dry or senescent vegetation, litter, coarse woody debris, and standing dead woody material, whose spectral and spatial characteristics can overlap with shadows, exposed substrate, and mixed vegetation–soil pixels (Lewis et al., 2001; Fisk et al., 2019a; Melville et al., 2019a; Li et al., 2023; Sotomayor et al., 2025a). By extending a U-Net-based FVC segmentation framework with spectral-channel adaptation, NPV-weighted optimisation, data augmentation, and patch-scale evaluation, the workflow provides a controlled basis for assessing how model design, class imbalance, spatial context, training variability, and sensor configuration affect PV–NPV–BE discrimination.

6.1.1. Baseline ablations and NPV-weighted optimisation

The M1–M5 ablation results (Section 5.1.1) identify NPV-weighted optimisation as the primary driver of improved NPV performance. Relative to the plain U-Net baseline M1 using the combined 296-band input, the unweighted spectral-adapter variant M2 produced only a small improvement, while adding cross-channel attention without weighting in M4 left aggregate performance approximately equivalent to the baseline. In contrast, the NPV-weighted variants M3 and M5 produced substantially larger increases in NPV F1, mean F1, and mIoU. M5 achieved the highest aggregate NPV F1, whereas M3 achieved the highest aggregate mean F1 and mIoU. These values summarise performance across sensor profiles and patch scales, rather than the single combined FX10–FX17 configuration used in the baseline-method comparison.

The spectral adapter provided a band-aware projection before spatial decoding through an SE-reweighted 1×1 convolutional stem, allowing sensor-

specific channel combinations to be learned before the U-Net encoder–decoder. Lightweight cross-channel attention extended this learned representation in M4 and M5. However, the small aggregate differences between M3 and M5 do not establish a consistent advantage for the additional attention component. Spectral-channel adaptation and cross-channel attention are therefore best interpreted as supporting components within a class-weighted segmentation framework, rather than as independent solutions to NPV ambiguity. This interpretation is consistent with UAS vegetation segmentation studies that emphasise balancing spatial feature learning, annotation efficiency, and sensor-specific spectral representation rather than relying only on increasingly complex architectures (Kattenborn et al., 2019a, 2021; Chowdhury et al., 2027).

The separate matched weight-sensitivity experiment (Appendix A.1) strengthens this interpretation by varying only the loss weights for the fixed spectral-adapter and cross-channel-attention architecture. Mean held-out NPV F1 increased from 0.331 with $[1, 1, 1]$ to 0.442 with $[1, 2, 1]$. These separately retrained configurations are distinct from the original ablation and external benchmark. Increasing the NPV coefficient from 2 to 3 raised recall but reduced precision on both validation and test data. The $[1, 2, 1]$ configuration was selected for its stronger validation balance across NPV F1 and aggregate metrics; although $[1, 3, 1]$ achieved higher held-out NPV F1, the test results were not used for weight selection. The selected weights should therefore not be interpreted as universally optimal outside the present dataset and training configuration.

Data augmentation was shared across the CNN-based experiments rather than tested as an independent ablation factor. Variation in object orientation, patch composition, brightness, contrast, and shadow conditions may have supported robustness to illumination and spatial variability, consistent with previous CNN-based vegetation remote sensing studies (Kattenborn et al., 2019a; Schiefer et al., 2020; Möhring et al., 2025; Sotomayor et al., 2025a). Its contribution cannot, however, be quantified separately from the other components of the training protocol.

6.1.2. Baseline-method comparison and spectral compression

The baseline-method comparison (Section 5.1.2; Table 10) extends the internal ablation by comparing traditional per-pixel classification, PCA-compressed inputs, and a published spectral–spatial CNN against the plain U-Net reference and M5 using the combined 296-band FX10–FX17 input. Random

Forest and SS3FCN remained competitive in aggregate performance, while the principal advantage of M5 was higher NPV F1. SS3FCN achieved the highest BE F1 and the plain U-Net achieved the highest PV F1, so M5 did not improve performance uniformly across classes.

The competitiveness of Random Forest shows that individual pixel spectra provided a useful within-site classification baseline even without spatial context. It does not isolate the contribution of spatial modelling, because Random Forest and the CNN-based models also differed in training objectives and learning procedures. M5 used NPV-weighted focal loss, the CNN-based baseline configurations used unweighted focal loss, and Random Forest used no class weighting or augmentation. Together with the separate weight-sensitivity results, the benchmark supports the value of the complete NPV-aware pipeline rather than architectural superiority alone.

The PCA results also clarify the relationship between spectral redundancy and classification performance. Although the leading principal components retained almost all of the total spectral variance, the PCA-compressed inputs underperformed the combined 296-band input, particularly for NPV, indicating that variance retention alone is insufficient to assess the suitability of spectral compression for this task and that lower-variance components may contain information useful for NPV discrimination. These results do not establish whether the performance differences arose from discarded discriminative information, differences in optimisation, or training variability. It is also important to distinguish three different operations: variance-based dimensionality reduction (PCA), supervised spectral compression, and statistical decorrelation. The spectral adapter in the proposed pipeline compresses the 296 input bands into 32 feature channels learned through supervised training; these features are optimised for class discrimination but are not constrained to be statistically uncorrelated. The comparison therefore does not establish that the adapter eliminates multicollinearity, nor does it independently isolate the adapter's contribution from the rest of the pipeline.

The water-absorption channel exclusion experiment provides a complementary input-sensitivity check. Removing the 15 interpolated channels reduced NPV F1 from 0.461 to 0.409 under the tested conditions (Section 4.2.3). This finding does not show that interpolation recovered reliable measured reflectance or that those channels are intrinsically necessary for NPV discrimination. It indicates only that exclusion did not improve the evaluated pipeline; alternative treatment of unreliable channels remains a separate modelling question.

6.1.3. Spatial resolution, patch scale, and sensor configuration

The matched-resolution results (Section 5.1.3) clarify the spatial–spectral trade-off between MICA and FX10–FX17. Resampling MICA from 5 cm to 10 cm reduced all reported segmentation metrics, indicating a substantial resolution-associated contribution to its native-resolution advantage. However, MICA retained an mIoU advantage of 0.094 over combined FX10–FX17 after both were evaluated at 10 cm. This residual difference does not establish inherent multispectral superiority because radiometric response, wavelength placement, signal-to-noise characteristics, preprocessing, and model–sensor interactions remained unmatched. Broader FX10–FX17 VNIR–SWIR coverage instead provided complementary information for interpreting dry vegetation, substrate mixtures, and moisture-sensitive variation. The relative value of spatial and spectral information therefore depended on both target-class separability and the spatial context available to the model (Kattenborn et al., 2019a; Schiefer et al., 2020).

The Monte Carlo dropout uncertainty maps provide an additional qualitative diagnostic of the sensor comparison. MICA uncertainty was more locally fragmented, whereas FX10–FX17 uncertainty was more spatially coherent. These patterns are consistent with differences in spatial sampling and local surface heterogeneity, but they do not establish that broader spectral coverage produced better-calibrated confidence. Interpretation of the uncertain pixels requires the reflectance and confusion analyses discussed in Section 6.2.

Patch-scale effects further separated aggregate accuracy from spatial prediction detail (Section 5.1.4). Larger patches generally produced stronger aggregate metrics and more regularised predictions, whereas the 152 px outputs retained smaller NPV fragments, vegetation–soil mixtures, and local class boundaries. Broader spatial context may therefore stabilise class assignment while smoothing fine-scale heterogeneity. This interpretation is consistent with studies showing that image resolution and patch scale jointly determine the spatial context available to segmentation models (Möhring et al., 2025; Braham et al., 2025), although the present UAS input patches are not directly equivalent to internal transformer token sizes.

6.1.4. Zero-shot cross-site transfer

The external-site results (Table 12) show that within-site competitiveness did not ensure NPV transfer. Across the evaluated CNN-based and Random Forest configurations, NPV F1 remained low at 0.010–0.120, even where BE

and PV transferred comparatively well. Thus, stronger aggregate performance at the external site should not be interpreted as successful mapping of all three FVC components. The shared NPV difficulty across different model families and sensor inputs suggests that site-dependent spectral and reference data differences contributed to the transfer limitation, but the experiments do not isolate a single cause.

Patch-scale behaviour also changed under transfer: the FX10–FX17 304 px configuration degraded substantially, while the selected 152 px output retained more local BE–NPV structure. Broader context therefore cannot be assumed to improve generalisation simply because it improved aggregate within-site metrics. The cross-site CNN results used selected source-site checkpoints, whereas Random Forest results were averaged across three source-site fold models, so they should not be treated as a fully matched ranking of model families.

Three-fold spatial block cross-validation reduced dependence between source-site training and evaluation samples, whereas zero-shot evaluation at SAS-MDD0013 assessed geographic transfer without target-site parameter updates. Neither evaluation demonstrates that spatial autocorrelation was eliminated or that the learned representations were universally transferable, and the five reviewed external tiles do not represent the full range of target-site conditions. Target-site fine-tuning and domain-adaptation strategies, together with larger multi-site evaluations, remain future work. The spectral analyses below help interpret the residual NPV ambiguity without assuming that within-site spectral patterns explain every external-site error.

6.2. Spectral characterisation and model interpretability

The post-inference spectral characterisation workflow provided diagnostic evidence for interpreting CNN-predicted FVC classes, with particular emphasis on the spectrally ambiguous NPV component. Class-wise reflectance and separability, uncertainty- and confusion-stratified spectra, spectral-index maps, and model-derived gate, gradient, and permutation importance linked predicted BE, NPV, and PV patterns to observable spectral behaviour.

The post-inference spectral analysis was most useful for explaining why NPV remained difficult, rather than simply confirming which model achieved the highest segmentation accuracy. In the MICA data, class differences were concentrated mainly in the visible, red-edge, and NIR bands. These regions provide contrast related to greenness, chlorophyll-sensitive response, canopy scattering, and vegetation–substrate separation (Homolová et al.,

2013; Melville et al., 2019a; Sotomayor et al., 2025a). This helps explain the strong within-site performance of the high-resolution multispectral configuration. However, VIS–NIR information alone does not uniquely isolate dry vegetation material, particularly where NPV overlaps with exposed soil, woody debris, shadows, and mixed vegetation–soil backgrounds. Therefore, strong multispectral segmentation performance should not be interpreted as evidence that NPV is spectrally unambiguous in the VIS–NIR domain.

The FX10–FX17 results extended the diagnostic evidence into the SWIR, where reflectance responses, pairwise separability, and model-derived spectral importance scores provided additional contrast for NPV and substrate-related mixtures. Because the FX10–FX17 predictions were generated at the stitched-prediction support, spectral separability was interpreted primarily at the same prediction scale. Native hyperspectral pixels can describe finer-scale spectral variability, but they were not treated as the primary basis for explaining prediction-scale class separability. This distinction is important because separability estimated at the native hyperspectral pixel scale may reflect intrinsic spectral detail that is not fully preserved in the stitched prediction units.

The uncertainty- and confusion-stratified spectra extend this class-level interpretation to the pixels associated with uncertain predictions and classification errors (Section 5.2.2). High-uncertainty NPV predictions were brighter and displaced toward the BE signature, while pixels predicted as NPV but labelled BE on the held-out test tiles had spectra intermediate between correctly classified NPV and BE. These patterns are consistent with mixtures of dry vegetation and exposed soil. Pixels predicted as NPV but labelled PV had lower SWIR reflectance, which may reflect residual moisture in partially senescent vegetation. The darker spectra of high-uncertainty PV predictions are also consistent with shadow effects. Together, these observations suggest that vegetation–soil mixtures, senescence transitions, and illumination differences contribute to NPV ambiguity, but they do not identify the relative contributions of dry grass, litter, or woody debris.

The two analyses provide complementary evidence rather than an independent validation of the uncertainty estimates. The uncertainty-stratified spectra were extracted from a qualitative inference tile in the block-1 training partition, whereas the confusion-stratified spectra describe errors on spatially held-out test tiles. Agreement between their spectral patterns supports an interpretation of NPV difficulty in terms of surface heterogeneity, but does not establish that ecological mixtures are the principal cause of epistemic

uncertainty or exclude model-related effects. Subclass reference labels and uncertainty rasters on held-out tiles would be needed to test those relationships directly.

The spectral-index maps provide spatial context for these reflectance patterns. Higher kNDVI and NDRE values in PV-dominated shrub crowns are consistent with greenness and red-edge responses, whereas PSRI and MSI variation around dry vegetation and mixed backgrounds suggests pigment-transition and moisture-related contrasts. BSI highlights exposed-substrate patterns that can help interpret BE–NPV transitions. Because these indices were calculated from the same predictor imagery and displayed with per-panel normalisation, they provide complementary spectral diagnostics rather than independent evidence of class accuracy or quantitative measurements of vegetation condition.

The model-derived analyses provided three complementary views of wavelength importance (Section 5.2.4). The learned gate summarised class-agnostic band weighting, gradient sensitivities identified class-specific contributions to model logits, and permutation importance measured the loss of class performance after disrupting spectral regions or windows. Gradient importance was elevated around 1265–1321 nm and 1476–1590 nm, regions consistent with known dry-material, water-sensitive, substrate-related, and senescence-associated responses (Lewis et al., 2001; Homolová et al., 2013; Turner et al., 2023; Haynes et al., 2026). The first region lies on the NIR plateau between water-absorption features near 1200 and 1450 nm, while the second covers the long-wavelength shoulder of the 1450 nm water feature and overlapping O–H and C–H overtones associated with dry carbohydrates (Curran, 1989; Homolová et al., 2013).

Regional permutation results supported a broader VIS and NIR–SWIR dependence, while the weak red-edge and interpolated water-absorption responses showed that high gradient or gate relevance should not automatically be interpreted as indispensable predictive information. Correlation among neighbouring hyperspectral bands also allows adjacent wavelengths to compensate when narrow windows are permuted. Agreement among gate, gradient, and permutation outputs therefore strengthens regional interpretation, but none of these diagnostics establishes a direct biophysical retrieval.

The strongest ligno-cellulose diagnostics for separating plant litter from soil, including the cellulose–lignin absorption near 2100 nm that underlies the cellulose absorption index and the related feature near 2300 nm, lie beyond the 1700 nm limit of the FX17 sensor (Nagler et al., 2000; Asner and Lobell,

2000). NPV discrimination therefore relied on weaker water- and dry-matter-related features within 900–1700 nm, which may partly explain the residual confusion between cellulose-dominated dry grass and litter, lignin-rich woody debris, and exposed substrate. Spaceborne imaging spectroscopy missions such as PRISMA and EnMAP cover these 2100 and 2300 nm features at approximately 30 m spatial resolution (Guanter et al., 2015; Chabrillat et al., 2024), but that spatial scale reintroduces the mixed-pixel conditions that the sub-10 cm UAS data used here were designed to minimise. The two observation scales are therefore complementary: fine-resolution UAS FVC products can provide subpixel reference fractions for full-range spaceborne retrievals, while spaceborne SWIR coverage can supply the ligno-cellulose diagnostics unavailable below 1700 nm. The spectral-importance outputs should therefore be treated as diagnostic summaries of model sensitivity rather than direct retrievals of vegetation physiological traits.

Together, the spectral analyses explain class ambiguity rather than sensor superiority: broader VNIR–SWIR coverage improved interpretation of dry vegetation, substrate mixtures, and class transitions, whereas finer spatial detail supported sharper within-site segmentation.

6.3. Edge-inference feasibility for future onboard UAS deployment

The edge-inference results (Table 13) demonstrate that both selected models could be exported to ONNX, optimised with TensorRT, and executed on Jetson AGX Orin while preserving near-identical class predictions. The higher-dimensional FX10–FX17 model achieved a 1.70-fold latency speed-up with the validated mixed-precision engine, showing that hundreds of input bands did not preclude edge inference. However, pure FP16 execution produced non-finite logits for both models, and the validated mixed-precision MICA engine was slower than its FP32 counterpart. Reduced precision therefore required model-specific numerical validation and did not guarantee acceleration.

These benchmarks establish a foundation for future onboard UAS inference and deployment but do not constitute a complete onboard autonomy workflow. Field deployment would additionally require radiometric correction, georeferencing, tiling, valid data masking, mosaicking, uncertainty mapping, and mission-level data handling under realistic power, memory, and acquisition constraints. These requirements are consistent with recent work on onboard and edge AI for drone remote sensing, optimised inference on NVIDIA Jetson platforms, and low-compute hyperspectral models (Koubaa

et al., 2023; Mittal, 2019; López-Fandiño et al., 2024; Růžička and Markham, 2024).

6.4. Limitations and future transfer

The findings are constrained by benchmark comparability, external reference coverage, sensor differences, and the scope of the deployment evaluation.

Benchmark scope and model training comparisons. The benchmark compared complete model training pipelines rather than architecture alone because M5 used NPV-weighted focal loss, the CNN baselines used unweighted focal loss, and Random Forest used no class weighting. The weight-sensitivity experiment isolated weighting within one fixed architecture but did not provide weight-matched comparisons across all model families. Moreover, the CNNs were trained from scratch, and Random Forest used neither engineered spatial features nor texture. Weight-matched objectives, additional feature-based classifiers, and pretrained or foundation-model backbones would be needed to distinguish architecture, training objective, and representation-learning effects more fully (Kattenborn et al., 2021; Chowdhury et al., 2027; Braham et al., 2025; Hurtado et al., 2025).

External reference coverage and uncertainty. Cross-site evaluation used five supplied, manually reviewed and corrected tiles that were not a random or spatially comprehensive sample of SASMDD0013. The results therefore demonstrate weak NPV transfer within the evaluated sample rather than site-wide generalisation. NPV also combined dry grasses, senescent vegetation, litter, woody debris, and standing dead material, limiting diagnosis of which materials contributed to errors and spectral-importance patterns. Targeted subclasses could improve this diagnosis where sufficient reference data are available (Sotomayor et al., 2025c).

The uncertainty-stratified spectra were derived from a qualitative inference tile in the training partition, whereas the confusion-stratified spectra used held-out test tiles. Their agreement supports interpretation but does not validate uncertainty calibration. Larger prospectively selected external reference datasets, together with held-out uncertainty rasters and subclass labels, are required to evaluate domain shift, calibration, and class-specific error patterns.

Sensor harmonisation and spatial–spectral transferability. The matched 10 cm experiment controlled spatial resolution, source-tile extents, reference masks, spatial folds, and training schedule, but not spectral dimensionality, wavelength placement, radiometric response, signal-to-noise ratio, acquisition geometry, preprocessing, or co-registration. Consecutive FX10 and FX17 flights may also have introduced small illumination or shadow differences into the stacked cube. The matched experiment therefore quantifies a resolution-associated effect without isolating sensor type. Controlled band subsets, spectral-response matching, radiometric harmonisation, resampling series, and cross-platform validation are needed to separate these factors (Schiefer et al., 2023). Systematic spatial resampling and targeted band-selection experiments, together with sensors covering longer-wavelength SWIR features, could identify the coarsest spatial resolution and smallest spectral subset that maintain reliable BE–NPV–PV discrimination, supporting more practical and cost-effective FVC monitoring.

The primary FX10–FX17 input also retained 15 interpolated water-absorption channels. Their exclusion did not improve NPV F1, but this does not establish that interpolation recovered reliable reflectance. Future work should compare exclusion, masking, and models that accommodate unreliable channels without assuming spectral continuity.

Transfer and operational scaling. Future transfer should prioritise prospectively selected multi-site and multi-season semi-arid datasets spanning vegetation condition, soil background, illumination, and phenology. Such datasets are needed to assess temporal transferability, particularly whether models trained on data from one season generalise to other seasons with different phenological and surface conditions. Following validation across these gradients, the workflow could be tested in ecosystems often characterised by low-stature or spatially heterogeneous vegetation, including Antarctic moss and lichen communities, alpine tundra, dry coastal heathlands, post-fire landscapes, and other arid shrublands. These are prospective applications rather than demonstrated transfer settings.

Transfer across sensors and platforms may require spectral-response matching, radiometric cross-calibration, spatial resampling, and accurate co-registration. The Jetson AGX Orin benchmarks demonstrate edge-inference feasibility and provide a basis for integrating edge computing with UAS data acquisition to support near-real-time vegetation mapping. However, a complete operational workflow would need to incorporate radiometric correction, georeferencing,

tiling, valid data masking, inference, uncertainty estimation, and geospatial mosaicking. Depending on the system configuration, these processing stages could be performed onboard or downstream. Integration with fixed-wing or multirotor UAS platforms and subsequent flight validation would be needed to assess end-to-end performance under realistic payload, power, memory, storage, and processing-time constraints.

7. Conclusions

This study developed and evaluated an NPV-aware CNN workflow with spectral-channel adaptation for UAS-based fractional vegetation cover mapping in semi-arid vegetation. Controlled M1–M5 ablations identified NPV-weighted optimisation as the main contributor to target-class improvement, while spectral-channel adaptation and lightweight cross-channel attention acted as supporting components. M5 achieved the highest aggregate NPV F1 of 0.496, +0.148 relative to M1, whereas M3 achieved the highest aggregate mean F1 (0.745) and mIoU (0.629).

The combined 296-band FX10–FX17 benchmark compared M5 with five baseline configurations: per-pixel Random Forest, plain U-Net M1, PCA-3 and PCA-10 versions of the same plain U-Net, and SS3FCN. M5 achieved the highest mean F1 (0.705), NPV F1 (0.461), and mIoU (0.573), while Random Forest and SS3FCN remained competitive in aggregate performance, with mean F1/mIoU of 0.688/0.556 and 0.685/0.565, respectively. PCA compression underperformed the plain U-Net using the combined 296-band input despite retaining more than 99% of spectral variance. Because M5 used NPV-weighted focal loss, the CNN baselines used unweighted focal loss, and Random Forest used no class weighting, these findings support the complete model training pipeline rather than architectural superiority alone. Spatial resolution and patch scale also affected performance: resampling MICA to 10 cm reduced segmentation accuracy, but matched-resolution MICA retained an mIoU advantage of 0.094 over FX10–FX17, while smaller patches preserved finer local structure than larger, more spatially regularised outputs.

Post-inference reflectance, uncertainty and confusion, spectral-index, and model-derived importance analyses confirmed that NPV remained the least stable and most spectrally ambiguous class. Gate, gradient, and permutation outputs provided complementary evidence for VIS and NIR–SWIR contributions, but should be interpreted as diagnostic model summaries rather than direct retrievals of vegetation traits. Zero-shot evaluation likewise showed

stronger transfer for BE and PV than for NPV; the highest external-site NPV F1 across all pipelines was only 0.120.

ONNX and TensorRT results established edge-inference feasibility for both selected sensor models. The validated mixed-precision FX10–FX17 engine achieved a 1.70-fold latency speed-up with 99.96% argmax agreement, although pure FP16 was numerically unstable and reduced precision did not accelerate MICA. These benchmarks establish a foundation for future onboard UAS inference and deployment. Overall, the workflow provides an interpretable, sensor-informed baseline for NPV-aware FVC mapping. The principal priorities are broader multi-site and multi-season validation, sensor harmonisation, and uncertainty calibration.

8. Acknowledgements

We would like to acknowledge the Terrestrial Ecosystem Research Network (TERN) for support, in particular the TERN Ecosystem Surveillance team and TERN Landscapes program. We would like to thank Ben Sparrow, Poornima Sivanandam and Juan Carlos Montes-Herrera for drone operation and data processing. We thank the managers of Calperum Station (Australian Landscape Trust), South Australia, for providing access to the study sites. Laura Sotomayor is supported by a Research Training Program (RTP) scholarship through the University of Tasmania. The Australian Research Council (ARC) supported some of the initial fieldwork and infrastructure under Discovery grant DP180103460. We gratefully acknowledge Prof. Megan Lewis for her valuable guidance in helping us understand semi-arid ecosystems through an integrated ecological and remote sensing perspective, and for her helpful comments on the final manuscript. We also thank all individuals who contributed to the labelling process: Prof. Megan Lewis (School of Biological Sciences, University of Adelaide), Dr Krishna Lamsal (School of Geography, Planning, and Spatial Sciences, UTAS), Dr. Agustina Barros (Researcher at National Scientific and Technical Research Council), Dr. Sebastian Rossi (Researcher at National Scientific and Technical Research Council), Molly Marshall (School of Geography, Planning, and Spatial Sciences, UTAS) and Sophia Hoyer (School of Geography, Planning, and Spatial Sciences, UTAS). The authors gratefully acknowledge NVIDIA for selecting the project *Mapping Ecosystem Resilience with High-Resolution Remote Sensing Data* for inclusion in the NVIDIA Academic Grant Program. This six-month award provided cloud access through Brev to one reserved in-

stance of 8× NVIDIA A100 80 GB GPUs from October 1, 2025 to March 31, 2026, comprising 80 GiB VRAM per GPU, 2 TiB RAM, 128 CPUs, 60 TiB of storage, and 560 GiB NVMe storage. Multiple team members were permitted to use the resource, although only one instance was allocated to the project. The authors also gratefully acknowledge NVIDIA AI Technology for the research collaboration and additional computational support provided during model development and testing. These resources included a Brev/SFCompute NVIDIA H100 environment with 8× NVIDIA H100 GPUs, 74 GiB available GPU memory per GPU, 112 CPUs, 894 GiB RAM, and 1.36 TiB storage, together with an NVIDIA Jetson AGX Orin 32 GB device with 12 CPU cores, 30 GB available RAM, and 298 GB storage for edge-compute testing.

Appendix A. Additional within-site performance diagnostics

This appendix reports additional within-site performance diagnostics that complement the main results. These include NPV intersection-over-union (IoU), macro-averaged mean F1-score, the NPV F1–mIoU trade-off, and class-wise F1-score and IoU for bare ground (BE), non-photosynthetic vegetation (NPV), and photosynthetic vegetation (PV). These diagnostics support interpretation of the aggregate performance summary by showing whether improvements in NPV F1, mean F1, and mIoU were associated with class-specific gains or trade-offs across sensor profiles, patch scales, and model variants.

Appendix A.1. Sensitivity to NPV class weighting

The sensitivity analysis confirmed that NPV weighting was the principal contributor to improved target-class performance, as shown by the validation results below. Increasing the NPV weight from 1 to 2 increased validation NPV F1 from 0.391 to 0.466, macro F1 from 0.725 to 0.745, and mIoU from 0.618 to 0.631. Increasing the NPV weight further to 3 raised NPV recall from 0.488 to 0.642 but reduced precision from 0.459 to 0.366 and did not provide an additional improvement in NPV F1, macro F1, or mIoU. The $[1, 2, 1]$ configuration was therefore selected because it provided the strongest validation balance across target-class and aggregate metrics.

Table Appendix A.1: Validation sensitivity to the NPV focal-loss class weight for the fixed spectral-adapter and cross-channel-attention architecture. Values are means ± sample standard deviations across three spatial folds. Class weights are reported in the order BE, NPV, and PV.

Class weights	NPV precision	NPV recall	NPV F1	Macro F1	mIoU
$[1, 1, 1]$	0.578 ± 0.135	0.304 ± 0.040	0.391 ± 0.018	0.725 ± 0.008	0.618 ± 0.017
$[1, 2, 1]$	0.459 ± 0.124	0.488 ± 0.019	$\mathbf{0.466 \pm 0.055}$	$\mathbf{0.745 \pm 0.030}$	$\mathbf{0.631 \pm 0.035}$
$[1, 3, 1]$	0.366 ± 0.081	$\mathbf{0.642 \pm 0.064}$	0.463 ± 0.075	0.739 ± 0.030	0.622 ± 0.031

Table Appendix A.2: Held-out test sensitivity to the NPV focal-loss class weight for the fixed spectral-adapter and cross-channel-attention architecture. Values are means ± sample standard deviations across three spatial folds. The class weight was selected from validation performance; these held-out test results were not used for weight selection.

Class weights	NPV precision	NPV recall	NPV F1	Macro F1	mIoU
$[1, 1, 1]$	0.635 ± 0.145	0.252 ± 0.174	0.331 ± 0.149	0.671 ± 0.091	0.555 ± 0.102
$[1, 2, 1]$	0.547 ± 0.143	0.409 ± 0.197	0.442 ± 0.104	0.711 ± 0.066	$\mathbf{0.587 \pm 0.081}$
$[1, 3, 1]$	0.424 ± 0.123	$\mathbf{0.552 \pm 0.130}$	$\mathbf{0.468 \pm 0.077}$	$\mathbf{0.714 \pm 0.046}$	0.585 ± 0.057

On the held-out test data, $[1, 3, 1]$ achieved a slightly higher mean NPV F1 than $[1, 2, 1]$ (0.468 versus 0.442), whereas $[1, 2, 1]$ achieved a marginally higher mIoU (0.587 versus 0.585).

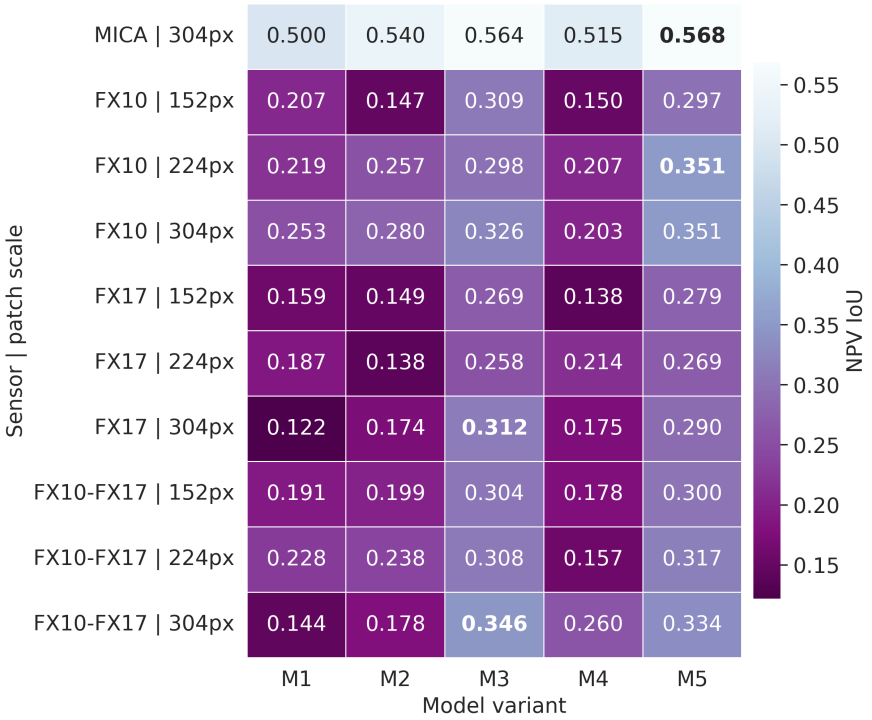


Figure Appendix A.1: Additional within-site target-class performance across model variants, sensor profiles, and patch scales. Values show NPV intersection-over-union (IoU) for each sensor-profile and patch-scale configuration. Rows denote sensor-profile and patch-scale combinations, and columns denote model variants M1–M5. Bold values indicate the best-performing variant within each sensor row. The heatmap complements the NPV F1-score results reported in the main text by showing the corresponding overlap-based target-class performance.

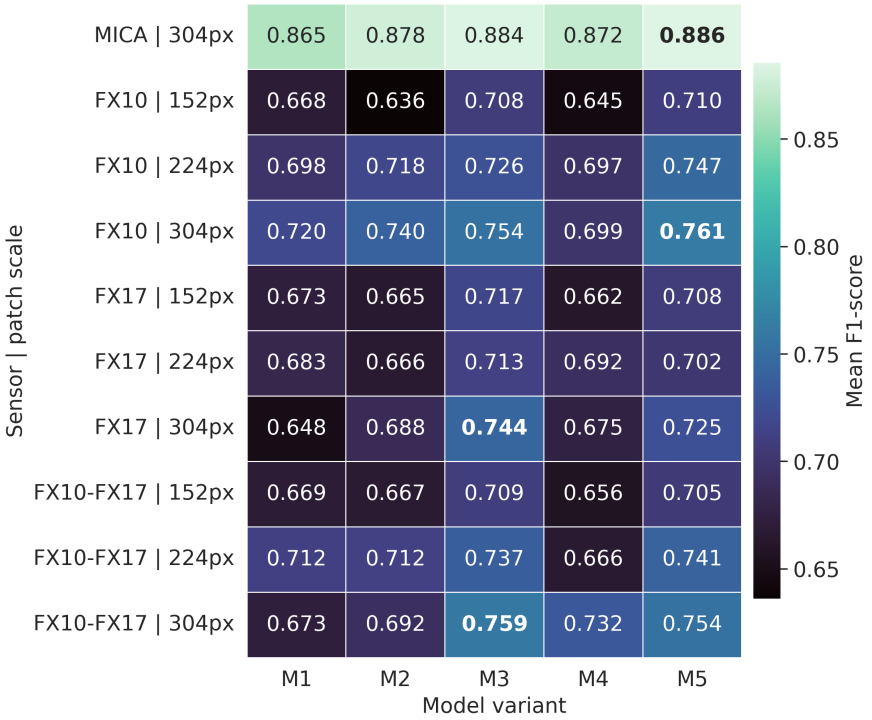


Figure Appendix A.2: Additional within-site aggregate segmentation performance across model variants, sensor profiles, and patch scales. Values show macro-averaged mean F1-score across bare ground (BE), non-photosynthetic vegetation (NPV), and photosynthetic vegetation (PV). Rows denote sensor-profile and patch-scale combinations, and columns denote model variants M1–M5. Bold values indicate the best-performing variant within each sensor row. The heatmap complements the mIoU results reported in the main text by showing the corresponding F1-based aggregate segmentation performance.

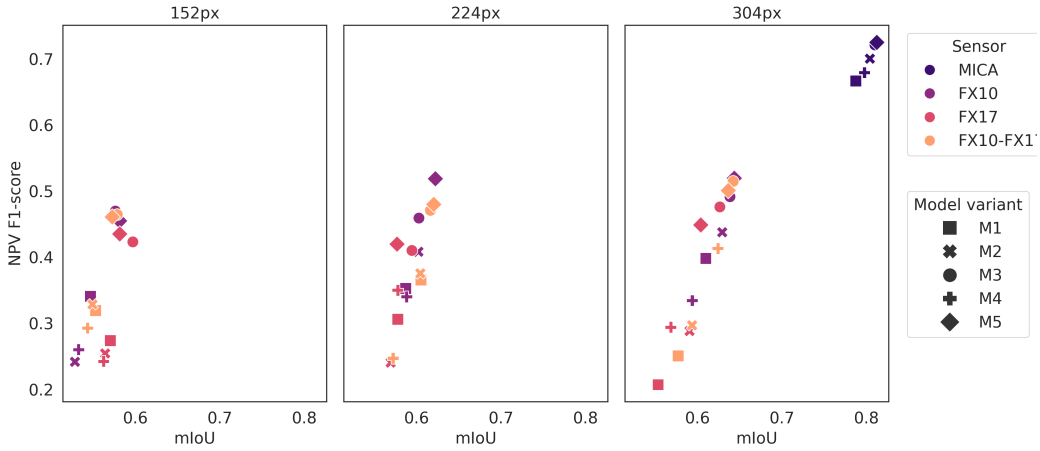


Figure Appendix A.3: Within-site trade-off between target-class NPV F1-score and aggregate mIoU across patch scales. Each panel corresponds to a patch scale, with points representing individual sensor-profile and model-variant combinations. The x-axis shows mIoU computed across BE, NPV, and PV, while the y-axis shows NPV F1-score. Colours denote sensor profiles and marker shapes denote model variants M1–M5. Points in the upper-right region indicate configurations that jointly improve NPV detection and overall segmentation quality. The plot complements the heatmap summaries by showing that the NPV-weighted variants generally shift configurations toward higher NPV F1-score while maintaining comparable or improved mIoU.

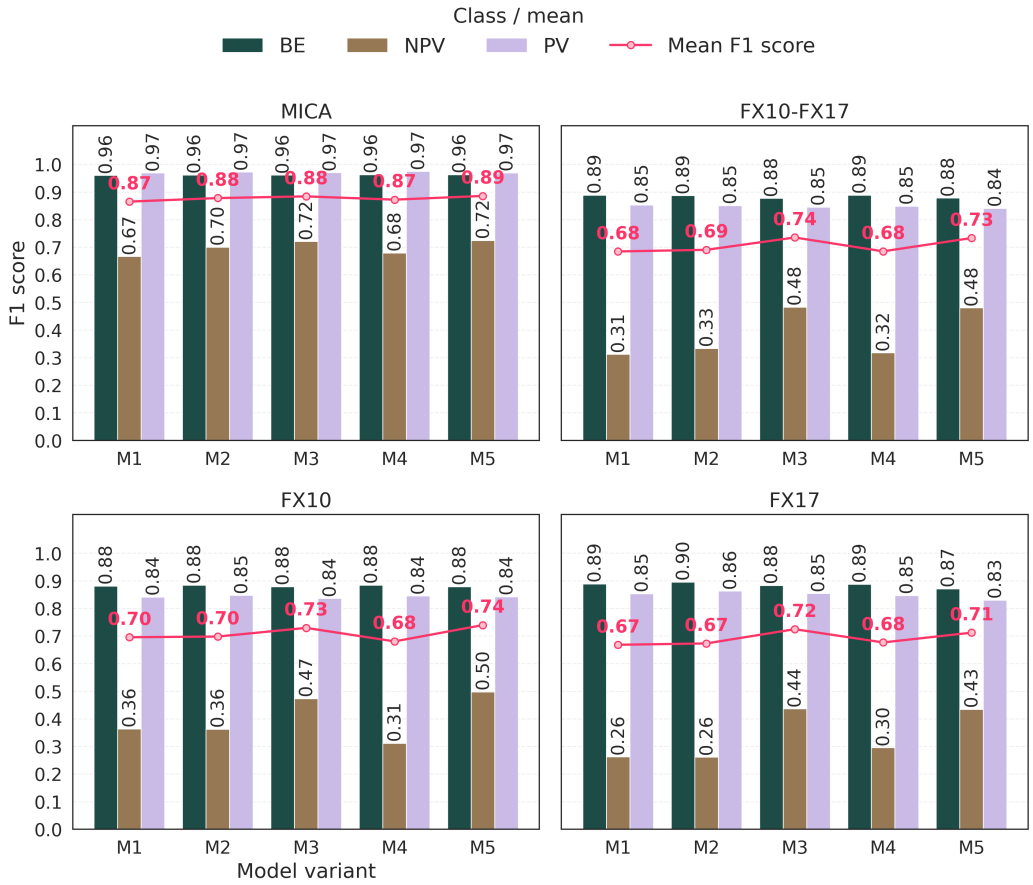


Figure Appendix A.4: Class-wise within-site F1-score across sensor profiles and model variants. Panels show the MICA, FX10–FX17, FX10, and FX17 sensor profiles, with model variants M1–M5 shown on the x-axis. Bars indicate class-wise F1-score for bare ground (BE), non-photosynthetic vegetation (NPV), and photosynthetic vegetation (PV), using a consistent class palette across panels. The line indicates the macro-averaged mean F1-score across the three FVC classes for each model variant. M1 is the baseline U-Net, M2 is the spectral-adapter CNN, M3 is the NPV-weighted spectral-adapter CNN, M4 is the spectral-adapter CNN with lightweight cross-channel attention, and M5 is the NPV-weighted spectral-adapter CNN with lightweight cross-channel attention. The figure highlights that BE and PV achieved consistently high F1-scores across sensor profiles, whereas NPV remained the limiting class. The NPV-weighted variants, particularly M3 and M5, improved NPV F1-score most clearly for the hyperspectral sensor profiles while maintaining high BE and PV performance.

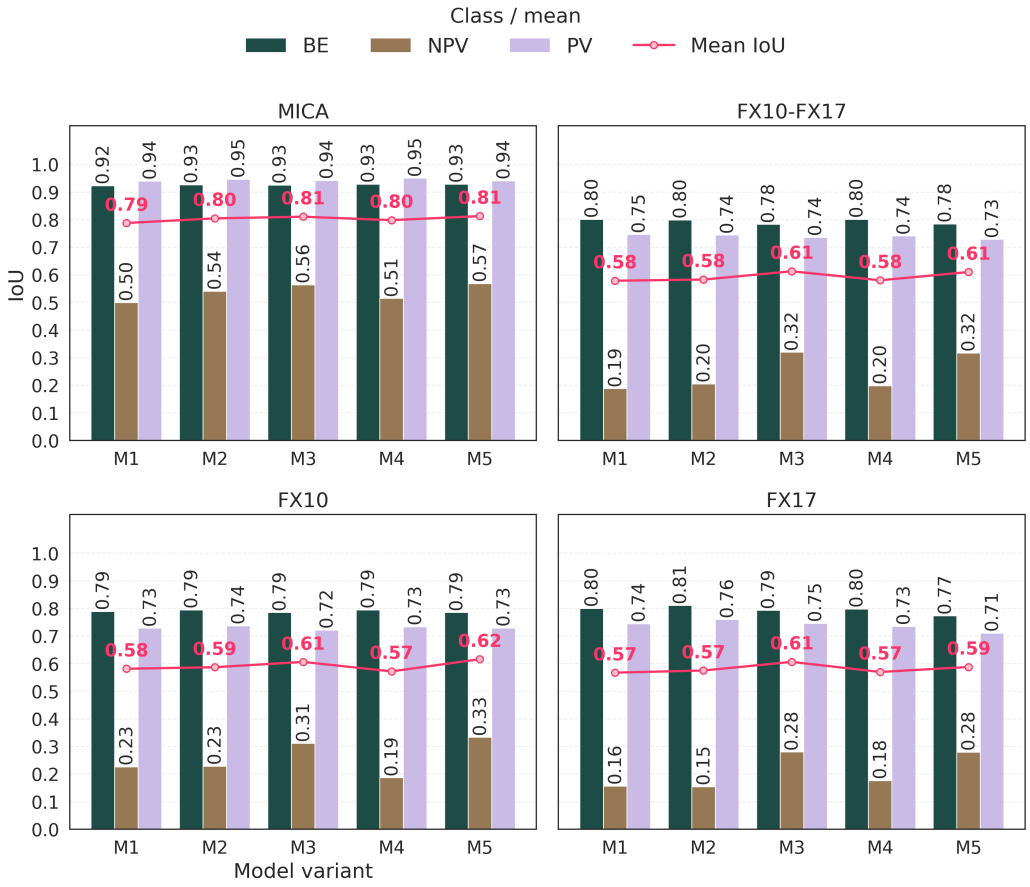


Figure Appendix A.5: Class-wise within-site intersection-over-union (IoU) across sensor profiles and model variants. Panels show the MICA, FX10–FX17, FX10, and FX17 sensor profiles, with model variants M1–M5 shown on the x-axis. Bars indicate class-wise IoU for bare ground (BE), non-photosynthetic vegetation (NPV), and photosynthetic vegetation (PV), using the same class palette as the class-wise F1-score figure. The line indicates the macro-averaged mean IoU across the three FVC classes for each model variant. M1 is the baseline U-Net, M2 is the spectral-adapter CNN, M3 is the NPV-weighted spectral-adapter CNN, M4 is the spectral-adapter CNN with lightweight cross-channel attention, and M5 is the NPV-weighted spectral-adapter CNN with lightweight cross-channel attention. The IoU results show the same class-level pattern as the F1-score results, with high BE and PV overlap and substantially lower NPV overlap. Improvements in mean IoU were therefore mainly controlled by gains in NPV, especially for the NPV-weighted variants M3 and M5.

Appendix A.2. Uncertainty- and confusion-stratified spectra

The following figure presents the uncertainty- and confusion-stratified mean reflectance spectra summarised in Section 5.2.2.

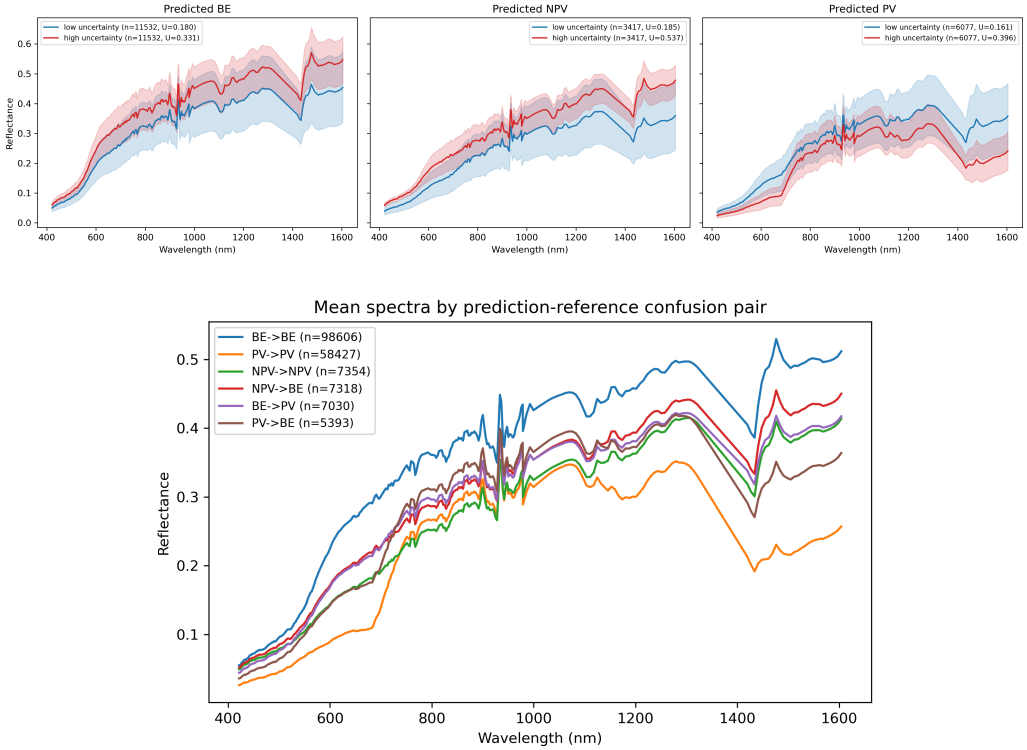


Figure Appendix A.1: Spectral tracing of high-uncertainty and confused NPV pixels for the combined 296-band FX10–FX17 M5 configuration. **Top:** mean reflectance spectra with one standard deviation envelopes for the low- and high-uncertainty strata of each predicted class in the stitched inference tile, with strata defined by the class-wise 25th and 75th percentiles of the Monte Carlo dropout uncertainty; legend entries report the stratum pixel count (n) and mean uncertainty (U). **Bottom:** mean reflectance spectra for prediction–reference confusion pairs on the spatially held-out block-1 test tiles, with pairs denoted as predicted class followed by reference class.

Appendix A.3. Spectral gate and permutation importance

The following figure compares the learned input spectral gate with the model-agnostic region-level permutation importance described in Section 4.3.4.

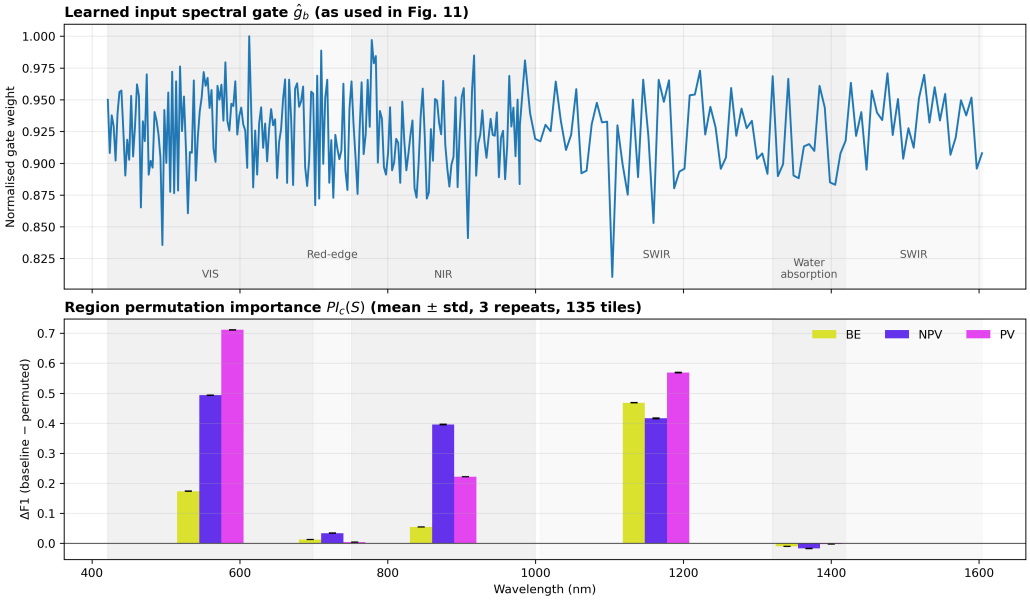


Figure Appendix A.2: Verification of model-derived spectral importance for the combined 296-band FX10–FX17 M5 configuration. **Top:** normalised learned input spectral gate $\hat{g}_b$ of the spectral adapter across the 296 retained bands, with shaded spectral regions. **Bottom:** region-level permutation importance $PI_c(S)$, calculated as the drop in class-wise F1-score when all bands within a region are jointly permuted across valid pixels (mean ± standard deviation over three repeats across all 135 patches). Permuting the interpolated water-absorption interval (1321–1420 nm) produced no degradation.

Appendix B. Supplementary deployment diagnostics

This appendix provides additional diagnostic information supporting the TensorRT deployment results reported in Section 5.3. The supplementary material includes ONNX export metadata, full parity diagnostics, latency-throughput behaviour, and representative tile-level parity maps relative to the PyTorch reference.

Appendix B.1. ONNX export metadata

The selected FX10–FX17 s152 and MICA s304 segmentation models were exported to ONNX before TensorRT engine construction. Table Appendix B.1 summarises the exported model interfaces. Both exports used dynamic batch and spatial dimensions and produced three-channel logits corresponding to BE, NPV, and PV.

Table Appendix B.1: Supplementary ONNX export metadata for the selected deployment models.

Sensor	Input tensor	Output tensor	Nodes	Weights (MB)
FX10–FX17 s152	FLOAT[batch, 296, height, width]	FLOAT[batch, 3, height, width]	218	125.47
MICA s304	FLOAT[batch, 10, height, width]	FLOAT[batch, 3, height, width]	213	126.53

Appendix B.2. Full parity diagnostics

Table Appendix B.2 reports logit-level and argmax-level parity relative to the PyTorch reference. ONNX Runtime reproduced the PyTorch outputs exactly within the reported precision for both sensors. TensorRT FP32 preserved near-identical predictions, while the validated FP16-labelled engines showed larger logit differences but maintained high argmax agreement. Pure FP16 TensorRT engines are not tabulated because they produced non-finite logits and were excluded from deployment interpretation.

Table Appendix B.2: Supplementary parity diagnostics relative to the PyTorch reference. Agreement and mIoU were computed from argmax predictions relative to PyTorch. FP16-labelled rows correspond to validated mixed FP16/FP32 TensorRT engines rather than pure FP16 engines.

Sensor	Backend	$\max \lvert\Delta\rvert$	$\overline{\lvert\Delta\rvert}$	Agree (%)	mIoU
FX10–FX17 s152	ONNX Runtime	0.00	0.00	100.0000	1.0000
FX10–FX17 s152	TRT FP32	5.62×10^{-5}	5.04×10^{-6}	100.0000	1.0000
FX10–FX17 s152	TRT FP16	1.80×10^{-2}	1.50×10^{-3}	99.9636	0.9991
MICA s304	ONNX Runtime	0.00	0.00	100.0000	1.0000
MICA s304	TRT FP32	1.73×10^{-3}	6.05×10^{-5}	99.9987	1.0000
MICA s304	TRT FP16	1.23×10^{-2}	4.20×10^{-4}	99.9933	0.9998

Appendix B.3. TensorRT latency-throughput diagnostic

The main text reports the deployment-ready TensorRT configurations in Table 13 and summarises the speed–parity trade-off in Figure 12. Figure Appendix B.3 provides the corresponding latency-throughput diagnostic.

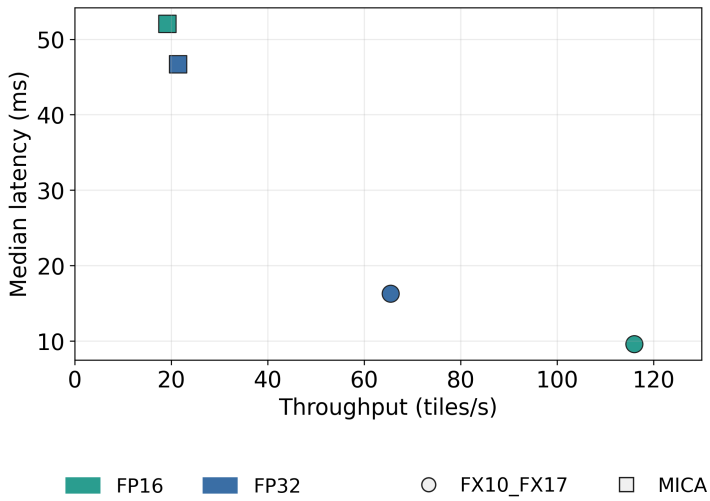
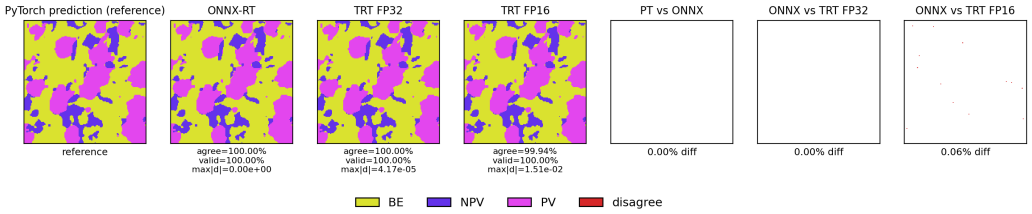


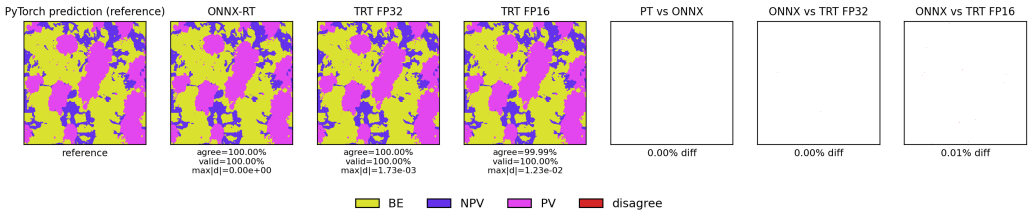
Figure Appendix B.3: Supplementary TensorRT latency-throughput diagnostic on Jetson AGX Orin. The x-axis shows throughput in tiles s^{-1}, and the y-axis shows median per-tile latency in milliseconds. Points farther to the lower-right indicate higher-throughput and lower-latency deployment configurations. FP16-labelled points correspond to validated mixed FP16/FP32 TensorRT engines obtained after Polygraphy precision debugging.

Appendix B.4. TensorRT parity maps

Representative tile-level parity maps are shown for the deployment-ready TensorRT FP32 engines and the validated FP16-labelled mixed FP16/FP32 engines. Pure FP16 TensorRT engines and intermediate precision-debugging configurations are omitted because they were not deployment-ready.



(a) FX10–FX17 s152



(b) MICA s304

Figure Appendix B.4: Supplementary TensorRT parity maps for representative FX10–FX17 s152 and MICA s304 inference tiles. PyTorch predictions are used as the reference and compared with deployment-ready TensorRT FP32 and FP16-labelled mixed FP16/FP32 outputs. Class-map panels show BE, NPV, and PV predictions, while disagreement panels highlight pixel-wise differences relative to the PyTorch reference. White indicates agreement and red indicates disagreement.

Code and Data Availability

The full FVC mapping workflow developed in this study, *hyperFVC*, is available at `https://github.com/LNSOTOM/fvc_function`. The repository contains the code structure for multi-sensor UAS FVC segmentation, spectral-encoding model variants, post-inference spectral characterisation, and edge-deployment benchmarking. The version used in this manuscript is 2026.28.4. Code required to reproduce the final experiments and results will be made publicly available after acceptance of the manuscript.

The UAS imagery, tiled datasets, and manual FVC reference labels used in this study are available from Zenodo at `https://zenodo.org/records/15036860`.

Declaration of generative AI and AI-assisted technologies in the manuscript preparation process.

During the preparation of this work the author(s) used ChatGPT for language editing. During analysis, the authors employed GitHub Copilot for

programming assistance. After using these tools, the author(s) reviewed and edited the content and code as needed and take(s) full responsibility for the content of the published article and code.

References

Asner, G.P., Lobell, D.B., 2000. A Biogeophysical Approach for Automated SWIR Unmixing of Soils and Vegetation. Remote Sensing of Environment 74, 99–112. URL: https://www.sciencedirect.com/science/article/pii/S0034425700001267, doi:10.1016/S0034-4257(00)00126-7.

Asner, G.P., Martin, R.E., 2009. Airborne spectranomics: mapping canopy chemical and taxonomic diversity in tropical forests. Frontiers in Ecology and the Environment 7, 269–276. URL: https://onlinelibrary.wiley.com/doi/abs/10.1890/070152, doi:10.1890/070152. _eprint: https://esajournals.onlinelibrary.wiley.com/doi/pdf/10.1890/070152.

Bian, J., Li, A., Zhang, Z., Zhao, W., Lei, G., Xia, H., Tan, J., 2016. Grassland fractional vegetation cover monitoring using the composited HJ-1A/B time series images and unmanned aerial vehicles: A case study in Zoige wetland, China, in: 2016 IEEE International Geoscience and Remote Sensing Symposium (IGARSS), pp. 7192–7195. URL: https://ieeexplore.ieee.org/document/7730876, doi:10.1109/IGARSS.2016.7730876.

Bollard, B., Doshi, A., Gilbert, N., Poirot, C., Gillman, L., 2022. Drone Technology for Monitoring Protected Areas in Remote and Fragile Environments. Drones 6, 42. URL: https://www.mdpi.com/2504-446X/6/2/42, doi:10.3390/drones6020042.

Braham, N.A.A., Albrecht, C.M., Mairal, J., Chanussot, J., Wang, Y., Zhu, X.X., 2025. SpectralEarth: Training Hyperspectral Foundation Models at Scale. IEEE Journal of Selected Topics in Applied Earth Observations and Remote Sensing 18, 16780–16797. URL: https://ieeexplore.ieee.org/document/11045062, doi:10.1109/JSTARS.2025.3581451.

Breiman, L., 2001. Random Forests. Machine Learning 45, 5–32. doi:10.1023/A:1010933404324.

Brodribb, T., Brodersen, C.R., Carriqui, M., Tonet, V., Rodriguez Dominguez, C., McAdam, S., 2021. Linking xylem network failure with leaf tissue death. New Phytologist 232, 68–79. URL: https://

onlinelibrary.wiley.com/doi/abs/10.1111/nph.17577, doi:10.1111/nph.17577. tex.copyright: © 2021 The Authors. New Phytologist © 2021 New Phytologist Foundation.

Brodribb, T.J., Powers, J., Cochard, H., Choat, B., 2020. Hanging by a thread? Forests and drought. Science 368, 261–266. URL: https://www.science.org/doi/full/10.1126/science.aat7631, doi:10.1126/science.aat7631.

Brodrick, P.G., Davies, A.B., Asner, G.P., 2019. Uncovering Ecological Patterns with Convolutional Neural Networks. Trends in Ecology & Evolution 34, 734–745. URL: https://www.sciencedirect.com/science/article/pii/S0169534719300862, doi:10.1016/j.tree.2019.03.006.

Chabrillat, S., Foerster, S., Segl, K., Beamish, A., Brell, M., Asadzadeh, S., Milewski, R., Ward, K.J., Brosinsky, A., Koch, K., Scheffler, D., Guillaso, S., Kokhanovsky, A., Roessner, S., Guanter, L., Kaufmann, H., Pinnel, N., Carmona, E., Storch, T., Hank, T., Berger, K., Wocher, M., Hostert, P., van der Linden, S., Okujeni, A., Janz, A., Jakimow, B., Bracher, A., Soppa, M.A., Alvarado, L.M.A., Buddenbaum, H., Heim, B., Heiden, U., Moreno, J., Ong, C., Bohn, N., Green, R.O., Bachmann, M., Kokaly, R., Schodlok, M., Painter, T.H., Gascon, F., Buongiorno, F., Mottus, M., Brando, V.E., Feilhauer, H., Betz, M., Baur, S., Feckl, R., Schickling, A., Krieger, V., Bock, M., La Porta, L., Fischer, S., 2024. The EnMAP spaceborne imaging spectroscopy mission: Initial scientific results two years after launch. Remote Sensing of Environment 315, 114379. URL: https://www.sciencedirect.com/science/article/pii/S003442572400405X, doi:10.1016/j.rse.2024.114379.

Chen, J., Yi, S., Qin, Y., Wang, X., 2016. Improving estimates of fractional vegetation cover based on UAV in alpine grassland on the Qinghai–Tibetan Plateau. International Journal of Remote Sensing 37, 1922–1936. URL: https://doi.org/10.1080/01431161.2016.1165884, doi:10.1080/01431161.2016.1165884.

Cherif, E., Feilhauer, H., Berger, K., Dao, P.D., Ewald, M., Hank, T.B., He, Y., Kovach, K.R., Lu, B., Townsend, P.A., Kattenborn, T., 2023. From spectra to plant functional traits: Transferable multi-trait models from heterogeneous and sparse data. Remote Sensing of Environ-

ment 292, 113580. URL: https://www.sciencedirect.com/science/article/pii/S0034425723001311, doi:10.1016/j.rse.2023.113580.

Choi, S.K., Lee, S.K., Jung, S.H., Choi, J.W., Choi, D.Y., Chun, S.J., 2016. Estimation of Fractional Vegetation Cover in Sand Dunes Using Multi-spectral Images from Fixed-wing UAV. Journal of the Korean Society of Surveying, Geodesy, Photogrammetry and Cartography 34, 431–441. URL: https://koreascience.or.kr/article/JAKO201625752509115.page, doi:10.7848/ksgpc.2016.34.4.431.

Chowdhury, A.I., Beloiu, M., Kattenborn, T., Mosig, C., Ahishali, M., Vastaranta, M., Puttonen, E., Honkavaara, E., Huo, L., Uddin, M.J., Griess, V.C., Kuzmin, A., Cheng, Y., Junttila, S., 2027. Remote sensing and deep learning for standing dead-tree detection and mapping: A review of advances, challenges, and future directions. ISPRS Journal of Photogrammetry and Remote Sensing 243, 1–22. URL: https://doi.org/10.1016/j.isprsjprs.2026.09.050, doi:10.1016/j.isprsjprs.2026.09.050.

Cimoli, E., Lucieer, A., Malenovský, Z., Woodgate, W., Janoutová, R., Turner, D., Haynes, R.S., Phinn, S., 2024. Mapping functional diversity of canopy physiological traits using UAS imaging spectroscopy. Remote Sensing of Environment 302, 113958. URL: https://www.sciencedirect.com/science/article/pii/S0034425723005102, doi:10.1016/j.rse.2023.113958.

Cimoli, E., Lucieer, V., Meiners, K.M., Chennu, A., Castrisios, K., Ryan, K.G., Lund-Hansen, L.C., Martin, A., Kennedy, F., Lucieer, A., 2020. Mapping the in situ microspatial distribution of ice algal biomass through hyperspectral imaging of sea-ice cores. Scientific Reports 10, 21848. URL: https://www.nature.com/articles/s41598-020-79084-6, doi:10.1038/s41598-020-79084-6. tex.copyright: 2020 The Author(s).

Cimoli, E., Montes-Herrera, J.C., Cummings, V., Marriott, P., Haynes, R.S., 2026. Advancing Monitoring of Nearshore Antarctic Sea Ice and Benthic Ecosystems with HIcyBot. Oceanography 39, 6–13. URL: https://tos.org/oceanography/article/advancing-monitoring-of-nearshore-antarctic-sea-ice-and-benthic-ecosystems-with doi:10.5670/oceanog.2026.e107.

Cotrozzi, L., 2022. Spectroscopic detection of forest diseases: a review (1970–2020). Journal of Forestry Research 33, 21–38. URL: https://doi.org/10.1007/s11676-021-01378-w, doi:10.1007/s11676-021-01378-w.

Curran, P.J., 1989. Remote sensing of foliar chemistry. Remote Sensing of Environment 30, 271–278. doi:10.1016/0034-4257(89)90069-2.

DCCEEW, 2017. Australian Vegetation Attribute Manual Version 7.0 - DCCEEW. URL: https://www.dcceew.gov.au/environment/land/publications/australian-vegetation-attribute-manual-version-7.

Dou, H., Lin, T., Xu, Q., Wang, J., Xu, H., Aili, A., Zhang, P., Wang, C., Zhao, W., 2025. Ecohydrological significance of microtopography in arid Zones: Regulating Water, supporting Vegetation, promoting ecosystem stability. Ecological Indicators 171, 113200. URL: https://www.sciencedirect.com/science/article/pii/S1470160X25001293, doi:10.1016/j.ecolind.2025.113200.

Fisk, C., Clarke, K.D., Delean, S., Lewis, M.M., 2019a. Distinguishing Photosynthetic and Non-Photosynthetic Vegetation: How Do Traditional Observations and Spectral Classification Compare? Remote Sensing 11, 2589. URL: https://www.mdpi.com/2072-4292/11/21/2589, doi:10.3390/rs11212589.

Fisk, C., Clarke, K.D., Lewis, M.M., 2019b. Comparison of Hyperspectral Versus Traditional Field Measurements of Fractional Ground Cover in the Australian Arid Zone. Remote Sensing 11, 2825. URL: https://www.mdpi.com/2072-4292/11/23/2825, doi:10.3390/rs11232825. number: 23.

Gal, Y., Ghahramani, Z., 2016. Dropout as a Bayesian Approximation: Representing Model Uncertainty in Deep Learning. URL: http://arxiv.org/abs/1506.02142, doi:10.48550/arXiv.1506.02142.

Guanter, L., Kaufmann, H., Segl, K., Foerster, S., Rogass, C., Chabrillat, S., Kuester, T., Hollstein, A., Rossner, G., Chlebek, C., Straif, C., Fischer, S., Schrader, S., Storch, T., Heiden, U., Mueller, A., Bachmann, M., Mühle, H., Müller, R., Habermeyer, M., Ohndorf, A., Hill, J., Buddenbaum, H., Hostert, P., Van der Linden, S., Leitão, P.J., Rabe, A.,

Doerffer, R., Krasemann, H., Xi, H., Mauser, W., Hank, T., Locherer, M., Rast, M., Staenz, K., Sang, B., 2015. The EnMAP Spaceborne Imaging Spectroscopy Mission for Earth Observation. Remote Sensing 7, 8830–8857. URL: https://www.mdpi.com/2072-4292/7/7/8830, doi:10.3390/rs70708830.

Harrison, B.A., Gibson, R., Bastin, G., Thackway, R., Huete, A., Donald, G., Lyons, M., Sparks, T., Byrne, G., Lewis, M.M., Xie, Q., 2021. Earth Observation: Data, Processing and Applications. Volume 3A: Applications—Terrestrial Vegetation. Australia and New Zealand CRC for Spatial Information. URL: https://opus.lib.uts.edu.au/handle/10453/155085. tex.copyright: info:eu-repo/semantics/openAccess.

Haut, J.M., Bernabé, S., Paoletti, M.E., Fernandez-Beltran, R., Plaza, A., Plaza, J., 2019. Low–High-Power Consumption Architectures for Deep-Learning Models Applied to Hyperspectral Image Classification. IEEE Geoscience and Remote Sensing Letters 16, 776–780. URL: https://ieeexplore.ieee.org/abstract/document/8554064, doi:10.1109/LGRS.2018.2881045.

Haynes, R.S., Lucieer, A., Brodribb, T.J., Tonet, V., Cimoli, E., 2024. Predicting key water stress indicators of Eucalyptus viminalis and Callitris rhomboidea using high-resolution visible to short-wave infrared spectroscopy. Plant, Cell & Environment 47, 4992–5006. URL: https://onlinelibrary.wiley.com/doi/abs/10.1111/pce.15083, doi:10.1111/pce.15083. tex.copyright: © 2024 The Author(s). Plant, Cell & Environment published by John Wiley & Sons Ltd.

Haynes, R.S., Lucieer, A., Turner, D., Cimoli, E., 2025. Co-Registration of Multi-Modal UAS Pushbroom Imaging Spectroscopy and RGB Imagery Using Optical Flow. Drones 9, 132. URL: https://www.mdpi.com/2504-446X/9/2/132, doi:10.3390/drones9020132.

Haynes, R.S., Lucieer, A., Turner, D., Cimoli, E., Sivanandam, P., Brodribb, T.J., 2026. UAS ecophysiology: Imaging spectroscopy can map canopy leaf water potential in a diverse forest ecosystem. Remote Sensing of Environment 344, 115532. URL: https://www.sciencedirect.com/science/article/pii/S0034425726003020, doi:10.1016/j.rse.2026.115532.

He, X., Chen, Y., Lin, Z., 2021. Spatial-Spectral Transformer for Hyperspectral Image Classification. Remote Sensing 13, 498. URL: https://www.mdpi.com/2072-4292/13/3/498, doi:10.3390/rs13030498.

Hendrycks, D., Gimpel, K., 2023. Gaussian Error Linear Units (GELUs). URL: http://arxiv.org/abs/1606.08415, doi:10.48550/arXiv.1606.08415. arXiv:1606.08415 [cs.LG].

Homolová, L., Malenovský, Z., Clevers, J.G.P.W., García-Santos, G., Schaepman, M.E., 2013. Review of optical-based remote sensing for plant trait mapping. Ecological Complexity 15, 1–16. URL: https://www.sciencedirect.com/science/article/pii/S1476945X13000524, doi:10.1016/j.ecocom.2013.06.003.

Hong, D., Han, Z., Yao, J., Gao, L., Zhang, B., Plaza, A., Chanussot, J., 2022. SpectralFormer: Rethinking Hyperspectral Image Classification with Transformers. IEEE Transactions on Geoscience and Remote Sensing 60, 1–15. URL: http://arxiv.org/abs/2107.02988, doi:10.1109/TGRS.2021.3130716. arXiv:2107.02988 [cs.CV].

Hu, J., Shen, L., Albanie, S., Sun, G., Wu, E., 2019. Squeeze-and-Excitation Networks. URL: http://arxiv.org/abs/1709.01507, doi:10.48550/arXiv.1709.01507. arXiv:1709.01507 [cs.CV].

Huang, B., Lu, K., Audeberr, N., Khalel, A., Tarabalka, Y., Malof, J., Boulch, A., Le Saux, B., Collins, L., Bradbury, K., Lefèvre, S., El-Saban, M., 2018. Large-Scale Semantic Classification: Outcome of the First Year of Inria Aerial Image Labeling Benchmark, in: IGARSS 2018 - 2018 IEEE International Geoscience and Remote Sensing Symposium, pp. 6947–6950. URL: https://ieeexplore.ieee.org/document/8518525, doi:10.1109/IGARSS.2018.8518525.

Hurtado, J.V., Mohan, R., Valada, A., 2025. Hyperspectral Adapter for Semantic Segmentation with Vision Foundation Models. URL: http://arxiv.org/abs/2509.20107, doi:10.48550/arXiv.2509.20107. arXiv:2509.20107 [cs.CV].

Jiang, X., Wu, Z., Han, S., Yan, H., Zhou, B., Li, J., 2023. A multi-scale approach to detecting standing dead trees in UAV RGB images based on improved faster R-CNN. PLOS ONE 18,

e0281084. URL: https://journals.plos.org/plosone/article?id=10.1371/journal.pone.0281084, doi:10.1371/journal.pone.0281084.

Joshi, D., Witharana, C., 2025. Vision Transformer-Based Unhealthy Tree Crown Detection in Mixed Northeastern US Forests and Evaluation of Annotation Uncertainty. Remote Sensing 17, 1066. URL: https://www.mdpi.com/2072-4292/17/6/1066, doi:10.3390/rs17061066.

Jutras-Perreault, M.C., Næsset, E., Gobakken, T., Ørka, H.O., 2023. Detecting the presence of standing dead trees using airborne laser scanning and optical data. Scandinavian Journal of Forest Research 38, 208–220. URL: https://doi.org/10.1080/02827581.2023.2211807, doi:10.1080/02827581.2023.2211807. _eprint: https://doi.org/10.1080/02827581.2023.2211807.

Kattenborn, T., Eichel, J., Fassnacht, F.E., 2019a. Convolutional Neural Networks enable efficient, accurate and fine-grained segmentation of plant species and communities from high-resolution UAV imagery. Scientific Reports 9, 17656. doi:10.1038/s41598-019-53797-9.

Kattenborn, T., Eichel, J., Wiser, S., Burrows, L., Fassnacht, F.E., Schmidtlein, S., 2020. Convolutional Neural Networks accurately predict cover fractions of plant species and communities in Unmanned Aerial Vehicle imagery. Remote Sensing in Ecology and Conservation 6, 472–486. URL: https://onlinelibrary.wiley.com/doi/10.1002/rse2.146, doi:10.1002/rse2.146.

Kattenborn, T., Fassnacht, F.E., Schmidtlein, S., 2019b. Differentiating plant functional types using reflectance: which traits make the difference? Remote Sensing in Ecology and Conservation 5, 5–19. URL: https://zslpublications.onlinelibrary.wiley.com/doi/10.1002/rse2.86, doi:10.1002/rse2.86.

Kattenborn, T., Leitloff, J., Schiefer, F., Hinz, S., 2021. Review on Convolutional Neural Networks (CNN) in vegetation remote sensing. ISPRS Journal of Photogrammetry and Remote Sensing 173, 24–49. URL: https://www.sciencedirect.com/science/article/pii/S0924271620303488, doi:10.1016/j.isprsjprs.2020.12.010.

Kattenborn, T., Schiefer, F., Frey, J., Feilhauer, H., Mahecha, M.D., Dormann, C.F., 2022. Spatially autocorrelated training and validation samples inflate performance assessment of convolutional neural networks. ISPRS Open Journal of Photogrammetry and Remote Sensing 5, 100018. URL: https://www.sciencedirect.com/science/article/pii/S2667393222000072, doi:10.1016/j.ophoto.2022.100018.

Kattenborn, T., Schiefer, F., Zarco-Tejada, P., Schmidtlein, S., 2019c. Advantages of retrieving pigment content [g/cm2] versus concentration [%] from canopy reflectance. Remote Sensing of Environment 230, 111195. URL: https://www.sciencedirect.com/science/article/pii/S003442571930207X, doi:10.1016/j.rse.2019.05.014.

Kattenborn, T., Wieneke, S., Montero, D., Mahecha, M.D., Richter, R., Guimarães-Steinicke, C., Wirth, C., Ferlian, O., Feilhauer, H., Sachsenmaier, L., Eisenhauer, N., Dechant, B., 2024. Temporal dynamics in vertical leaf angles can confound vegetation indices widely used in Earth observations. Communications Earth & Environment 5, 550. URL: https://www.nature.com/articles/s43247-024-01712-0, doi:10.1038/s43247-024-01712-0. tex.copyright: 2024 The Author(s).

Koubaa, A., Ammar, A., Abdelkader, M., Alhabashi, Y., Ghouti, L., 2023. AERO: AI-Enabled Remote Sensing Observation with Onboard Edge Computing in UAVs. Remote Sensing 15, 1873. URL: https://www.mdpi.com/2072-4292/15/7/1873, doi:10.3390/rs15071873.

Lewis, M., Jooste, V., de Gasparis, A., 2001. Discrimination of arid vegetation with airborne multispectral scanner hyperspectral imagery. IEEE Transactions on Geoscience and Remote Sensing 39, 1471–1479. URL: https://ieeexplore.ieee.org/abstract/document/934078, doi:10.1109/36.934078.

Li, L., Mu, X., Jiang, H., Chianucci, F., Hu, R., Song, W., Qi, J., Liu, S., Zhou, J., Chen, L., Huang, H., Yan, G., 2023. Review of ground and aerial methods for vegetation cover fraction (fCover) and related quantities estimation: definitions, advances, challenges, and future perspectives. ISPRS Journal of Photogrammetry and Remote Sensing 199, 133–156. URL: https://www.sciencedirect.com/science/article/pii/S0924271623000801, doi:10.1016/j.isprsjprs.2023.03.020.

Li, Y., Luo, Y., Zhang, L., Wang, Z., Du, B., 2024. MambaHSI: Spatial–Spectral Mamba for Hyperspectral Image Classification. IEEE Transactions on Geoscience and Remote Sensing 62, 1–16. URL: https://ieeexplore.ieee.org/abstract/document/10604894, doi:10.1109/TGRS.2024.3430985.

Lin, M., Chen, Q., Yan, S., 2014. Network In Network. URL: http://arxiv.org/abs/1312.4400, doi:10.48550/arXiv.1312.4400. arXiv:1312.4400 [cs.NE].

Lin, T.Y., Goyal, P., Girshick, R., He, K., Dollár, P., 2017. Focal Loss for Dense Object Detection. URL: https://ui.adsabs.harvard.edu/abs/2017arXiv170802002L, doi:10.48550/arXiv.1708.02002.

Lucieer, A., Turner, D., King, D.H., Robinson, S.A., 2014. Using an Unmanned Aerial Vehicle (UAV) to capture micro-topography of Antarctic moss beds. International Journal of Applied Earth Observation and Geoinformation 27, 53–62. doi:10.1016/j.jag.2013.05.011.

López-Fandiño, J., B. Heras, D., Argüello, F., 2024. Using heterogeneous computing and edge computing to accelerate anomaly detection in remotely sensed multispectral images. The Journal of Supercomputing 80, 12543–12563. URL: https://doi.org/10.1007/s11227-024-05918-z, doi:10.1007/s11227-024-05918-z.

Makarov, A., Mirpulatov, I., Firsov, N., Lobanov, V., Illarionova, S., Podlipnov, V., Vybornova, Y., Shadrin, D., Rastorguev, A., Skidanov, R., Burnaev, E., Nikonorov, A., 2025. Deep Spectral-Spatial Transformer for Robust Hyperspectral Image Segmentation in Varying Field Conditions. IEEE Access 13, 97454–97471. URL: https://ieeexplore.ieee.org/document/11021539, doi:10.1109/ACCESS.2025.3575699.

Malenovský, Z., Lucieer, A., King, D.H., Turnbull, J.D., Robinson, S.A., 2017. Unmanned aircraft system advances health mapping of fragile polar vegetation. Methods in Ecology and Evolution 8, 1842–1857. URL: https://onlinelibrary.wiley.com/doi/10.1111/2041-210X.12833, doi:10.1111/2041-210X.12833.

Malenovský, Z., Turnbull, J.D., Lucieer, A., Robinson, S.A., 2015. Antarctic moss stress assessment based on chlorophyll content and leaf density

retrieved from imaging spectroscopy data. New Phytologist 208, 608–624. URL: https://onlinelibrary.wiley.com/doi/abs/10.1111/nph.13524, doi:10.1111/nph.13524. tex.copyright: © 2015 The Authors New Phytologist © 2015 New Phytologist Trust.

Melville, B., Fisher, A., Lucieer, A., 2019a. Ultra-high spatial resolution fractional vegetation cover from unmanned aerial multispectral imagery. International Journal of Applied Earth Observation and Geoinformation 78, 14–24. URL: https://www.sciencedirect.com/science/article/pii/S0303243418311693, doi:10.1016/j.jag.2019.01.013.

Melville, B., Fisher, A., Lucieer, A., 2019b. Ultra-high spatial resolution fractional vegetation cover from unmanned aerial multispectral imagery. International Journal of Applied Earth Observation and Geoinformation 78, 14–24. doi:10.1016/j.jag.2019.01.013.

Merton, R., 1998. Monitoring community hysteresis using spectral shift analysis and the red-edge vegetation stress index, in: Proceedings of the Seventh Annual JPL Airborne Earth Science Workshop, JPL Pasadena, CA, USA. pp. 12–16. URL: https://aviris.jpl.nasa.gov/proceedings/workshops/98_docs/37.pdf.

Mishra, N.B., Crews, K.A., 2014. Estimating fractional land cover in semi-arid central Kalahari: the impact of mapping method (spectral unmixing vs. object-based image analysis) and vegetation morphology. Geocarto International 29, 860–877. URL: https://doi.org/10.1080/10106049.2013.868041, doi:10.1080/10106049.2013.868041. _eprint: https://doi.org/10.1080/10106049.2013.868041.

Mittal, S., 2019. A Survey on optimized implementation of deep learning models on the NVIDIA Jetson platform. Journal of Systems Architecture 97, 428–442. URL: https://www.sciencedirect.com/science/article/pii/S1383762118306404, doi:10.1016/j.sysarc.2019.01.011.

Montero, D., Aybar, C., Mahecha, M.D., Martinuzzi, F., Söchting, M., Wieneke, S., 2023. A standardized catalogue of spectral indices to advance the use of remote sensing in Earth system research. Scientific Data 10, 197. URL: https://www.nature.com/articles/s41597-023-02096-0, doi:10.1038/s41597-023-02096-0. tex.copyright: 2023 The Author(s).

Montes-Herrera, J.C., Cimoli, E., Cummings, V.J., D'Archino, R., Nelson, W.A., Lucieer, A., Lucieer, V., 2024. Quantifying pigment content in crustose coralline algae using hyperspectral imaging: A case study with Tethysphytum antarcticum (Ross Sea, Antarctica). Journal of Phycology 60, 695–709. URL: https://onlinelibrary.wiley.com/doi/abs/10.1111/jpy.13449, doi:10.1111/jpy.13449. _eprint: https://onlinelibrary.wiley.com/doi/pdf/10.1111/jpy.13449.

Montes-Herrera, J.C., Robbins, A., Franson, C., Bektas, T., Sparrow, B., Lucieer, A., 2025. DroneScape: Collection of Penta-Return LiDAR for Ecosystem Plot Monitoring URL: https://www.protocols.io/print/dronescape-collection-of-penta-return-lidar-for-ec-g3c3byiyp.

Morgan, B.E., Chipman, J.W., Bolger, D.T., Dietrich, J.T., 2020. Spatiotemporal Analysis of Vegetation Cover Change in a Large Ephemeral River: Multi-Sensor Fusion of Unmanned Aerial Vehicle (UAV) and Landsat Imagery. Remote Sensing 13, 51. URL: https://www.mdpi.com/2072-4292/13/1/51, doi:10.3390/rs13010051.

Mosig, C., Vajna-Jehle, J., Mahecha, M.D., Cheng, Y., Hartmann, H., Montero, D., Junttila, S., Horion, S., Schwenke, M.B., Koontz, M.J., Maulud, K.N.A., Adu-Bredu, S., Al-Halbouni, D., Ali, M., Allen, M., Altman, J., Amorós, L., Angiolini, C., Astrup, R., Awada, H., Barrasso, C., Bartholomeus, H., Beck, P.S.A., Bozzini, A., Braun-Wimmer, J., Brede, B., Breunig, F.M., Brugnaro, S., Buras, A., Burchard-Levine, V., Camarero, J.J., Candotti, A., Capuder, L., Carrieri, E., Centritto, M., Chirici, G., Cloutier, M., Conciani, D., Cushman, K., Dalling, J.W., Dao, P.D., Dempewolf, J., Denter, M., Dogotari, M., Díaz-Delgado, R., Ecke, S., Eichel, J., Eltner, A., Fabbri, A., Fabi, M., Fassnacht, F., Ferreira, M.P., Fischer, F.J., Frey, J., Frick, A., Fuentes, J., Ganz, S., Garbarino, M., García, M., Gassilloud, M., Gazol, A., Gea-Izquierdo, G., Gerberding, K., Ghasemi, M., Giannetti, F., Gillan, J., Gonzalez, R., Gosper, C., Greene, T., Greinwald, K., Grieve, S., Große-Stoltenberg, A., Gutierrez, J.A., Göritz, A., Hajek, P., Hedding, D., Hempel, J., Heremans, S., Hernández, M., Heurich, M., Honkavaara, E., Höfle, B., Jackisch, R., Jucker, T., Kalwij, J.M., Kepfer-Rojas, S., Khatri-Chhetri, P., Kleinebecker, T., Klemmt, H.J., Klouček, T., Koivumäki, N., Kolagani, N., Komárek, J., Korznikov, K., Kraszewski, B., Kruse, S., Krüger, R.,

Kuechly, H., Kwong, I.H.Y., Laliberté, E., Langan, L., Latifi, H., Leal-Medina, C., Lehmann, J.R.K., Li, L., Lines, E., Lisiewicz, M., Lopatin, J., Lucieer, A., Ludwig, A., Ludwig, M., Lyytikäinen-Saarenmaa, P., Ma, Q., Mansuy, N., Peña, J.M., Marino, G., Maroschek, M., Martín, M.P., Martín-Benito, D., Matham, P., Mazzoni, S., Meloni, F., Menzel, A., Meyer, H., Miraki, M., Moreno, G., Moreno-Fernández, D., Muller-Landau, H.C., Mälicke, M., Möhring, J., Müllerova, J., Naidu, S.S., Nardi, D., Neumeier, P., Nita, M.D., Näsi, R., Oppgenoorth, L., Orunbaev, S., Palmer, M., Paul, T., Pfenning, M., Potts, A., Prasanna, G.L., Prober, S., Puliti, S., Pérez-Luque, A.J., Pérez-Priego, O., Reudenbach, C., Revuelto, J., Rivas-Torres, G., Roberge, P., Roggero, P.P., Rossi, C., Ruehr, N.K., Ruiz-Benito, P., Runge, C.M., Satta, G.G.A., Scanu, B., Scherer-Lorenzen, M., Schiefer, F., Schiller, C., Schladebach, J., Schmehl, M.T., Schmid, J., Schmidt, T.A., Schwarz, S., Seidl, R., Seifert, T., Barba, A.S., Shafeian, E., Shapiro, A., de Simone, L., Sohrabi, H., Soltani, S., Sotomayor, L., Sparrow, B., Steer, B.S.C., Stenson, M., Stöckigt, B., Su, Y., Suomalainen, J., Tamudo, E., Barbieri, M.J.T., Tomelleri, E., Torresani, M., Trepekli, K., Ullah, S., Ullah, S., Umlauft, J., Vargas-Ramírez, N., Vatandaslar, C., Visacki, V., Volpi, M., Vásquez, V., Wallis, C., Weinstein, B., Weiser, H., Wich, S., Ximena, T.C., Zarco-Tejada, P.J., Zdunic, K., Zielewska-Büttner, K., de Oliveira, R.A., van Wagtendonk, L., von Dosky, V., Kattenborn, T., 2026. deadtrees.earth — An open-access and interactive database for centimeter-scale aerial imagery to uncover global tree mortality dynamics. Remote Sensing of Environment 332, 115027. URL: https://www.sciencedirect.com/science/article/pii/S0034425725004316, doi:10.1016/j.rse.2025.115027.

Möhring, J., Kattenborn, T., Mahecha, M.D., Cheng, Y., Beloiu Schwenke, M., Cloutier, M., Denter, M., Frey, J., Gassilloud, M., Göritz, A., Hempel, J., Horion, S., Jucker, T., Junttila, S., Khatri-Chhetri, P., Korznikov, K., Kruse, S., Laliberté, E., Maroschek, M., Neumeier, P., Pérez-Priego, O., Potts, A., Schiefer, F., Seidl, R., Vajna-Jehle, J., Zielewska-Büttner, K., Mosig, C., 2025. Global, multi-scale standing deadwood segmentation in centimeter-scale aerial images. ISPRS Open Journal of Photogrammetry and Remote Sensing 18, 100104. URL: https://www.sciencedirect.com/science/article/pii/S2667393225000237, doi:10.1016/j.ophoto.2025.100104.

Nagler, P.L., Daughtry, C.S.T., Goward, S.N., 2000. Plant Litter and Soil Reflectance. Remote Sensing of Environment 71, 207–215. URL: https://www.sciencedirect.com/science/article/pii/S0034425799000826, doi:10.1016/S0034-4257(99)00082-6.

Reddig, F., Hütt, C., Jenal, A., Wolf, J., Bareth, G., 2025. The Invisible Plant: Estimating Fractional Vegetation Cover of Tillandsia landbeckii in the Atacama Desert using Hyperspectral EnMAP and High-Resolution Validation Data. PFG – Journal of Photogrammetry, Remote Sensing and Geoinformation Science 93, 583–609. URL: https://doi.org/10.1007/s41064-025-00358-7, doi:10.1007/s41064-025-00358-7.

RESE, 2025. Droacor - Rese Remote Sensing Software. URL: https://www.rese-apps.com/droacor/.

Ronneberger, O., Fischer, P., Brox, T., 2015. U-Net: Convolutional Networks for Biomedical Image Segmentation, in: Navab, N., Hornegger, J., Wells, W.M., Frangi, A.F. (Eds.), Medical Image Computing and Computer-Assisted Intervention – MICCAI 2015, Springer International Publishing, Cham. pp. 234–241. doi:10.1007/978-3-319-24574-4_28.

Růžička, V., Markham, A., 2024. HyperspectralViTs: General Hyperspectral Models for On-board Remote Sensing. URL: https://arxiv.org/abs/2410.17248v3, doi:10.1109/JSTARS.2025.3557527.

Sandino, J., Barthelemy, J., Doshi, A., Randall, K., Robinson, S.A., Bollard, B., Gonzalez, F., 2025. Drone hyperspectral imaging and artificial intelligence for monitoring moss and lichen in Antarctica. Scientific Reports 15, 27244. URL: https://www.nature.com/articles/s41598-025-11535-4, doi:10.1038/s41598-025-11535-4. tex.copyright: 2025 The Author(s).

Scarth, P., 2012. Tracking Grazing Pressure and Climate Interaction - The Role of Landsat Fractional Cover in Time Series Analysis URL: https://figshare.com/articles/journal_contribution/Tracking_Grazing_Pressure_and_Climate_Interaction_-_The_Role_of_Landsat_Fractional_Cover_in_Time_Series_Analysis/94250/1, doi:10.6084/m9.figshare.94250.v1.

Scheiter, M., Valentine, A., Sambridge, M., 2022. Upscaling and downscaling Monte Carlo ensembles with generative models. Geophysical Journal International 230, 916–931. URL: https://doi.org/10.1093/gji/ggac100, doi:10.1093/gji/ggac100.

Schiefer, F., Kattenborn, T., Frick, A., Frey, J., Schall, P., Koch, B., Schmidtlein, S., 2020. Mapping forest tree species in high resolution UAV-based RGB-imagery by means of convolutional neural networks. ISPRS Journal of Photogrammetry and Remote Sensing 170, 205–215. URL: https://www.sciencedirect.com/science/article/pii/S0924271620302938, doi:10.1016/j.isprsjprs.2020.10.015.

Schiefer, F., Schmidtlein, S., Frick, A., Frey, J., Klinke, R., Zielewska-Büttner, K., Junttila, S., Uhl, A., Kattenborn, T., 2023. UAV-based reference data for the prediction of fractional cover of standing deadwood from Sentinel time series. ISPRS Open Journal of Photogrammetry and Remote Sensing 8, 100034. URL: https://www.sciencedirect.com/science/article/pii/S2667393223000054, doi:10.1016/j.ophoto.2023.100034.

Sothe, C., , C. M., D.A., , M. B., S., , L. E. C., L.R., , J. D. B., C., , R. Q., F., , M., D., , C. L., L., , V., L., , G. T., M., , Tommaselli, A.M.G., 2020. Comparative performance of convolutional neural network, weighted and conventional support vector machine and random forest for classifying tree species using hyperspectral and photogrammetric data. GIScience & Remote Sensing 57, 369–394. URL: https://doi.org/10.1080/15481603.2020.1712102, doi:10.1080/15481603.2020.1712102.

Sotomayor, L.N., Lucieer, A., Turner, D., Barthelemy, J., Kattenborn, T., 2026. From 2D labels to 3D structure: Scalable label transfer and benchmarking of 3D vegetation models in rangeland ecosystems URL: https://eartharxiv.org/repository/view/12889/. tex.copyright: CC BY Attribution 4.0 International.

Sotomayor, L.N., Lucieer, A., Turner, D., Lewis, M., Kattenborn, T., 2025a. Mapping fractional vegetation cover in UAS RGB and multispectral imagery in semi-arid Australian ecosystems using CNN-based semantic segmentation. Landscape Ecology 40, 169. URL: https://doi.org/10.1007/s10980-025-02193-y, doi:10.1007/s10980-025-02193-y.

Sotomayor, L.N., Megan, L., Krishna, L., Hoyer, S., Molly, M., Arko, L., 2025b. Fractional Vegetation Cover Mapping - UAS RGB and Multispectral Imagery, CNN algorithms, Semi-Arid Australian Ecosystems Coverage URL: https://zenodo.org/records/15036860.

Sotomayor, L.N., Megan, L., Krishna, L., Sophia, H., Molly, M., Arko, L., 2025c. Fractional vegetation cover mapping - UAS RGB and multispectral imagery, CNN algorithms, semi-arid australian ecosystems coverage. URL: https://doi.org/10.5281/zenodo.15036860, doi:10.5281/zenodo.15036860.

Storch, T., Honold, H.P., Chabrillat, S., Habermeyer, M., Tucker, P., Brell, M., Ohndorf, A., Wirth, K., Betz, M., Kuchler, M., Mühle, H., Carmona, E., Baur, S., Mücke, M., Löw, S., Schulze, D., Zimmermann, S., Lenzen, C., Wiesner, S., Aida, S., Kahle, R., Willburger, P., Hartung, S., Dietrich, D., Plesia, N., Tegler, M., Schork, K., Alonso, K., Marshall, D., Gerasch, B., Schwind, P., Pato, M., Schneider, M., de los Reyes, R., Langheinrich, M., Wenzel, J., Bachmann, M., Holzwarth, S., Pinnel, N., Guanter, L., Segl, K., Scheffler, D., Foerster, S., Bohn, N., Bracher, A., Soppa, M.A., Gascon, F., Green, R., Kokaly, R., Moreno, J., Ong, C., Sornig, M., Wernitz, R., Bagschik, K., Reintsema, D., La Porta, L., Schickling, A., Fischer, S., 2023. The EnMAP imaging spectroscopy mission towards operations. Remote Sensing of Environment 294, 113632. URL: https://www.sciencedirect.com/science/article/pii/S0034425723001839, doi:10.1016/j.rse.2023.113632.

TERN, 2021. Summary of TERN plots on Calperum, South Australia.

TERN, L., 2022. Field Survey Apps & Protocols | TERN Land Ecosystem Research Network. URL: https://www.tern.org.au/field-survey-protocols/.

TERN, L., Monitoring, T.S., Stenson, M., Sparrow, B., Lucieer, A., 2022. Drone RGB and Multispectral Imagery from TERN plots across Australia. URL: https://portal.tern.org.au/metadata/TERN/39de90f5-49e3-4567-917c-cf3e3bc93086.

TERN, T.E.R.N., 2026. terndata.ecoplots 1.0.0 documentation. URL: https://terndata-ecoplots.readthedocs.io/en/latest/.

Tucker, C.J., 1979. Red and photographic infrared linear combinations for monitoring vegetation. Remote Sensing of Environment 8, 127–150. URL: https://www.sciencedirect.com/science/article/pii/0034425779900130, doi:10.1016/0034-4257(79)90013-0.

Turner, D., Cimoli, E., Lucieer, A., Haynes, R.S., Randall, K., Waterman, M.J., Lucieer, V., Robinson, S.A., 2023. Mapping water content in drying Antarctic moss communities using UAS-borne SWIR imaging spectroscopy. Remote Sensing in Ecology and Conservation n/a. URL: https://onlinelibrary.wiley.com/doi/abs/10.1002/rse2.371, doi:10.1002/rse2.371. tex.copyright: © 2023 The Authors. Remote Sensing in Ecology and Conservation published by John Wiley & Sons Ltd on behalf of Zoological Society of London.

Turner, D., Cimoli, E., Lucieer, A., Haynes, R.S., Randall, K., Waterman, M.J., Lucieer, V., Robinson, S.A., 2024. Mapping water content in drying Antarctic moss communities using UAS-borne SWIR imaging spectroscopy. Remote Sensing in Ecology and Conservation 10, 296–311. URL: https://onlinelibrary.wiley.com/doi/abs/10.1002/rse2.371, doi:10.1002/rse2.371. tex.copyright: © 2023 The Authors. Remote Sensing in Ecology and Conservation published by John Wiley & Sons Ltd on behalf of Zoological Society of London.

Uddin, M.P., Mamun, M.A., Hossain, M.A., 2021. PCA-based Feature Reduction for Hyperspectral Remote Sensing Image Classification. IETE Technical Review 38, 377–396. URL: https://doi.org/10.1080/02564602.2020.1740615, doi:10.1080/02564602.2020.1740615.

Ustin, S.L., Gamon, J.A., 2010. Remote sensing of plant functional types. New Phytologist 186, 795–816. URL: https://onlinelibrary.wiley.com/doi/abs/10.1111/j.1469-8137.2010.03284.x, doi:10.1111/j.1469-8137.2010.03284.x. _eprint: https://nph.onlinelibrary.wiley.com/doi/pdf/10.1111/j.1469-8137.2010.03284.x.

Vaswani, A., Shazeer, N., Parmar, N., Uszkoreit, J., Jones, L., Gomez, A.N., Kaiser, L., Polosukhin, I., 2023. Attention Is All You Need. URL: http://arxiv.org/abs/1706.03762, doi:10.48550/arXiv.1706.03762. arXiv:1706.03762 [cs.CL].

Veitch-Michaelis, J., Cottam, A., Schweizer, D., Broadbent, E.N., Dao, D., Zhang, C., Zambrano, A.A., Max, S., 2024. OAM-TCD: A globally diverse dataset of high-resolution tree cover maps. URL: http://arxiv.org/abs/2407.11743, doi:10.48550/arXiv.2407.11743. arXiv:2407.11743 [cs.CV].

Verrelst, J., Halabuk, A., Atzberger, C., Hank, T., Steinhauser, S., Berger, K., 2023. A comprehensive survey on quantifying non-photosynthetic vegetation cover and biomass from imaging spectroscopy. Ecological Indicators 155, 110911. URL: https://www.sciencedirect.com/science/article/pii/S1470160X23010531, doi:10.1016/j.ecolind.2023.110911.

Wada, K., others, 2021. wkentaro/labelme: v4.6.0. URL: https://zenodo.org/records/5711226, doi:10.5281/zenodo.5711226.

Wang, X., Liu, S., Shen, X., Shen, C., Jia, J., 2019a. Associatively Segmenting Instances and Semantics in Point Clouds. URL: http://arxiv.org/abs/1902.09852, doi:10.48550/arXiv.1902.09852.

Wang, Z., Townsend, P.A., Schweiger, A.K., Couture, J.J., Singh, A., Hobbie, S.E., Cavender-Bares, J., 2019b. Mapping foliar functional traits and their uncertainties across three years in a grassland experiment. Remote Sensing of Environment 221, 405–416. URL: https://www.sciencedirect.com/science/article/pii/S003442571830525X, doi:10.1016/j.rse.2018.11.016.

White, A., Sparrow, B., Leitch, E., Foulkes, J., Flitton, R., Lowe, A.J., Caddy-Retalic, S., 2012. AusPlots Rangelands Survey Protocols Manual. University of Adelaide Press. URL: https://digital.library.adelaide.edu.au/dspace/handle/2440/101955. tex.copyright: © The Authors 2012 This book is copyright. Apart from any fair dealing for the purposes of private study, research, criticism or review as permitted under the Copyright Act, no part may be reproduced, stored in a retrieval system, or transmitted, in any form or by any means, electronic, mechanical, photocopying, recording or otherwise without the prior written permission.

Xie, E., Wang, W., Yu, Z., Anandkumar, A., Alvarez, J.M., Luo, P., 2021. SegFormer: Simple and Efficient Design for Semantic Segmentation with Transformers. URL: http://arxiv.org/abs/2105.15203, doi:10.48550/arXiv.2105.15203. arXiv:2105.15203 [cs.CV].

Xiong, Y., Varadarajan, B., Wu, L., Xiang, X., Xiao, F., Zhu, C., Dai, X., Wang, D., Sun, F., Iandola, F., Krishnamoorthi, R., Chandra, V., 2023. EfficientSAM: Leveraged Masked Image Pretraining for Efficient Segment Anything. URL: http://arxiv.org/abs/2312.00863, doi:10.48550/arXiv.2312.00863.

Xiong, Y., Zhou, C., Xiang, X., Wu, L., Zhu, C., Liu, Z., Suri, S., Varadarajan, B., Akula, R., Iandola, F., Krishnamoorthi, R., Soran, B., Chandra, V., 2024. Efficient Track Anything. URL: http://arxiv.org/abs/2411.18933, doi:10.48550/arXiv.2411.18933.

Xue, J., Su, B., 2017. Significant Remote Sensing Vegetation Indices: A Review of Developments and Applications. Journal of Sensors 2017, 1353691. URL: https://onlinelibrary.wiley.com/doi/abs/10.1155/2017/1353691, doi:10.1155/2017/1353691. tex.copyright: Copyright © 2017 Jinru Xue and Baofeng Su.

Yang, D., Morrison, B.D., Hantson, W., Breen, A.L., McMahon, A., Li, Q., Salmon, V.G., Hayes, D.J., Serbin, S.P., 2021. Landscape-scale characterization of Arctic tundra vegetation composition, structure, and function with a multi-sensor unoccupied aerial system. Environmental Research Letters 16, 085005. URL: https://doi.org/10.1088/1748-9326/ac1291, doi:10.1088/1748-9326/ac1291.

Zhao, Y., Sun, Y., Lu, X., Zhao, X., Yang, L., Sun, Z., Bai, Y., 2021. Hyperspectral retrieval of leaf physiological traits and their links to ecosystem productivity in grassland monocultures. Ecological Indicators 122, 107267. URL: https://www.sciencedirect.com/science/article/pii/S1470160X20312073, doi:10.1016/j.ecolind.2020.107267.

Zou, L., Zhu, X., Wu, C., Liu, Y., Qu, L., 2020. Spectral–Spatial Exploration for Hyperspectral Image Classification via the Fusion of Fully Convolutional Networks. IEEE Journal of Selected Topics in Applied Earth Observations and Remote Sensing 13, 659–674. URL: https://ieeexplore.ieee.org/document/8984214, doi:10.1109/JSTARS.2020.2968179.

References

Leslie Lamport, *LaTeX: a document preparation system*, Addison Wesley, Massachusetts, 2nd edition, 1994.